UNIVERSITY OF CALIFORNIA SAN DIEGO

Coastal Hazards: Predicting wave runup through storms and assessing saltwater intrusion in coastal freshwaters

A dissertation submitted in partial satisfaction of the
requirements for the degree Doctor of Philosophy

in

Oceanography

by

Lauren Nicole Kim

Committee in charge:

Morgan C. Levy, Chair
Sarah N. Giddings, Co-Chair
Mark A. Merrifield, Co-Chair
Adrian Borsa
Jennifer Burney
Mara M. Orescanin

2024

The Dissertation of Lauren Nicole Kim is approved, and it is acceptable in quality and form for publication on microfilm and electronically.

University of California San Diego

2024

DEDICATION

To Nana and Poppo.

TABLE OF CONTENTS

LIST OF FIGURES

LIST OF TABLES

ACKNOWLEDGEMENTS

Back in 2013, my grandparents took me to La Jolla Shores to see the leopard sharks in the summer before I started college. At the time, I had no idea that I was in the place that I would call home for all of grad school and that I hope to call home for the rest of my life. This work is dedicated to my grandparents for their unending support in all my endeavors: from school, to dance, to sewing, to baking. Some of my fondest memories include them and the time they spent taking my brother and I on all sorts of adventures. I can't thank them enough for all that they've done for me.

I always joked with my grandpa that I would eventually get more degrees than he had, and although he's no longer with us, I know he would be endlessly proud of me for achieving this.

Thank you to my advisors, Morgan, Sarah, and Mark. I appreciate you letting me try something different for my thesis and being kind and supportive throughout the whole process. I really enjoyed having a whole advising team and integrating all your perspectives into my work.

Thank you also to my family and friends for being there for me throughout this entire process. This has been quite the journey and I couldn't have done it without all your love and support.

Chapter 2, in full, is a reprint of the paper "Observations of beach change and runup, and the performance of empirical runup parameterizations during large storm events" published in Coastal Engineering by L.N. Kim, K.L. Brodie, N.T. Cohn, S.N. Giddings, and M.A. Merrifield in 2023. The dissertation author was the primary investigator and author of this paper.

Chapter 3, in full, has been submitted for publication as it may appear in Water Resources Research 2024. L.N. Kim, C. Meusel, R. Barker, B. Lockwood, M. Strudley, D. Behrens, M.M. Orescanin, M.A. Merrifield, S.N. Giddings, M.C. Levy. The dissertation author was the primary investigator and author of this paper.

Chapter 4, in part, is currently being prepared for submission for publication of the material. L.N. Kim, S.N. Giddings, M.A. Merrifield, L. Cagigal, M.C. Levy. The dissertation author was the primary investigator and author of this material.

VITA

2017	Bachelor of Science, Physics - California State Polytechnic University, Pomona, USA
2019	Master of Science, Oceanography - University of California San Diego, USA
2024	Doctor of Philosophy, Oceanography - University of California San Diego, USA

PUBLICATIONS

Enhanced Surf Zone and Wave Runup Observations with Hovering Drone-Mounted Lidar Fiedler, J.W., Kim, L.N., Grenzeback, R.L., Young, A.P. and Merrifield, M.A. *Journal of Atmospheric and Oceanic Technology* (2021)

Observations of beach change and runup, and the performance of empirical runup parameterizations during large storm events Kim, L.N., Brodie, K.L., Cohn, N.T., Giddings, S.N., Merrifield, M. *Coastal Engineering* (2023)

ABSTRACT OF THE DISSERTATION

Coastal Hazards: Predicting wave runup through storms and assessing saltwater intrusion in coastal freshwaters

by

Lauren Nicole Kim

Doctor of Philosophy in Oceanography

University of California San Diego, 2024

Morgan C. Levy, Chair
Sarah N. Giddings, Co-Chair
Mark A. Merrifield, Co-Chair

Extreme events, like drought, large storms, and coastal floods are expected to increase under climate change. Along the coast, where an estimated 1 billion people are expected to reside by the end of the century, these hazards threaten infrastructure and livelihoods. Here, we investigate two coastal hazards that are expected to worsen under climate change: coastal storms and their impacts on beaches, and saltwater intrusion (SWI) impacts on coastal freshwater use, which are linked through total water level at the shoreline. To investigate the first coastal hazard, we use stationary lidar data with high

spatial and temporal resolution to compare observations of runup with predicted runup using various runup parameterizations in the Outer Banks, NC, USA. We also investigate the performance of the parameterizations using a pre-storm versus a time varying beach slope. The results suggest that a pre-storm beach slope may be sufficient in predicting runup throughout a storm for a number of parameterizations, but that the presence of two-dimensional morphologic features (beach cusps) greatly degrade the performance of the parameterizations. To address the second coastal hazard, we use inland hydrologic and oceanographic datasets to investigate the drivers of SWI in the surface freshwater sloughs of the Pajaro Valley, CA, USA. The results of this study suggest that the co-occurrence of high total water levels (oceanic water level plus wave runup) and low inland flow conditions create the conditions necessary for SWI. Additionally, the closure of the lagoon mouth, which is driven by identical processes, is likely a key component in SWI occurrence. Finally, we expand the SWI study to incorporate future climate scenarios using modelled sea level and precipitation and simulations of wave time series. Under the CMIP5 RCP 8.5, 99th percentile, SWI risk frequency is expected to increase by nearly 20% by the end of the century. This increase is dominated by sea level rise, with some variability contributed by the timing of large wave and low precipitation events. The investigation of these hazards advances the science-informed development of coastal and freshwater mitigation strategies under a changing climate.

Chapter 1

Introduction

Under climate change projections, extreme events, like drought, large storms, and coastal floods, are expected to increase in both frequency and intensity (Elko et al., 2014, 2019; Langridge, 2018). These events threaten infrastructure and livelihoods along coasts around the world where an estimated 800 million people are living within 10 m of sea level (Elko et al., 2014). Nearly 40% of the U.S. population resides along the U.S. east and west coasts (NOAA, 2021). The IPCC 5th assessment reports that sea level rise is already impacting livelihoods, economic activities, and infrastructure, and that much of North American infrastructure is currently vulnerable to extreme weather events (IPCC, 2014). In this proposal, I observe two different processes affected by different aspects of climate change: storm-driven wave runup and beach impacts, and saltwater intrusion (SWI) impacts on coastal freshwater use. The purpose of the studies herein are to investigate coastal hazards that threaten infrastructure in the context of a changing climate.

Observations of coastal processes during high energy wind and wave events, like storms, are uncommon due to the difficulty of obtaining data in these harsh conditions. A lack of observations during these high impact events, in turn, makes their effect on surfzone bathymetry, beach morphology, and wave runup difficult to predict. As noted by Elko et al. (2019), novel observations of dune impacts and oceanographic forcings throughout storms are necessary to advance our understanding of storm impacts and recovery processes.

Currently wave runup forecasts to assess storm impacts rely on beach slope estimates that are collected some time prior to the storm of interest and are presumed constant throughout the event (Phillips et al., 2017; Harley et al., 2016, 2017; Beuzen et al., 2019; Burvingt et al., 2017; Pye, Blott, 2016). However, the transient nature of beaches and their morphologic features throughout high energy events necessitate further investigation into the validity of this assumption for predicting wave runup and storm impacts. Given that the coastal zone is a critical resource to many communities and that it is particularly vulnerable to increasing sea levels and storm intensity and frequency (Elko et al., 2014, 2019), it is imperative to improve observations in order to make strides in predicting storm and high energy wave impacts on beaches.

For coastal regions dependent on coastal freshwater, including coastal agricultural sectors, salinity intrusion in both surface waters and groundwater can greatly affect water availability. On a global scale, agriculture uses approximately 70% of available freshwater resources (Cosgrove, Loucks, 2015). Agricultural sectors that primarily use coastal freshwater are susceptible to over-drawing freshwater from both groundwater and surface water systems and thus inducing seawater intrusion (SWI). This, coupled with drought, sea level rise, and inundation from storms and tides, can severely limit the amount of usable freshwater (Tully et al., 2019). Currently, SWI is one of the leading causes of groundwater contamination (Michael et al., 2017). The impact of marine salt input to to groundwater, for example, is far reaching and can induce coastal forest loss, increase the presence of invasive species, and cause marsh migration, in addition to reducing agricultural productivity (Tully et al., 2019). Importantly, research focused on surface water SWI, in particular, is lacking. Thus, further research in the interest of preserving coastal freshwater resources is necessary to support climate change adaptation.

In this study, oceanic total water level (TWL) plays an important role in the investigation of these coastal hazards. TWL is comprised of a sea level component, which may be influenced by astronomical tides, regional dynamics, and sea level anomalies (Pugh,

1987), and a wave driven component, for which we use $R_{2\%}$, or the 2% exceedence level of the vertical uprush of waves (Stockdon et al., 2006). Although $R_{2\%}$ may be calculated directly from observations, parameterizations are often relied upon due to the difficulty of obtaining the necessary nearshore measurements, especially in high energy conditions. These parameterizations often utilize deep water or nearshore wave measurements, which can be obtained with wave buoys or pressure sensors, and estimates of beach slope, which can be obtained through beach surveys or satellite data.

1.1 Research Outline

The goal of this thesis is to investigate current coastal hazards, including large storm events and salinity intrusion events, that threaten infrastructure in the context of a changing climate. This is done in the following chapters.

In Chapter 2, *Estimating runup through storms and subsequent recovery periods*, we investigate the questions of how well do runup parameterizations predict runup during large storms events? And how well do they perform when beach cusps form during beach recovery periods post-storm? We utilize stationary lidar data of sea surface, wave runup, and beach morphology to assess several widely used runup parameterizations during and after storm periods in Duck, NC, USA.

In Chapter 3, *Drivers of saltwater intrusion in surface sloughs*, we address the questions of what are the oceanographic and hydrologic drivers of salinity intrusion in a human-altered freshwater slough system? And how are lagoon mouth closures linked to these intrusions? We use a wide range of data, including data from slough water monitoring stations, offshore buoys, tide gauges, rain gauges, river discharge gauges, and visual lagoon monitoring, to assess the drivers of salinity intrusions in the Pajaro Valley's Harkins-Watsonville slough and to establish thresholds of total water level and river discharge in which salinity intrusion may be expected.

And finally in Chapter 4, *Assessing future SWI risk using projections of TWL and precipitation*, we investigate the questions of how do the magnitude and frequency of drivers of salinity intrusion change under future climate projections? And what tools can be used by coastal managers to predict saltwater intrusion under different climate scenarios? We use CMIP5 modeled sea level and precipitation and simulated waves using TESLA, a wave emulator, to explore the changes in magnitude and frequency of salinity intrusions in the Pajaro Valley's Harkins-Watsonville slough under the RCP 8.5, 99th percentile scenario.

Chapter 2

Estimating runup through storms and subsequent recovery periods

2.1 Abstract

Timeseries observations of beach elevation change and wave runup from a tower-mounted stationary lidar are used to assess the skill ($skill = 1 - NMSE$, where NMSE is the normalized mean square error) of 2% runup exceedence ($R_{2\%}$) estimates (Stockdon et al., 2006) during four storm events at Duck, NC, USA. The runup parameterization requires specification of the foreshore beach slope, however beach slope is generally unknown during high energy events, and pre-storm estimates of beach slope are often used as a proxy. $R_{2\%}$ hindcasts are computed using the observed time-varying beach slope and a static pre-storm beach profile. The time-varying beach slope yields $R_{2\%}$ skill of 0.57 compared to the observed $R_{2\%}$. Similar skill scores are obtained using a tidally variable beach slope, derived from the static pre-storm beach profile, due in part to limited beach volume (-10.4 to 7.7 m^3/m) and foreshore slope (0.04 - 0.09 m/m) changes during the four events. The skill drops to -1.0 using seasonal mean beach slopes. Even using the observed beach profiles, the skill reduces (-0.86) just after the peak of two of the storms due to the appearance of beach cusps ($\sim$ 40 m wavelength) in the swash zone morphology. For one storm (a Nor'Easter), runup is underpredicted by up to 1.0 m at high tides following the storm peak when cusps are present, which coincides with high tides of near equal magnitude to those

near the storm peak. Additional pre- and post-storm mobile lidar surveys for one of the storms confirm ubiquitous small-scale beach cusps along 8 km of the local shoreline. The results suggest that skillful runup estimates during storms are often attainable given the availability of beach information just before a storm. The parameterization errors increase when beach cusps develop, highlighting the need to extend standard one-dimensional runup parameterizations to account for two-dimensional effects.

2.2 Introduction

Beaches and sand dunes provide critical protection to coastal infrastructure from the impacts of energetic storm events. Wave runup, which is the the time-varying vertical excursion of swash on a beach, is a particularly important quantity for assessing site-specific coastal hazards (e.g., Stockdon et al. (2007a)). Due to recognized topographic and bathymetric feedbacks on wave setup and swash, most empirical models of wave runup commonly used for these analyses utilize a foreshore slope definition to represent the shape of the coastal profile (Atkinson et al., 2017; Holman, 1986; Stockdon et al., 2006). Storm runup forecasts and storm impact studies generally rely on foreshore slope estimates from pre-storm or historical beach profiles; quantities that are typically assumed to remain constant throughout storm events for estimating wave runup (Phillips et al., 2017; Harley et al., 2016, 2017; Beuzen et al., 2019; Burvingt et al., 2017; Pye, Blott, 2016). Net beach changes, including volume losses to the beach and dune, are usually assessed from pre- and post-storm surveys. Given that there are often considerable beach volume changes and complex evolution of beach morphology (e.g., cusp generation) during storms (O'Dea et al., 2019), which influences the foreshore slope, then stationary beach properties (e.g., slope) may be a poor assumption at the intra-storm timescale. Due to the feedback effects on foreshore slope on extreme runup, this time-evolving morphology has direct implications on the prediction of wave runup and the corresponding hazard. Unfortunately data of beach

morphology change is rarely available at this intra-storm scale to improve over current approaches. This deficiency highlights questions such as (1) *what aspects of intra-storm variability need to be accounted for to obtain skillful runup estimates?* and (2) *to what extent does an evolving beach profile and the appearance of cusp formations diminish the skill of one-dimensional (single cross-shore transect) runup estimates?*

Contemporaneous observations of runup and beach change are needed throughout individual storm events to assess the specific timing of morphologic changes which subsequently affect wave runup. Swash zone field measurements generally have been lacking due to the challenges of collecting in-situ and remotely sensed data in the midst of storm wave conditions, which frequently are accompanied by extreme winds and rain. Global Navigation Satellite System (GNSS) surveys that rely on cart, jetski, all-terrain vehicles (ATVs), (Ludka et al., 2019; Turner et al., 2016), or amphibious vehicles (Smith et al., 2017) are labor intensive, difficult to stage during storm conditions, and limited in spatial and temporal resolution. Stationary cameras, such as Argus, have provided long-term observations of nearshore variability; however, accurate vertical measurements from these cameras require further assumptions or direct measurements of reference points. Additionally, quantitative estimates of beach change and runup may be compromised during high wind and heavy rain conditions (Holman, Haller, 2013). The advent of continuous lidar scanning (Spore et al., 2019; Phillips et al., 2019; Almeida et al., 2013; Brodie, 2010; Pye, Blott, 2016; O'Dea et al., 2019; Splinter et al., 2018; Matsumoto et al., 2020; Burvingt et al., 2017; Beuzen et al., 2019; Vousdoukas et al., 2014; Brodie et al., 2015; Blenkinsopp et al., 2010; Martins et al., 2017; Almar et al., 2017), has opened opportunities to measure wave runup on an evolving beach morphology during storms. Lidar systems can be configured to record the swash zone surface elevation, the beach face, and runup elevation simultaneously at sub-centimeter resolutions (Blenkinsopp et al., 2010). Henderson et al. (2022) used lidar to capture an energetic runup event at Imperial Beach, CA as the beach eroded by nearly 80-cm in elevation, with measurable impacts on runup estimates. However in a

previous study, a temporary tower-fixed lidar captured onshore net deposition on a gravel beach during a storm event in Loe Bar, SW England (Almeida et al., 2013).

Most operational runup models and lidar scanning systems are applied at cross-shore transects (i.e., one-dimensional), yet recent studies highlight that the response of nearshore-beach-dune systems to storm forcing is a complex, coupled morphological evolution at various temporal and spatial scales. Typically, beaches tend to erode at the storm timescale, with considerable alongshore variability in the response. For example, at Narrabeen-Collaroy Beach in Australia, an extratropical cyclone induced a reduction in beach volume that ranged from near zero to 124 m^3/m over a 2500 m alongshore extent of coastline (Harley et al., 2016). Beach recovery may happen quickly following a storm, even during moderate wave conditions ($\sim$ 2 m significant wave height), as observed in Faro Beach (Vousdoukas et al., 2012a). Recognized controls on alongshore variability in both beach erosion and responses to the beach-adjacent dune or bluff systems include the role of crescentic bars or bathymetric anomalies (Holman, Sallenger Asbury H., 1993; Senechal et al., 2018; Cohn et al., 2021), pre-storm beach slope or volume (Lee et al., 1998; Vousdoukas et al., 2012a; Dissanayake et al., 2015; Splinter et al., 2014), and local vegetation properties (Feagin et al., 2019; Charbonneau, Dohner, 2021).

Runup models, including non-hydrostatic models, like XBeach (Smit et al., 2010) and SWASH (Zijlema et al., 2011), and empirical parameterizations (Stockdon et al., 2006; Holman, 1986; Nielsen, 2009; Ruggiero et al., 2001; Vousdoukas et al., 2012b; Atkinson et al., 2017; Senechal et al., 2011) require measurements of beach morphology. In part due to fewer input data requirements and reduced computational needs related to wave-resolving numerical models, empirical equations are most commonly used for hazard assessments. For empirical parameterizations, such as the widely used Stockdon et al. (2006) equation, a single value representative of the foreshore beach slope β is often used. The parameterization requires measurements of deep water wave length (H_0) and period (T_0) in addition to β. Despite the widespread use of this equation, there are a range of

different approaches to defining the foreshore beach slope. Limited guidance currently exists for the optimum way to specify β during storm conditions to best predict wave runup.

As noted by Stockdon et al. (2006), the one-dimensional parameterization (i.e., β is specified across a single cross-shore transect) may be compromised by the presence of megacusps, which are $\sim$ 200 m rhythmic features in the alongshore (Thornton et al., 2007). Mega-cusps are common features that have been observed on sandy beaches throughout the world, including along the Outer Banks, NC (Stockdon et al., 2006). Moreover, smaller beach cusps with wavelengths reported between 12 and 40 m are commonly observed on the lower beach at sites around the world (Holland, Holman, 1996; Miller et al., 1989; Holland, 1998; Agredano et al., 2019; Matsumoto et al., 2020). These small-scale cusps are cited as both erosional and depositional features that are often destroyed by passing storms and reformed within days (Miller et al., 1989) or even at the sub-tidal timescale (O'Dea, Brodie, 2019). These morphologic processes may also couple with hydrologic processes, as Ciriano et al. (2005) indicate that low frequency swash oscillations are affected by the development of beach cusps, and vice versa.

Here, we examine stationary lidar observations of sub-aerial beach and swash zone surface elevations during 4 distinct storm periods and mobile lidar observations of beach/dune morphology from pre- and post-conditions during 2 storms collected at the US Army Engineer Research and Development Center's (ERDC) Field Research Facility (FRF) in Duck, NC, USA. The stationary lidar system conducts linescans along a $\sim$ 65 m cross-shore range and also completes 2D framescans that cover a $\sim$ 500 m alongshore stretch of beach every hour. 10 cm and 1 m horizontal resolutions are achieved with the linescanning and framescanning modes, respectively. The system has been sampling near-continuously since September 2015 at the FRF (O'Dea et al., 2019; Cohn et al., 2021) and was fully operational during the 4 storms considered here. The mobile lidar system, covering 8 km of the Outer Banks coast, provided detailed pre- and post- storm

beach/dune morphology (Spore et al., 2019) for two of the four storms sampled by the stationary lidar.

With a detailed dataset of time-evolving beach morphology and swash variability at the intra-storm time scale, we primarily aim to address: *Is a pre-storm beach slope sufficient for characterizing morphologic controls on wave runup throughout storms?* Along this line of investigation, the data provide insight into both cross-shore and alongshore variability of beach morphology changes and the accuracy of empirical runup models throughout tropical and extratropical storms. Section 2.3 describes the field site, wave and water level conditions during the four storms, the methods for utilizing the stationary and mobile lidar data, and the methods for calculating foreshore beach slope. Study results, including descriptions of the evolving beach throughout each storm, observations and parameterization/predictions of runup, and the effects of beach cusps on runup prediction skill are discussed in section 2.4. In section 2.5, we investigate the performance of other commonly used runup parameterizations, use the mobile lidar system to establish how localized the observed beach cusp field is, and assess the scales of beach slope variability at this site. Finally, we summarize our key findings in section 2.6.

2.3 Methodology

Observations of dune and beach morphology, wave runup, and offshore oceanographic conditions were collected at the ERDC FRF. Our dataset includes concurrent observations during four storms: Hurricane Joaquin (Sept 30, - Oct 8, 2015), a Nor'Easter (Feb 7 - 11, 2016), Hurricane Jose (Sept 18 - 21, 2017), and Hurricane Maria (Sept 25 - 28, 2017) and span conditions $5.4s < T_p < 16.7s$ and $0.8m < H_s < 4.2m$ in 8 m depth. The following subsections describe these field datasets.

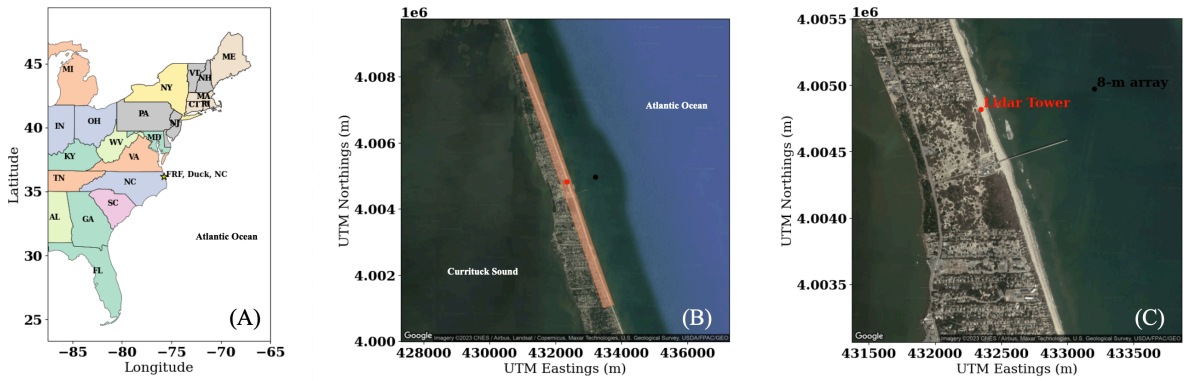

Figure 2.1. (A) Location of the Field Research Facility (FRF) in the eastern region of the United States, (B) the area of Duck, NC that was mapped by CLARIS (shaded orange region), and (C) the locations of the lidar tower and the 8 m pressure array on the FRF property.

2.3.1 Study Site

The FRF is located in Duck, NC, USA, a heavily studied, dune-backed, intermediate beach (foreshore slope $\sim$ 0.08 (O'Dea, Brodie, 2019; Holland, Holman, 1996; Holland, 1998)) in the Outer Banks (Birkemeier et al., 1996; Holman, 1986; Holman, Sallenger Asbury H., 1993), located between the Atlantic Ocean to the east and Currituck Sound to the west (figure 2.1). The sandy beach is comprised of a bimodal mixture of coarse and fine sand, 1 mm and 0.3 mm, respectively (Birkemeier, Holland, 2000). Semi-diurnal tides in this area have a $\sim$ 1 m range (Lee et al., 1998). The Outer Banks are subject to Nor'Easters, extra-tropical storms that develop in the mid-latitudes and typically occur in the fall, winter, and early spring, and tropical storms and hurricanes that pass over the Outer Banks in summer and early fall (Brodie, 2010). Both types of storms generate high wind conditions that drive large waves.

2.3.2 Morphology Data

Stationary Lidar Measurements

A Riegl terrestrial lidar scanner (VZ-1000, 1550 nm laser with a 0.3 mrad beamwidth) mounted on a 4 m boom over the dune recorded elevation data along a cross-shore line at approximately 7.1 Hz for the first 30 minutes of every hour. These scans were oriented offshore and span about 65 m, which encompassed the dune crest, beach face, swash zone, and inner surfzone (Brodie et al., 2015; O'Dea et al., 2019). During the subsequent 30 minutes, the lidar conducted a 237 ^{o} framescan to obtain alongshore elevation measurements over a 500 m range. The location of this scanner is shown in figure 2.1C. An hourly co-registration was completed as part of the data analysis to account for small movements of the lidar platform and to therefore reduce offsets in the x-, y-, and z- planes caused by thermal or wind effects on the lidar mounting system. The raw data were transformed from the scanner's own coordinate system into a rectified Cartesian coordinate system with NAVD88 as the vertical datum and a local geo-referenced horizontal coordinate system (xFRF, yFRF). The data also were filtered to remove noise, such as sea spray and vegetation, and linearly interpolated onto a 10 cm grid as described in O'Dea et al. (2019). The gridded lidar data were used to define hourly bed elevation change patterns across the beach for each of the target storms.

CLARIS Surveys

To supplement the detailed measurements from a single location, larger scale spatial measurements of beach morphology over an 8 km coastal stretch in the same vicinity of the dune lidar are used here (figure 2.1B). A Riegl VZ-2000 terrestrial lidar system and Inertial Motion Unit (IMU) attached to the top of a van were driven along the Outer Banks coast to collect measurements in framescan mode of the beach/dune face. This system, referred to as the Coastal Lidar and Radar Imaging System (CLARIS), provided detailed spatial measurements of beach and dune morphology with vertical errors less

than 0.05 m (Cohn et al., 2022). Ground points from the lidar, determined through filtering of the raw data using standard Riegl terrain filters, were then interpolated on a 25 cm by 25 cm grid as outlined by Spore et al. (2019). Surveys conducted on 9/18/2017 (before Hurricane Jose), 9/22/2017 (after Hurricane Jose and before Hurricane Maria), and 9/29/2017 (after Hurricane Maria), which covered about 8 km (4.1 km north and 3.9 km south of the stationary lidar platform) of the coast, were used in this analysis. The dataset encompassed both nourished (from a June 2017 project) and un-nourished sections of the beach. The mean interpolated contour used for wavelet analysis was extracted from the dataset by first establishing the 2.0 m and 1.8 m elevation contours, due to widespread data availability at these elevations on the dry beach as opposed to more intermittent returns closer to the water line. The average difference between the two contours was calculated for all alongshore positions in which both contours were present. A mean contour was calculated, and the average difference was used to estimate the mean in areas in which only one of the 2.0 or 1.8 m contours was present. We linearly interpolated through the remaining alongshore locations in which no contour was present. A 10 m moving mean was applied to the interpolated mean contour, and finally the larger shoreline trend was removed by subtracting the contour with an applied Savitzky-Golay filter with a 505 m window. This approach was used to isolate the wavelengths of beach cusps and to ignore the effects of a larger shoreline wavelength trend. To analyze the spatial behavior of the beach cusp field over these 8 km, continuous Morse wavelets were used on the resulting mean contours from each CLARIS dataset, similar to the analysis in Matsumoto et al. (2020).

Beach Slope Definitions

Beach slope is a primary factor for controlling wave runup. For the purposes of this work we calculated three different beach slopes as follows:

- Observed beach slope (β_{obs}) is calculated on an hourly basis from the lidar-measured

beach profiles in the foreshore region, which is defined as the mean horizontal swash position +/- 2 standard deviations of the observed swash timeseries for each 30 minute window. β_{obs} is defined here as the slope of the best fit line using linear regression within this foreshore region. We consider this the 'ground truth' beach slope timeseries.

- Pre-storm beach slope (β_0) uses the lidar-measured pre-storm beach profile as shown in figure 2.4. The hour that each pre-storm profile was observed is denoted by the stars in figure 2.6. These hours were specifically chosen because they were at low tide, exposing the most beach, and because the beach changed little in the hours prior. The mean swash position was predicted using offshore conditions and the parameterization for setup as given by Stockdon et al. (2006). A detailed explanation of this process is described later in this section.

- Time-varying beach slope ($\beta(t)$) uses hourly lidar-measured beach profiles with predicted setup generated by the same process as that used for β_0. This differs from β_{obs} in that the foreshore slope is defined over a region that is empirically predicted (as opposed to measured) in $\beta(t)$.

The differences between these definitions of beach slope are further illustrated by an example in the Appendix.

To calculate β_0 and $\beta(t)$, we assume that we cannot directly measure the runup during the storm to obtain the mean swash position. Thus, we use the expression for predicting setup from Stockdon et al. (2006):

$$\eta = 0.35\beta\sqrt{(H_0 L_0)} \tag{2.1}$$

In Stockdon et al. (2006), a portion of the data used to tune the parameterization was collected at the FRF study site, including during energetic wave conditions, thus

we expect it to outperform other existing parameterizations. To predict hourly β, and therefore runup, we begin with a pre-storm beach profile as our starting estimate using β_{obs}. For the next hour, we take the beach profile (the pre-storm profile again if estimating β_0 or the lidar-measured profile for that hour if estimating $\beta(t)$), calculate setup using equation 2.1, add the estimated setup to the water level measured at the tide gauge for that hour, and find where this water level intersects the beach (mean swash position). For simplicity, we used the mean standard deviation of the horizontal swash position as measured by the lidar to establish the foreshore region (+/- 2 standard deviations from the mean swash position) to obtain the linear best fit line to estimate beach slope. Once we obtain this beach slope estimate, we repeat the process for the same hour until the estimate for beach slope asymptotes. This entire process is repeated for the remaining hours using the previous hour's estimate for β as the starting point to obtain the timeseries for β_0 and $\beta(t)$. We also calculated curvature of the beach using the coefficient of the x^2 term of a second order polynomial fit for the area over which β_0 and $\beta(t)$ were calculated. If values of curvature fell outside of two standard deviations from the mean, we assumed these beach slope values were unrepresentative of the foreshore beach and excluded them from our timeseries.

Skill Calculations

To assess model performance in estimating wave runup, we utilized the definition of $Skill = 1 - NMSE$, where NMSE (normalized mean square error) is as follows:

$$NMSE = \frac{\Sigma_{i=1}^{n}(p-o)^2}{\Sigma_{i=1}^{n}(o-\bar{o})^2} \tag{2.2}$$

where p is the runup prediction and o is the lidar-derived runup observation.

2.3.3 Oceanographic Conditions

Offshore Wave and Water Level Properties

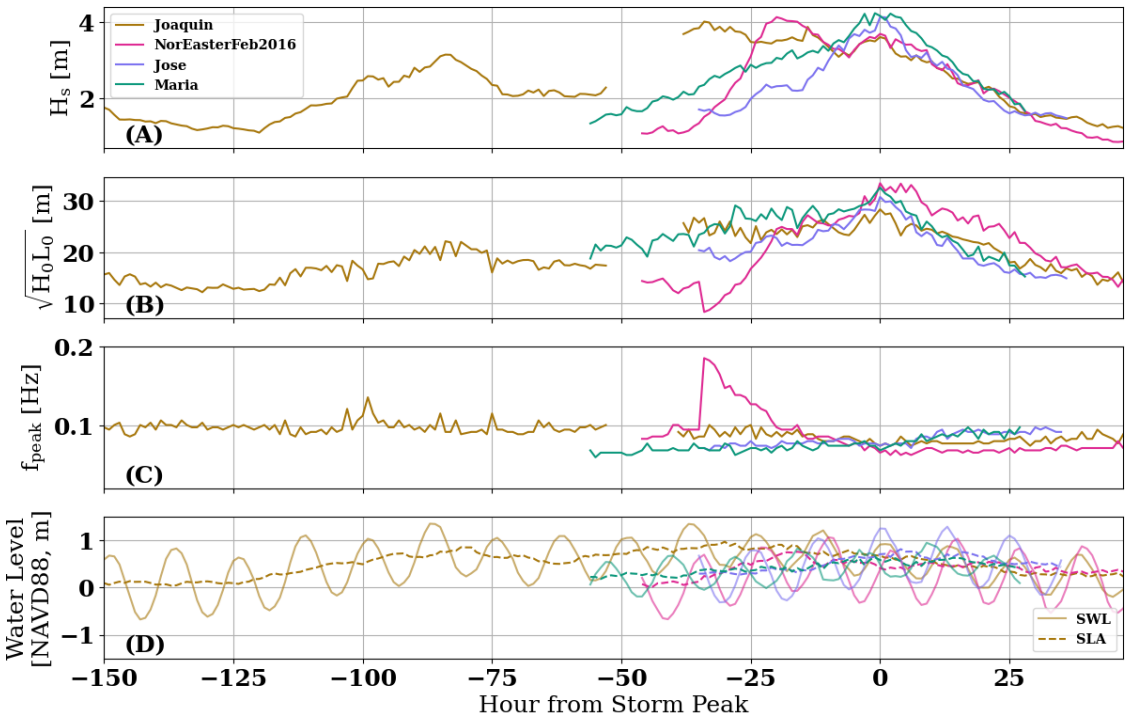

Figure 2.2. (A) Significant wave height as measured by the 8 m pressure array, (B) runup proxy $\sqrt{H_0 L_0}$ extrapolated from 8 m pressure array measurements of H_s and T_p, (C) peak frequency as calculated from hourly 8 m pressure array data, (D) hourly still water level (SWL, solid line) and sea level anomaly (SLA, dashed line) measured by FRF end-of-pier (EOP) NOAA station 8651370. Lines are colored by storm dataset as indicated by the legend in panel (A).

Significant wave height (H_s), wave direction (θ) and directional spread (θ_{spread}), and peak frequency (f_{peak}) were specified using a pressure array in 8 m depth offshore of the FRF property (figure 2.1C). Deep water significant wave height (H_0) and wavelength were calculated by back refracting significant wave height and peak period recorded by the 8 m pressure array.

All four storms reached maximum $H_s > 4.0$ m as recorded at the 8 m pressure array (figure 2.2A). Deep water wave height and wavelength were used to calculate a

runup proxy, $\sqrt{H_0 L_0}$, following the runup parameterization from Stockdon et al. (2006) (figure 2.2B). We assume that the hour of highest runup corresponds with the hour of maximum $\sqrt{H_0 L_0}$, and thus set this hour as "Hour 0", or the storm peak, for each storm timeseries. This allowed us to align the time axes for all storms, despite each timeseries being a different length. Maximum values of $\sqrt{H_0 L_0}$ ranged from 29.3 m (Joaquin) to 36.0 m (Nor'Easter) (figure 2.2B). Although this runup proxy has a stronger dependency on period than wave height, since $L_0 \propto T^2$, the peak runup proxy does not correspond to the hour of lowest frequency, because wave height and frequency do not change concurrently and the runup proxy is dependent on both factors.

Hurricanes Jose, Maria, and Joaquin maintained similar and steady f_{peak} of ~ 0.09 Hz throughout their timeseries, whereas the Nor'Easter began in the higher frequencies and then decreased over the course of 25 hours to a peak frequency of ~ 0.07 Hz (figure 2.2C). This decrease in frequency is characteristic of Nor'Easters in the Outer Banks, as wind driven seas tend to precede the incoming storm swell (Brodie, 2010).

For all storms, incoming waves were oriented in approximately the shore-normal direction at the storm peak and subsequently. However, for Jose and Maria, we note higher variability in θ_{spread} throughout the timeseries, while the directional spread is roughly maintained between 18 and 35 degrees surrounding the storm peaks for Joaquin and the Nor'Easter (not shown). These storm characteristics are within the range of values reported from numerous previous studies (Holland, Holman, 1996; Miller et al., 1989; Lee et al., 1998; **?**; Holland, 1998), suggesting that the target storms of interest are not uncommon events at this site.

Water level observations were taken from the NOAA tide gauge at the end of the FRF pier (figure 2.2D). The sea level anomaly (SLA) is the observed still water level (SWL) at the tide gauge with the predicted astronomical tidal water level removed. Here we define total water level (TWL) as the observed SWL plus the lidar observed $R_{2\%}$, which includes both wave setup and swash.

Lidar-Derived Wave Runup

From the stationary lidar outputs (Section 2.2.1), the runup tongue was identified following the methods outlined in Brodie et al. (2015). To reduce noise at the seaward end of mean hourly beach profiles, any elevation data observed less than 1.5% of the number of returns per cross-shore position were assumed to be water elevation or sea spray and were removed. Then a moving standard deviation with a window of 1.5 m in the cross-shore was applied to the elevation data, and areas in the seaward edge of the profile with a standard deviation higher than 5 cm were removed. Finally, the profile was smoothed using a 1.5 m running mean at the seaward edge of the profile and data with an upward slope over a 1 m horizontal distance were removed.

Empirical Runup Prediction

As part of this study, we aim to assess the skill of runup predictions using a beach slope generated from a fixed 'pre-storm' beach profile as opposed to a time-varying beach profile. We use the runup parameterization from Stockdon et al. (2006) (referred to as Sto06), given by:

$$R_{2\%} = 1.1\left(0.35\beta\sqrt{(H_0 L_0)} + \frac{\sqrt{H_0 L_0(0.563\beta^2 + 0.004)}}{2}\right) \tag{2.3}$$

where β is the foreshore beach slope and H_0 and L_0 are the deep-water wave height and wavelength calculated from the 8 m pressure array, respectively. This formulations has a stronger dependence on wave period than wave height since $L_0 \propto T^2$.

For hours in which the Iribarren number ($\xi = \frac{\beta}{\sqrt{H_0/L_0}}$) was less than 0.3 (i.e. a dissipative state), we use the dissipative equation from Stockdon et al. (2006), given by:

$$R_{2\%} = 0.043\sqrt{H_0 L_0} \tag{2.4}$$

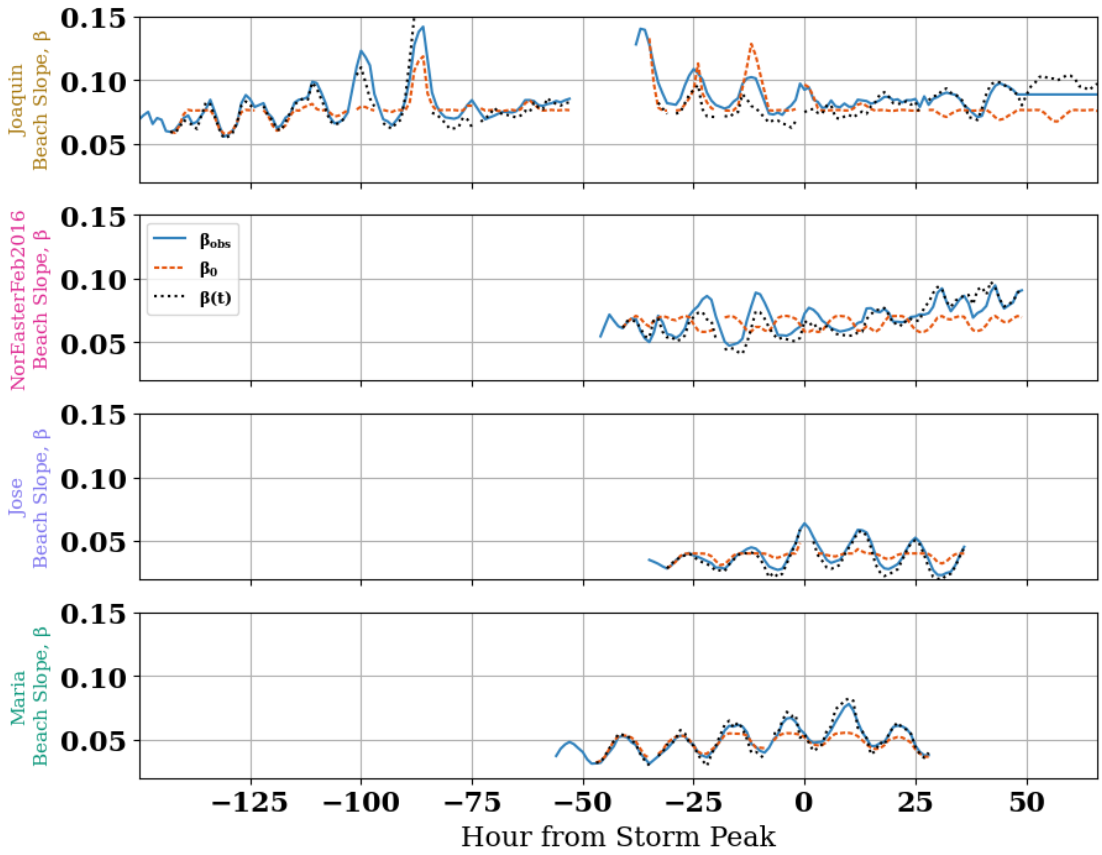

Figure 2.3. Timeseries of beach slope calculated from hourly beach morphology and runup observations (β_{obs}), pre-storm beach profile and predicted setup (β_0), and hourly beach profiles and predicted setup ($\beta(t)$) for each storm.

However, this dissipative state is observed for only 10 hours of the Jose timeseries, which accounts for 14% of the Jose runup timeseries and 2% of the combined storm runup timeseries.

2.4 Results

2.4.1 Intra-Storm Beach Evolution

We calculate the three beach slope definitions as described in section 2.2.3: β_{obs}, β_0, and $\beta(t)$ (figure 2.3). For each storm, as expected, the time-varying beach slope, $\beta(t)$,

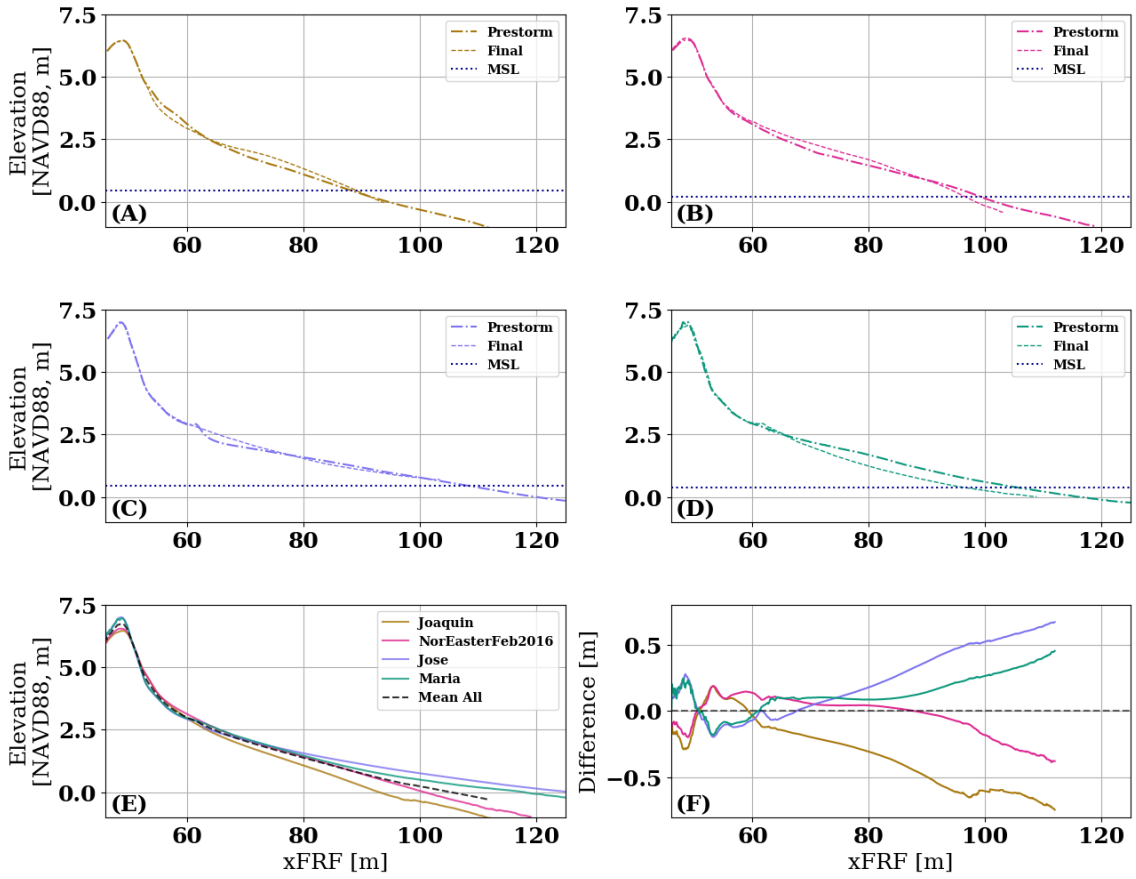

Figure 2.4. 10 cm gridded pre-storm (solid, colored by storm) and final (dashed) beach elevation profiles for (A) Hurricane Joaquin, (B) the Nor'Easter, (C) Jose, and (D) Hurricane Maria as measured by the stationary lidar. Mean sea level (MSL) for each dataset is indicated by the horizontal dotted blue line. (E) Mean profiles for each storm and mean profile of all storms combined as indicated by the dashed black line. (F) Difference of mean profile of each storm from overall mean profile.

closely follows the observed beach slope β_{obs}. The beach slope based on a pre-storm profile, β_0, oscillates between over- and under- predicting β_{obs}. To further assess the observed and calculated beach slopes, we examine the intra- and inter- storm variability in beach profiles, as shown in figures 2.4 and 2.5. For hurricanes Jose and Maria, the beach began as a more planar wide beach than during Joaquin and the Nor'Easter (figure 2.4E & F). Of the 4 target storms, the maximum local bed elevation change recorded was -0.46 m (Maria) and up to 0.30 m of local beach aggradation was observed (Jose). Overall, the

mean bed elevation change across the beach, measured from 50 m $\leq$ x $\leq$ 120 m in the cross-shore for location where data was available, was 0.06 m, 0.06 m, 0.02 m, and -0.23 m for Joaquin, the Nor'Easter, Jose, and Maria, respectively. The spatial distribution of these changes was not uniform. For Joaquin and the Nor'Easter in particular, by the end of the storm period the profile became more convex (centered around 75 m and 85 m in the local FRF coordinate system, respectively), while for Maria, the profile seaward of the dune face was mostly eroded, except for a small area around 62 m. During Jose, the beach generally changed little, but a $\sim$ 0.4 m scarp feature around 62 m was destroyed by the end of the storm period.

Despite the similarities in the magnitudes of the runup proxy $\sqrt{H_0 L_0}$ during the peak of each storm (Fig 2.2), the mean bed elevation change across the profile through the storm peak (hour 0), was quite different: -0.08, -0.08, 0.07, and -0,19 for Joaquin, the Nor'Easter, Jose, and Maria, respectively (Fig 2.5). These results demonstrate that the morphological evolution of the sub-aerial and sub-aqueous swash zone cannot be simply related to deepwater wave characteristics, total water levels, or swash parameterizations alone, and is instead the cumulative result of the interplay of complex processes which requires further investigation.

The timestacks in figure 2.5 show hourly elevation changes relative to the first hour for each storm. The lidar-derived TWL line (dashed black line on each timestack) indicates that most major elevation occurred seaward of the TWL line, as expected. Landward of this limit, changes may reflect the role of extreme runup (e.g., R_{max}) or aeolian processes. For Joaquin and the Nor'Easter, accretion of the upper/mid beach occurred on high tides (after hour -50 for Joaquin and for the majority of the Nor'Easter) with erosion of the lower beach occurring near low tides. During Maria, the beach profile eroded throughout the storm everywhere seaward of the TWL line. The elevation changes for Jose were generally less pronounced than the three other storms, although a net bed elevation lowering was observed seaward of the TWL location.

These patterns in bed elevation change have some influence on the resulting foreshore beach slope at both the tidal and storm timescale (Figure 2.3). The differences between the beach slopes using hourly profiles (β_{obs} and $\beta(t)$) and β_0, are partially due to the concavity of the profiles throughout the storms, notably Joaquin and the Nor'Easter. The estimated beach slopes increase with the tidal elevation and wave setup on the concave profile.

To characterize the net beach change, we calculate volume change timeseries for each event within the green dashed lines in figure 2.5. The elevation changes were assumed to be uniform in the alongshore over 1 m in order to convert to volume changes. Compared to the first hour of data collection for each storm, the maximum changes in volume were -6.2 (Joaquin), +7.7 (Nor'Easter), +2.8 (Jose), and -10.4 (Maria) m^3/m (figure 2.6).

2.4.2 Observations and Empirical Parameterization of Runup

Although continuous coastal morphologic measurement is rare, pre-storm beach morphology data is readily available for many coastal field sites from beach surveying (Spore et al., 2019; Agredano et al., 2019), airborne lidar (Burvingt et al., 2017), or satellite imagery approaches (Almeida et al., 2019). These pre-storm data often are used to define beach slopes within empirical parameterizations of wave runup for the purposes of characterizing coastal hazards. Here we compare the skill of calculated runup from Sto06 using our estimates of β_0 and $\beta(t)$, relative to lidar-derived runup. We aim to determine if runup estimates calculated from pre-storm profiles are accurate or whether a time-evolving profile is necessary to generate more reliable runup predictions. For both parameterization approaches, we used the hourly H_0 and L_0 generated from the 8 m array. The resulting timeseries of both empirically predicted and the lidar-derived $R_{2\%}$ are shown in figure 2.7.

For Hurricane Joaquin, the Sto06 skill using β_0 is low (0.09). Sto06 with β_0 notably tends to overestimate runup maxima near the peak hours of the storm: at hour -12, $R_{2\%}$ is overestimated by ~ 0.7 m when using β_0 as the model input. Skill increases to 0.30

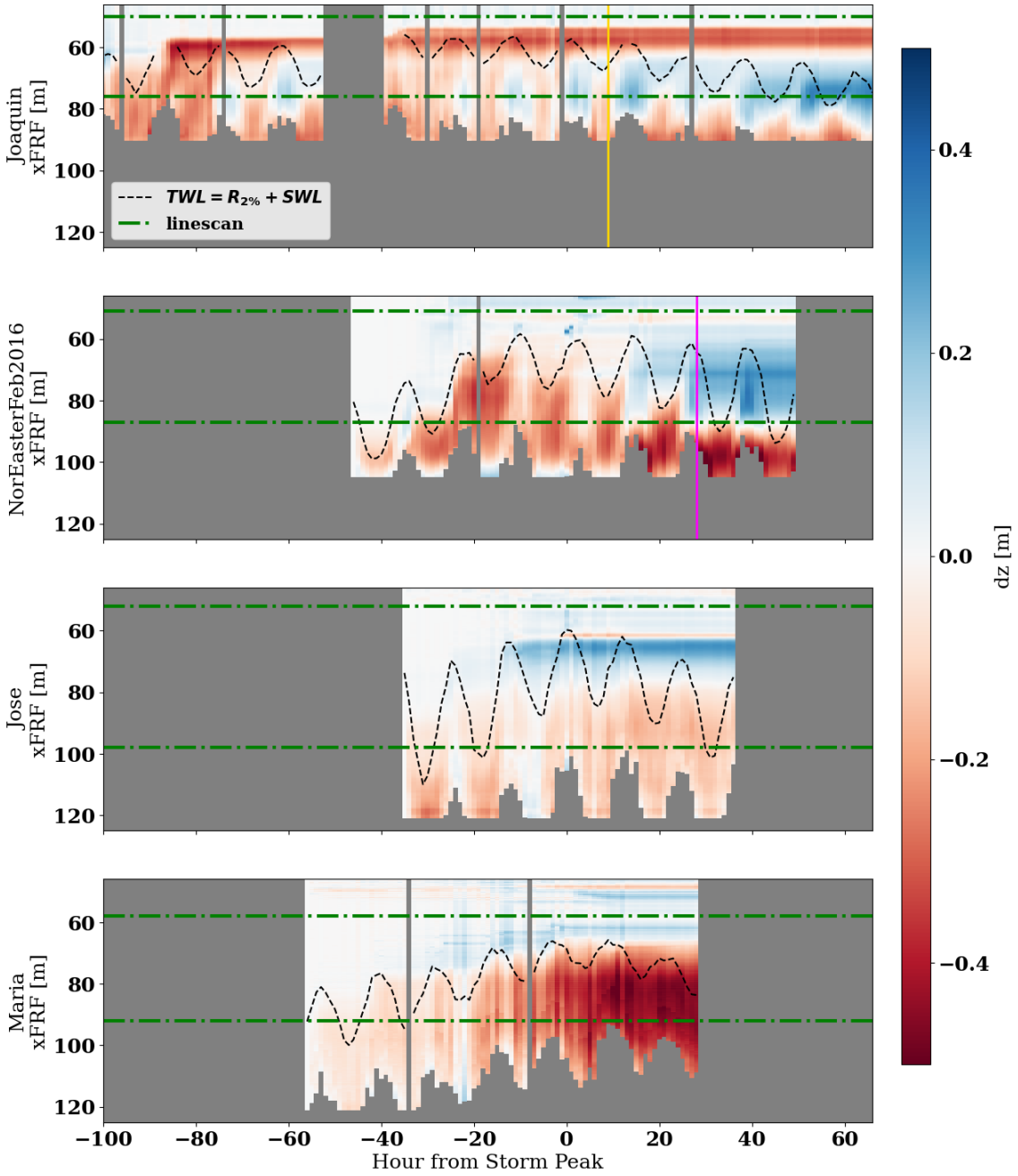

Figure 2.5. Hourly cross-shore elevation changes from the first hour of each storm. Blue indicates accretion and red indicates erosion. Cross-shore position of hourly TWL is shown as a black dashed line and limits of beach volume calculations are shown as dashed-dotted green lines. Hour of emergence of beach cusps is indicated by gold (Joaquin) and pink (Nor'Easter) solid vertical lines.

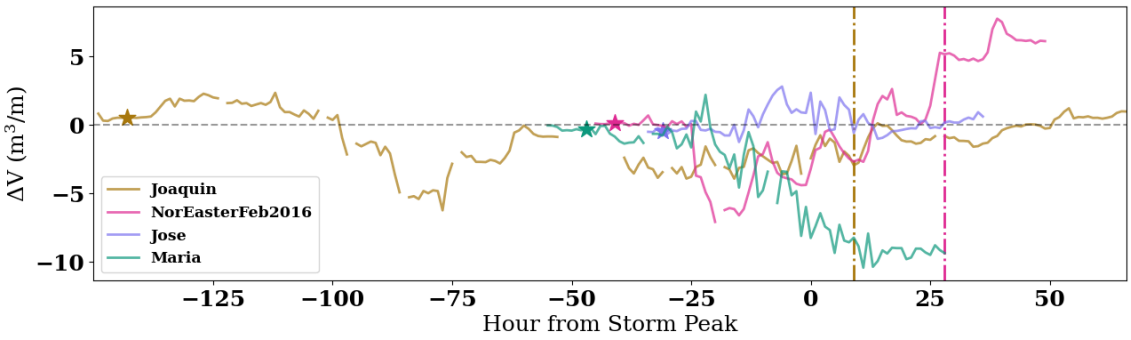

Figure 2.6. Hourly volume change from the first hour of each storm with cross-shore limits of calculation indicated in figure 2.5. Hour of emergence of beach cusps is indicated by gold (Joaquin) and pink (Nor'Easter) dashed-dotted vertical lines. Stars indicate the hour in which the pre-storm beach profile was identified.

if $\beta(t)$ is used in Sto06. Both parameterizations appear to underpredict runup maxima towards the beginning of the timeseries. For example, at hour -135, both parameterizations underpredict $R_{2\%}$ by about 0.4 m. Additionally, during the last 60 hours of the dataset, the parameterizations using β_0 and $\beta(t)$ underpredict runup by an average of 0.46 m and 0.33 m respectively. This coincides with a reduction in tidal variability of the observed runup timeseries.

For the Nor'Easter, skill also increases from 0.12 to 0.49 when $\beta(t)$ was used over β_0. However, both parameterizations underestimate runup maxima by up to 1.0 m in the last 40 hours of the data set when higher tidal variability is seen in the observed runup dataset. This increase in tidal variability enhances runup maxima to levels similar to those during the peak of the storm.

Skill of both parameterizations is relatively high (0.65 using β_0 and 0.49 using $\beta(t)$) when predicting runup during Hurricane Jose. This is likely attributed to the minor beach changes during this storm as shown in the beach profile change figures (figures 2.4 & 2.5) and the volume change timeseries (figure 2.6), and the dissipative state that the beach is briefly in for 3 of the observed low tides. Both parameterizations tend to capture the

runup maxima during this timeseries but slightly underpredict the minima after the peak of the storm.

During Hurricane Maria, the parameterizations predict runup with the least amount of skill. Throughout the storm, both parameterizations overpredict runup, however Sto06 using β_0 better recreates observed $R_{2\%}$ with a skill of 0.20 as opposed to -0.33 for Sto06 using $\beta(t)$.

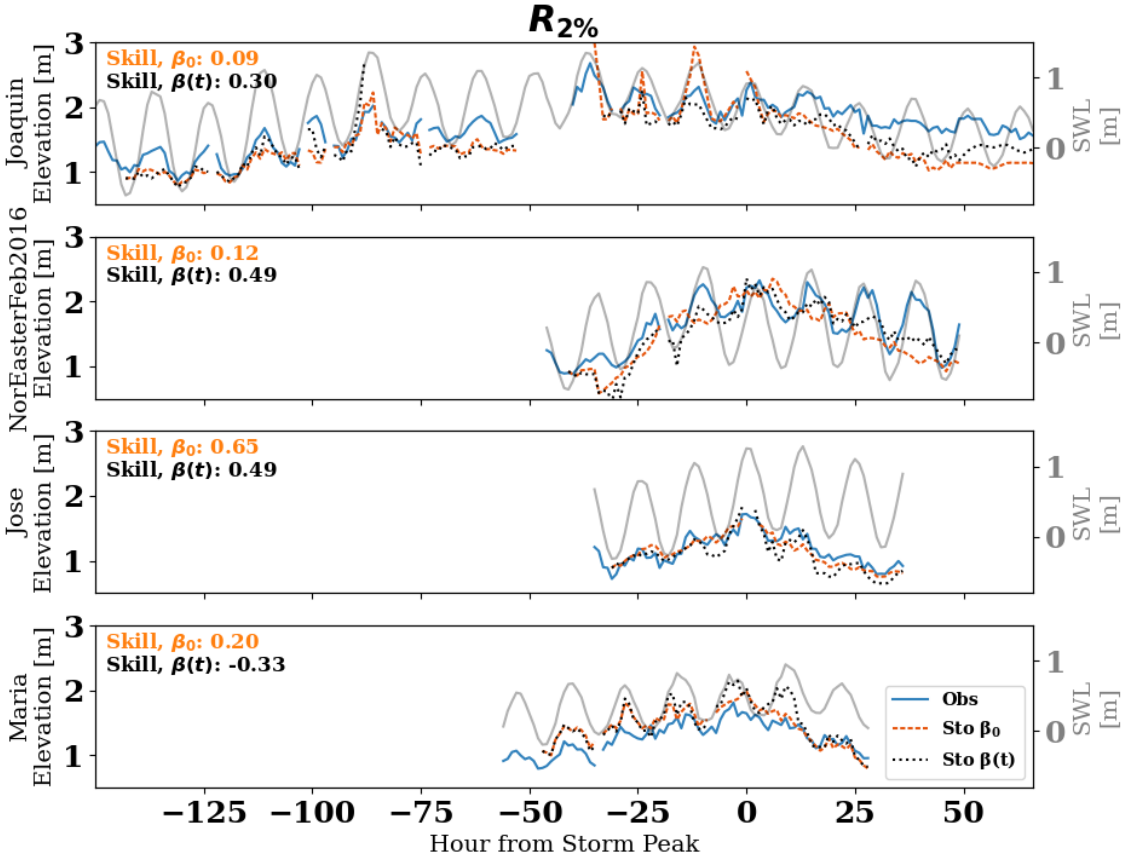

Figure 2.7. Observed (blue solid), predicted with β_0 (orange dotted), and predicted with $\beta(t)$ (black dotted) $R_{2\%}$ for each storm. Still water levels in the NAVD88 vertical datum as measured by the tide gauge on the FRF pier are shown on the gray twin axis.

2.4.3 The influence of beach cusps on runup

For approximately 60 and 40 hours after the storm peaks of Joaquin and the Nor'Easter, respectively, the observed runup events during high tides reached magnitudes nearly equal to the maximum runup for each storm (figure 2.7). Additionally, after hours ~ 9 and ~ 25 of Joaquin and the Nor'Easter, respectively, the magnitude of $R_{2\%}$ is not well captured by Sto06 (figure 2.7). The sustained high runup values and underprediction of $R_{2\%}$ post storm peak are not present in the Jose or Maria runup timeseries. We hypothesize that these discrepancies in observed versus estimated runup are due to alongshore variability in morphology, which limits treatment of runup as a purely cross-shore problem. To gain insight, we use the hourly framescans from the stationary lidar to qualitatively analyze the alongshore structure of the beach/dune face.

Around hour 9 of Hurricane Joaquin, beach cusps form with $\sim 30-40$ m wavelength (figure 2.8), which coincides with the sustained runup maxima and underprediction of $R_{2\%}$. These features are consistent which beach cusps observed in other studies at the FRF, including Holland, Holman (1996), Holland (1998), and Miller et al. (1989). The cusps increase in prominence by the end of the timeseries, reaching nearly 0.5 m in height. For the Nor'Easter, beach cusps of similar size and shape form beginning at hour 28. In contrast, during hurricanes Jose and Maria, the beach face did not develop rhythmic alongshore features. This suggests that sustained observed magnitudes of runup at high tides that are underpredicted may be related to the presence of beach cusps.

To further understand the effect of beach cusps on runup parameterizations, we split the storm datasets into hours without cusps (NC) and hours with cusps (CO). We analyze the ability of equation 2.3 to estimate $R_{2\%}$ using β_0 and $\beta(t)$ during these two time periods and assess the accuracy of each result by comparing skill, bias error (BE), root mean-squared error (RMSE), and the regression equation, shown in table 2.1. In the regression analysis, we assume that there was no error in the observed $R_{2\%}$ and 95%

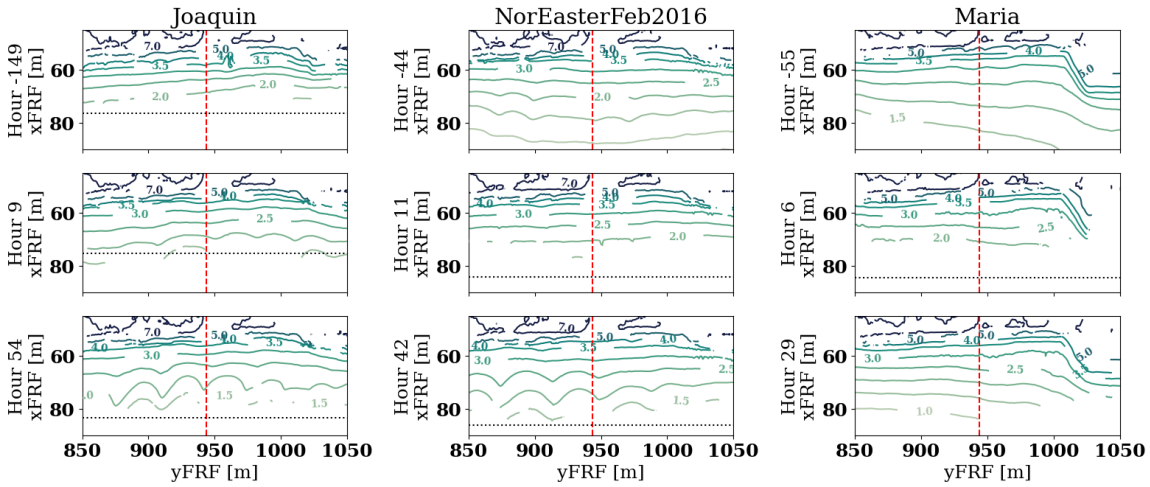

Figure 2.8. Contour plot of beach elevation during Hurricane Joaquin (left), the Nor'Easter (middle), and Maria (right) for three chosen hours. Jose is not shown because of its similar behavior to Maria. Contour levels are reported on the plot in units of m, NAVD88. The position of the lidar cross-shore scans are denoted by the vertical dashed red line, and the hourly mean swash position, if present in the chosen domain, is denoted by the horizontal dotted black line. The abrupt increase in sand volume around yFRF=1025 m for Hurricane Maria is due to the nourishment that was placed near the north end of the FRF property in June 2017.

confidence intervals are reported with all regression slope and intercept values.

Table 2.1. Table of model error. Dataset, skill (as calculated by equation 2.2), mean error percentage (error %), bias error (BE), root mean-squared error (RMSE), and regression slope (m) and intercept (b) with 95% confidence intervals shown in parentheses. 'NC' indicates dataset compiled from all storms without hours where cusps were observed and 'CO' indicates dataset compiled from Joaquin and the Nor'Easter with hours where cusps were observed only. Errors are reported in units of m.

Dataset	Skill	Error %	BE [m]	RMSE [m]	m	b
β_0, NC	0.57	1.3%	-0.02	0.26	1.0 (0.4)	0.1 (0.6)
$\beta(t)$, NC	0.56	5.1%	0.02	0.26	0.9 (0.4)	0.1 (0.6)
β_0, CO	-2.55	8.2%	0.44	0.24	0.6 (0.3)	0.2 (0.6)
$\beta(t)$, CO	-0.86	8.2%	0.28	0.21	0.6 (0.3)	0.5 (0.5)

For the NC dataset, using β_0 or $\beta(t)$ in Sto06 (equation 2.3) yields similar regression equations and skill values (figure 2.9, table 2.1). The root mean square error (RMSE) and mean bias error (BE) were both 0.26 and $|0.02|$, respectively, for the NC β_0 and $\beta(t)$ cases.

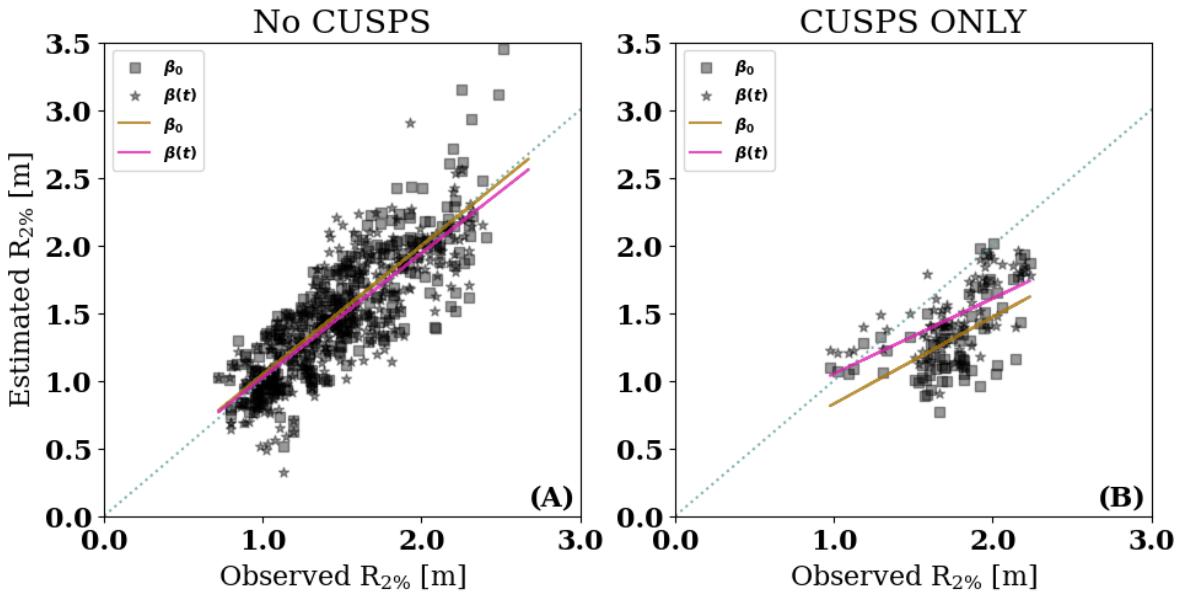

Figure 2.9. Stockdon estimates of $R_{2\%}$ versus observed values (A) using equation 2.3 with β_0 (squares, gold trendline) and $\beta(t)$ (stars, pink trendline) for all hours without cusps present; (B) same as (A) but for all hours with cusps present. The 1:1 line is shown as a light gray dotted line.

However, error percentage increased from 1.3% for the β_0 case to 5.1% for the $\beta(t)$ case. For the CO dataset, there is a large decline in skill and an increase in error percentage for both types of parameterizations. The negative skill values for the β_0 (skill=-2.55) and $\beta(t)$ (skill=-0.86) parameterizations indicate that Sto06 does not perform any better than using the mean value as a model for time periods where cusps are present. These results suggest that for empirically calculating wave runup, the pre-storm beach morphology is just as good, if not better, for defining runup than the availability of continuously evolving topography. However, they also indicate that Sto06 breaks down when the beach becomes highly variable in the alongshore, whether there are accurate measurements of cross-shore morphology or not.

2.5 Discussion

2.5.1 Insights from New Intra-Storm Runup and Morphology Observations

Typically field observations of storm-induced morphologic changes to coastal beach systems are only available from pre- and post-storm surveys that may have occurred relatively far from the date of the event. Consistent with the few other datasets of $\sim$ hourly scale morphological changes during storms, these data from Duck, NC, USA indicate that beach changes are complex in both the cross-shore and temporal dimensions at the event scale. In the case of Hurricane Joaquin, the onset of the event triggered substantial erosion from the water line to the back of the beach. While the beach scarp was maintained throughout the remainder of the storm, the beach morphology continued to evolve considerably with beach volume losses mostly recovering over the following 5 days. Despite a typical conclusion that storms are broadly erosional to the beach, the upper portion of the foreshore instead accreted due to swash processes during the 2016 Nor'Easter and Hurricane Jose. Across all events, the bed elevation locally changed by upwards of 20 cm (either accretion or erosion) and, as such, these morphologic changes have important implications on the instantaneous foreshore slope. While these net slope changes across the intertidal zone (e.g., from MLW to MHW) were non-negligible over the course of the storm, it is important to note that that the formal definition of foreshore slope that has time variable vertical limits depending on the swash itself results in broad slope variability on the sub-daily timescale associated with fluctuations in the tides. Therefore use of a static slope value, such as between MHW and the dune toe that is commonly used for hazard studies, is likely to under-resolve morphologic effects on runup extremes. However, incorporating the full pre-storm profile to iteratively develop time-variable foreshore slope estimates may serve to enhance predictions when intra-storm morphology data is not broadly available.

Although the cross-shore linescans indicate intra- and inter- storm morphologic variability, our results suggest that alongshore variability due to beach cusps has a greater effect on the skill of Sto06 in predicting runup than the variability in foreshore beach slope throughout the storm. If beach cusps are not present, an estimate of beach slope using a pre-storm beach profile seems sufficient to predict runup throughout a storm. However, if beach cusps are present, then runup predictions using Sto06 are likely an underestimate.

2.5.2 How do other empirical runup parameterizations perform?

While Stockdon et al. (2006) remains the most widely used empirical formula for wave runup prediction on sandy coastal systems, numerous other parameterizations exist in the literature that synthesize the role of wave height, wavelength, and beach morphology on wave runup in different ways. To examine the generality of our results, we investigate the skill of other common runup parameterizations at the FRF property. Specifically, we compare the performance of five additional commonly used empirical parameterizations (as shown in a table 2.2) using β_0 and $\beta(t)$ during the NC time periods. For the parameterization from Holman (1986), we use the formulation based on the relationship between the non-dimensional runup and the Iribarren number (Hol86); for the parameterization from Nielsen (2009), we use the formulation for extreme runup heights (Nie09) with $Z_{100} = 0$ since we are not adding SWL to our other $R_{2\%}$ predictions and Z_{100} is often approximated at SWL (Atkinson et al., 2017); and for the parameterization from Atkinson et al. (2017), we use the M2 model of models since it yielded the smallest error in the original study (Atk17). The results of these analyses are shown in figure 2.10.

Overall, the parameterization from Ruggiero et al. (2001) (Rug01) and Sto06 have the highest skill in predicting $R_{2\%}$ using both β_0 (0.61 for Rug01, 0.57 for Sto06) and $\beta(t)$ (0.60 for Rug01, 0.56 for Sto06). Both these parameterizations were tuned using data from our study site, which liekly explains their high skill overall. The skill of the

parameterization from Vousdoukas et al. (2012b) (Vou12) slightly decreases from 0.47 using β_0 to 0.35 using $\beta(t)$. Faro Beach, the study site at which the Vou12 parameterization was formulated, is generally a more reflective and steep beach than our study site. For Hol86 and Atk17, which are similar parameterizations, skill increases from 0.29 (Hol86) and 0.18 (Atk17) when using β_0 to 0.44 (Hol86) and 0.35 (Atk17) when using $\beta(t)$. Although Hol86 was calibrated using data from our study site and encompassed two storms, the three week study period did not cover the recovery period following the second storm and did not account for a wide range of beach states. Alternatively, Atk17 was not assessed under extreme wave conditions, and the authors note that this is an explicit limitation of the model (Atkinson et al., 2017), which may explain it's low performance during our storm periods. Nie09 performed most poorly in predicting $R_2\%$, which could be attributed to the model's tuning on a range of 6 Australian beaches.

All models utilize a factor of $\sqrt{H_0 L_0}$ (except Nie09, which uses the analogous $\sqrt{H_{rms} L_0}$), with coefficients that were tuned using different datasets from various study sites. Similar to Sto06, the formulations have a stronger dependence on wave period than wave height. Thus, the result that Sto06 and Rug01 were the most skillful parameterizations in predicting $R_{2\%}$ is expected, since they utilized datasets from the FRF. Generally, Sto06 is a model with predictive skill over a wide variety of beaches (**?**), so it's performance here is consistent with previous studies. Collectively there is not a uniform response in the runup models when using time-varying instead of pre-storm beach morphology, so we cannot conclude that a pre-storm morphology is sufficient in predicting storm driven runup for all parameterizations.

2.5.3 How localized are the beach cusps?

The initial lidar analysis indicates that there was complex spatio-temporal behavior in beach morphology at the study site. However, the stationary lidar system has a restricted $\sim$ 500 m field of view which (1) may limit the ability to observe longer wavelength cusp

Table 2.2. List of abbreviations, $R_{2\%}$ equations, and references for empirical runup parameterizations. The variables not previously defined in the text are: $L_R = 0.6 \tan\beta\sqrt{H_{rms}L_0}$ for $\tan\beta > 0.1$ or $L_R = 0.06\sqrt{H_{rms}L_0}$ for $\tan\beta < 0.1$ (Nielsen, 2009), Z_{100} which is defined as the highest elevation passed by all waves (Nielsen, 2009), and $H_{rms} = H_s/\sqrt{2}$. The py-wave-runup toolbox used to calculate predicted runup with these parameterizations is found on GitHub (Leaman et al., 2020).

Abbrev.	$R_{2\%}$ Equation	Reference
Sto06	$R_{2\%} = 1.1\left(0.35\beta\sqrt{(H_0L_0)} + \frac{\sqrt{H_0L_0(0.563\beta^2+0.004)}}{2}\right)$	Stockdon et al. (2006)
Hol86	$R_{2\%} = 0.83\tan\beta\sqrt{(H_0L_0)} + 0.2H_s$	Holman (1986)
Nie09	$R_{2\%} = 1.98L_R + Z_{100}$	Nielsen (2009)
Rug01	$R_{2\%} = 0.27\sqrt{\beta H_0L_0}$	Ruggiero et al. (2001)
Vou12	$R_{2\%} = 0.53\beta\sqrt{(H_0L_0)} + 0.58\xi\sqrt{(H_0^3/L_0)} + 0.45$	Vousdoukas et al. (2012b)
Atk17	$R_{2\%} = 0.92\tan\beta\sqrt{(H_0L_0)} + 0.16H_0$	Atkinson et al. (2017)

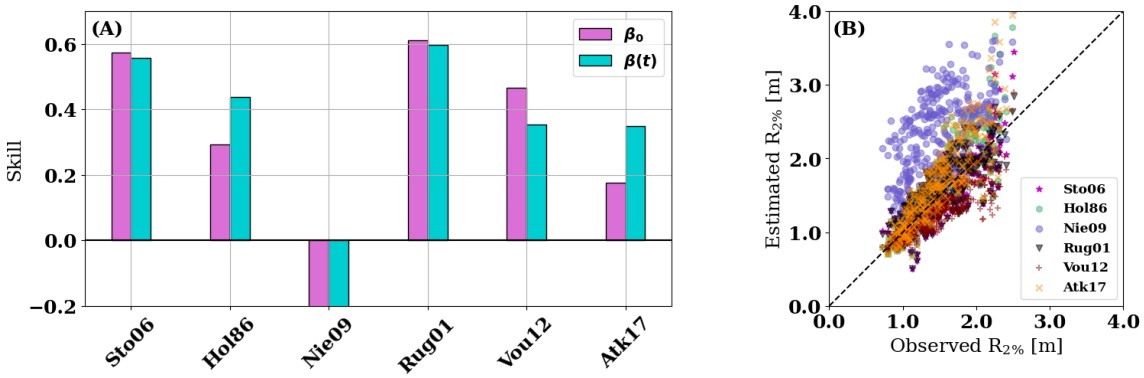

Figure 2.10. (A) Skill for $R_{2\%}$ calculated from empirical models described in table 2.2 using β_0 and $\beta(t)$ (colors shown in legend). The magnitude of Nie09 skill in both cases is greater than -4, which goes beyond chosen limits. (B) Model-predicted versus observed $R_{2\%}$ for the NC dataset using β_0. Model markers are listed in legend. 1:1 line is shown as dashed black line.

features and (2) does not in itself indicate whether these cusp behaviors are highly localized or representative of the broader region. To gain a sense of how localized the small wavelength (< 40 m) beach cusp features were, we analyzed the regional CLARIS mobile terrestrial lidar data that was available for hurricanes Jose and Maria. The 8 km elevation maps with a 505 m wavelength trend removed for 9/18/2017, 9/22/2017, and 9/29/2017 are shown in figure 2.11. A beach nourishment was completed between approximately 1100 m and 3200 m yFRF in 2017, resulting in large temporary increases in the beach width in this area. Unsurprisingly, we observed some 'leakage' of sediment from the nourishment, including within the stationary lidar field of view, as shown in the framescans in figure 2.8. For the purposes of this subsection we refer to the zones observed by the CLARIS system as the south (-3000 m to 1100 m yFRF), the nourishment (1100 m to 3200 m yFRF), and the north (3200 m to 5000 m yFRF). The position of the cross-shore linescans (yFRF = 945) is marked on the elevation map (figure 2.11), which is in the south zone.

As the storms passed over the region, beach cusps of similar magnitude to those observed during Joaquin and the Nor'Easter formed throughout this regional section but were especially prominent in the south. In the nourishment, larger wavelengths cusps are qualitatively apparent as well, especially in the 9/22/2017 elevation map (figure 2.11). To quantify these changes, we generate an elevation change map, by subtracting the 9/22 map from the 9/29 map (Note: we do not use the 9/18 map due to missing data in the nourishment zone), and establish a no change contour to use in a wavelet analysis (figure 2.12). We observe higher frequency movement of the contour in the south that is less prominent in the nourishment zone or the north. The wavelet shows that there is energy in the 20-50 m cusp band, with some persisting in the megacusp band, in the south. In the nourishment zone and the north, we see most of the energy in the megacusp band with some 20-50 m cusp energy (figure 2.12). These results suggest that the wider, flatter beach in the nourishment zone may inhibit movement of cusps and megacusps.

These regional analyses indicate that beach cusps are not localized to the 200 m

around the cross-shore lidar scans. For Jose and Maria, cusps were not present in the 3D stationary lidar framescans, but CLARIS data shows that they are prominent in almost all other parts of the region. These results show that beach cusp fields are non-uniform in presence and behavior, which when combined with the results from section 3.3 that show that runup behavior is difficult to predict where beach cusps form, offer a complex look at runup on a 3D variable beach.

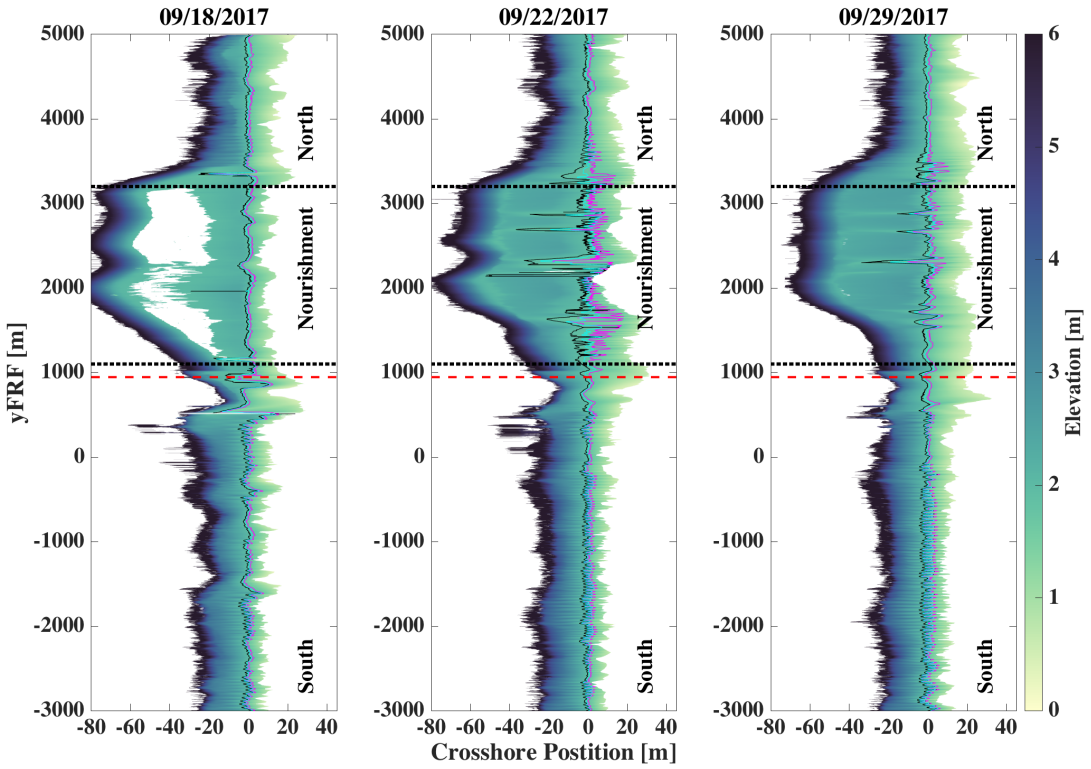

Figure 2.11. Elevation maps of CLARIS gridded data for 9/18/17, 9/22/17, and 9/29/17 with 505 m trend removed. The 2.0 m (black), 1.8 m (magenta), and mean interpolated (cyan) contours are marked by solid lines. Location of cross-shore linescans are denoted by dashed red line. Nourishment boundaries denoted by dotted black line. Elevation is reported in the NAVD88 datum.

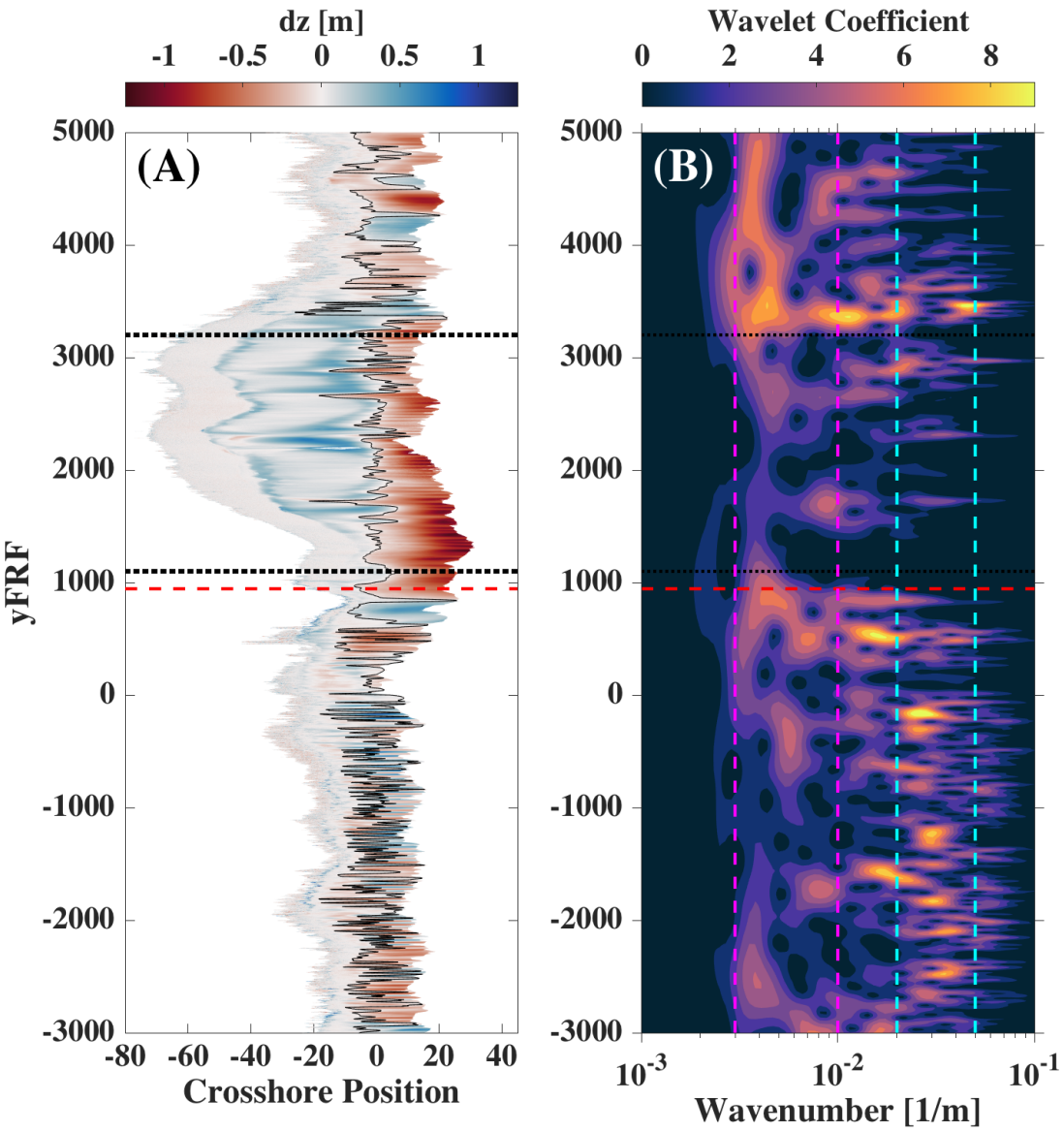

Figure 2.12. (A) Elevation map of difference between 9/29/17 and 9/22/17 CLARIS datasets with 0 m change contour marked by solid black line. Location of cross-shore linescans are denoted by dashed red line. Nourishment boundaries denoted by dotted black line. (B) Wavelet of 0 m change contour marked in panel (A). Positions of cross-shore lidar scans and nourishment boundaries denoted by dashed red line and dotted black lines, respectively. 20-50 m cusp wavenumbers and 100-330 m megacusp wavenumbers are marked by dotted blue and pink lines, respectively.

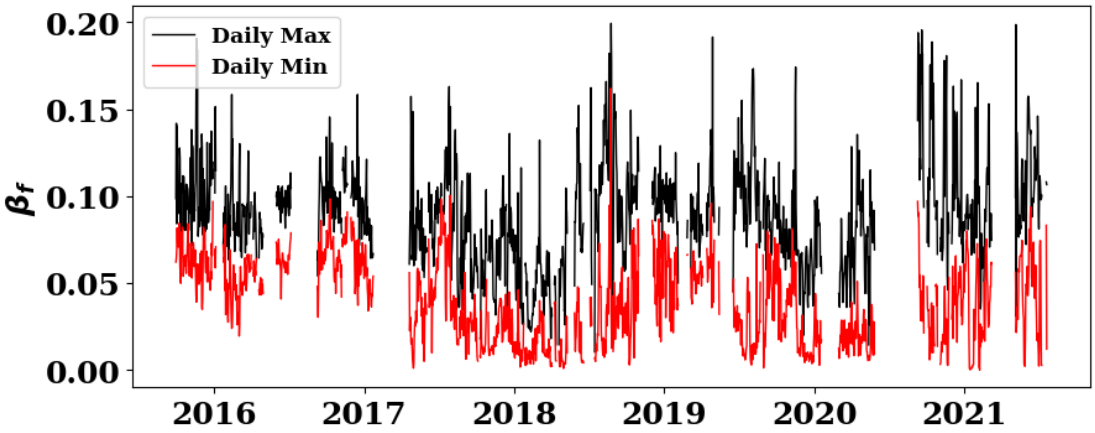

Figure 2.13. Daily maximum and minimum foreshore beach slope, calculated from mean lidar-observed swash position and beach morphology.

2.5.4 What scales of variability of beach slope are observed?

Timeseries of daily maximum and minimum beach slopes are used to assess the main scales of variability and to put the storm results in context (figure 2.13). The slopes are computed following the method of β_{obs} (Section 2.2.3). The maximum slope tends to occur at high tide, and the minimum at low tide, so the difference in the slope timeseries reflects the tidal range over the tidal cycle, as well as another indication of the consistent concave beach profile over time. Although the slope exhibits a weak seasonal cycle with a weak seasonal high in June ($\bar{\beta}_{June} = 0.07$) and low in February ($\bar{\beta}_{Feb} = 0.05$), more significant changes occur on longer time scales with shifts over weeks to months (e.g., mean slopes are low (0.03) for January to June of 2018 and high (0.08) during January to June of 2019). In addition, short-term changes occur presumably due to wave events changing the cross-shore profile as well as the intermittent presence of cusps and megacusp features. The slopes observed during the four storms fall mostly within +/- 1 standard deviation (0.03) of the long-term mean (0.06). If we use a seasonal mean beach slope in the Sto06 paramaterization for our observed four storms, the mean skill is low (-1.0).

Lacking a model for beach profile change at this location, the time series and lack of parameterization skill when using seasonal beach slope highlight the need to observe slopes as close as possible to a wave event of interest to reduce slope errors in runup calculations.

2.5.5 Discussion Synthesis

The effect of beach cusps on the FRF property and the temporal variability of beach slope at multiple scales on various runup parameterizations are complex. At the FRF, Sto06 is sufficient in predicting bulk runup throughout high energy events with a pre-storm beach profile, however, other runup parameterizations improve with the use of a time-varying beach profile. This lack of generality suggests that certain parameterizations may be better suited for other types of beaches. Regardless of whether a time-varying or pre-storm beach profile is used, once beach cusps develop, predicted runup is likely to be an underestimate due to 2D swash circulation.

Beach cusps induce a 2D circulation in the swash zone that spatially impact runup. According to Masselink et al. (1997), higher runup elevation is expected along the cusp horn (the maximum of the morphologic feature), while a longer horizontal runup excursion with a smaller maximum vertical excursion is expected along the embayment (the minimum of the morphologic feature). For both Joaquin and the Nor'Easter, the cross-shore linescans were measuring close to a horn for the majority of the timeseries in which beach cusps were present (figure 2.8). There may be various modes of swash circulation depending on the height, spacing of the cusps, and mean swash height (Masselink, Pattiaratchi, 1998). The complicating factors of swash dynamics due to the presence of beach cusps reduces the skill of the Stockdon parameterization, as shown in Section 3.3.

Given the ubiquity of these cusps, runup estimates in the greater Outer Banks region are likely to be affected. The presence of cusps also seemingly induce increased high tide magnitudes (Nor'Easter, figure 2.7), which not only influences runup estimate skills, but suggests greater implications for real world storm impacts. Additionally, the

variations in yearly beach slope and low skill when using seasonal means to predict runup through storms further indicate that accurate estimates or runup may be unattainable through storm events unless a profile close to the beginning of the storm, before large beach morphology changes occur, is measured.

2.6 Conclusion

Detailed lidar observations collected at hourly timescales within storms indicate a range of sediment redistribution patterns in both the long- and cross-shore that influence wave runup. The four storms investigated in this work had similar offshore oceanographic forcing, although differing beach responses were observed. The increasing convexity and steepening of the beach profile during Hurricane Joaquin and the Nor'Easter were not observed during Hurricanes Maria or Jose. While Jose and Maria began with similar beach profiles, their responses were distinct. During Jose there was little change to the shape or volume of the profile, while during Maria, the beach eroded seaward of the $R_{2\%}$ leading to a maximum volume loss of 10.4 m^3/m.

Despite the distinct differences between the pre-storm and the time-varying intra-storm beach morphologies, on non-cusped beaches the added information of time-variable beach slopes generally does not drastically improve estimates of empirically predicted wave runup over an assumption of the pre-storm beach profile being constant across the storm. It is of note that the definitions of slope in this work do not account for the role of curvature in the beach profile. Specifically, steeper slopes near the dune toe lead to higher runup in the observations due to highly local slope feedbacks, but these feedback mechanisms are missed by parametric runup models based on a pre-storm profile based foreshore slope. However, understanding how beach slope changes due to the intersection of mean swash at different parts of the tide on a curved beach is vital to predicting tidal variability in runup.

Our comparison of runup parameterizations using a pre-storm and time-varying beach slope was conducted over a range of periods (5.4 s to 16.7 s) and significant wave heights (0.8 m to 4.2 m) and encompassed two types of storms commonly seen on the East Coast of the United States. The result that a pre-storm beach slope may be sufficient in predicting runup throughout a storm was likely a function of the minimal changes in beach profile shape over the observed storm events. Further study is required to determine how generalizable this result is to other locations, and in particular beaches with larger grain size (e.g. gravel or cobble beaches), during larger storms, or even during other time periods in Duck, NC. These results highlight the need for continued research on understanding the morphology evolution of the beach profile near the shoreline for varied beach types during a range of storm conditions.

Our findings indicate that care must be taken when using runup parameterizations with a beach that is highly variable in the alongshore. Short-wavelength cusps (30-40 m) can degrade runup predictions even when the beach morphology is known at an hourly time scale. With the unique CLARIS dataset, we observed the presence of these beach cusps over much of the 8 km region near the FRF. Given that beach cusps are known to affect swash circulation and that the presence of mega cusps degraded the skill of the Sto06 parameterization in the original study, we anticipate that the low skill of runup parameterizations in the presence of beach cusps would likely be an issue for a large range of beach types.

The ubiquity of cusp features along sandy coastlines suggest that empirical runup parameterizations may not be sufficient over an entire field site or throughout an entire storm period, as these features are both spatially and temporally non-uniform. Additionally, the lack of skill when using seasonal beach slope means indicate the need for beach morphology measurements that more closely represent the beach profile at the beginning of storm periods. This presents a line of investigation for future work in defining how to best parameterize runup during alongshore variable beach conditions and when and how

often to collect morphological data in the interest of storm impact mitigation.

2.7 Acknowledgments

L.K., K.B., and N.C. received partial funding through the US Army Engineer Research and Development Center's (ERDC) Coastal Ocean Data Systems (CODS) R&D program. The authors would like to thank the operations team at the ERDC Field Research Facility for their continuous commitment to data collection, maintenance and processing of the data used in this paper.

Chapter 2, in full, is a reprint of the paper "Observations of beach change and runup, and the performance of empirical runup parameterizations during large storm events" published in Coastal Engineering by L.N. Kim, K.L. Brodie, N.T. Cohn, S.N. Giddings, and M.A. Merrifield in 2023. The dissertation author was the primary investigator and author of this paper.

2.A Beach slope calculation example

Figure 3.3 shows how beach slope is obtained during hour 20 of the Nor'Easter. β_{obs} and $\beta(t)$ are calculated from the beach profile measured at hour 20, whereas β_0 is calculated from the pre-storm beach profile. For β_{obs}, the position of mean swash +/- 2 standard deviations are determined by runup observations as explained in section 2.2.3 and represented by the black dots in figure 3.3. Beach slope is then determined by linearly interpolating through the beach profile between these two positions. For β_0, the iterative process of determining the predicted mean swash as described in section 2.2.3 is used on the pre-storm beach profile, with the limits over which the beach profile is linearly interpolated to determine β_0 depicted as pink dots on figure 3.3. To calculate $\beta(t)$ the same iterative process is used, but on the hourly lidar-measured profile, with the limits over which $\beta(t)$ is calculated depicted by the grey dots in figure 3.3.

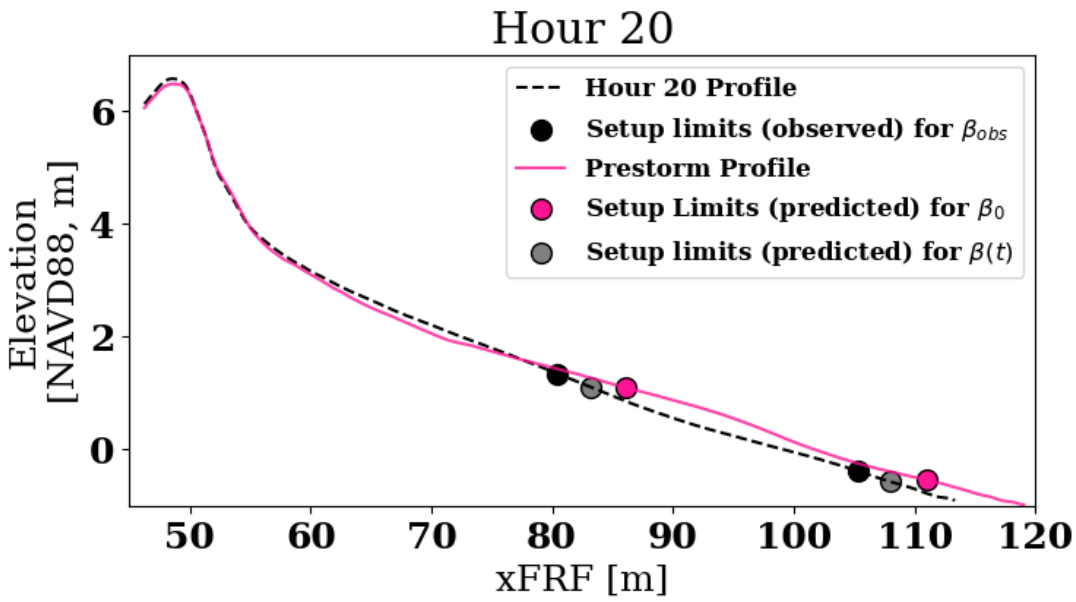

Figure 2.A.1. Beach profiles for pre-storm and hour 20 for the Nor'Easter as measured by the stationary lidar. The mean swash positions +/- 2 standard deviations are shown by the colored dots. The black dots show the observed limits over which β_{obs} is calculated from the hourly profile, the pink dots show the predicted (using the setup parameterization from Stockdon et al. 2006) limits over which β_0 is calculated from the pre-storm profile, and the gray dots show the predicted (using the setup parameterization from Stockdon et al. 2006) limits over which $\beta(t)$ is calculated from the hourly profile.

Chapter 3

Drivers of saltwater intrusion in surface sloughs

3.1 Abstract

Saltwater intrusion (SWI) into coastal freshwater systems is a growing concern in the face of climate change-driven sea level rise and hydrologic variability. SWI of freshwater in the coastal California Pajaro Valley exemplifies this concern. Pajaro Valley freshwaters are diverted for agricultural uses, but the water is unsuitable if saline. Closures at the mouth of the Pajaro River Lagoon, a bar-built estuary in the Pajaro Valley, are associated with SWI. Both closures and SWI are driven by a combination of offshore climate, coastal hydrodynamics, estuarine dynamics, inland hydrology, and infrastructure and management. Here, we describe the Pajaro Valley coastal water system using available observational data between 2012 and 2020, and identify the oceanic and inland hydrologic drivers of SWI to improve understanding of coastal freshwater management under climate change. To quantify ocean-inland connectivity, we use time series and exploratory statistical analyses of coastal total water levels (TWLs), slough stage and salinity, river discharge, and contextual knowledge from local water managers. We observe that wet season lagoon closure and SWI events follow high oceanic TWLs coupled with low stage and discharge in the inland freshwater network, revealing how both wave and inland flow conditions govern lagoon closures and coincident SWI. This study yields novel empirical findings

and a methodology for connecting coastal oceanography, estuarine coupled hydro- and morpho-dynamics, inland hydrology, and water management practices relevant to climate change adaptation in human-modified coastal water systems.

3.2 Introduction

In coastal watersheds, the movement of ocean saltwater into coastal freshwater networks creates uncertainty in freshwater supplies and thereby threatens coastal populations and industries. Coastal areas are projected to house more than one billion people by the end of the century (Hauer et al., 2020). In coastal communities, climate change and sea level rise (SLR) manifest as change in the interactions between oceanic and terrestrial systems. For example, the occurrence of coastal overtopping, driven by SLR and increased storm surge and wave runup, is predicted to increase 50-fold by the end of the 21st century globally (Almar et al., 2021). Similarly, SLR is expected to contribute to saltwater intrusion (SWI) of surface water and groundwater systems in coastal regions (Paul et al., 2019; Rice et al., 2012; Kaushal et al., 2021). SWI is defined as the landward movement of the freshwater–saltwater interface in coastal water systems typically considered fresh, and may occur in surface freshwater systems or groundwater aquifers (White, Kaplan, 2017).

Coastal threats are typically driven by increased storm surge, wave runup, frequency of storm and precipitation events (Almar et al., 2021), prolonged drought (Tully et al., 2019), and higher freshwater usage due to growing populations and water demands (Michael et al., 2017; Cosgrove, Loucks, 2015), or the confluence of two or more of these phenomena (Lucey, Gallien, 2022). Of these challenges, the issue of SWI into coastal freshwaters has received less attention than extreme events such as coastal storm-driven flooding. However, previous studies have highlighted that SLR is likely to have a profound impact on the salinity of freshwater habitats and drinking water supplies globally. In the Chesapeake Bay, USA, under a SLR scenario of 100 cm, the mean salinity of 2 tributaries were modeled

to exceed the US EPA drinking water standards, which would severly limit water intake (Rice et al., 2012). In four reservoirs of the Yangtze River Estuary, China, that provide water for 50 million people, the duration of undrinkable water was modeled to increase by up to 758% under a 2 m SLR scenario (Chen et al., 2015). Increased duration of water that exceeds chloride concentration thresholds were also modeled under SLR in conjunction with drought conditions in several branches of the Rhine River, demonstrating the vulnerability of drinking water supplies to rising seas (Brink van den et al., 2019). Ultimately, SWI is a persistent and growing concern for coastal water managers and planners (Michael et al., 2017).

SWI in coastal groundwater aquifers has been relatively well-documented using models and case studies throughout the U.S. (Jasechko et al., 2020; Sawyer et al., 2016), with one of the first studies on this phenomenon published in the mid-19th century (Houben, Post, 2017). Under climate change scenarios, SWI in aquifers is generally expected to increase due to SLR and groundwater pumping, with coastal aquifers being more vulnerable to pumping than SLR (Ferguson, Gleeson, 2012; Jasechko et al., 2020). Although the effect of SWI on groundwater supplies in regions with coastal aquifers is spatially variable, SWI has substantially affected the quality and availability of groundwater supplies in the Pajaro Valley and surrounding areas (Barlow, Reichard, 2010; Carollo, 2014; Pajaro Valley Water Management Agency, Montgomery & Associates, 2022).

For coastal surface waters, the role of saline water in general estuarine circulation has been well documented (e.g., Geyer, MacCready, 2014), and several studies have examined variability and drivers of salt wedge intrusion, often showing a relationship between the salinity intrusion length (L) and river discharge (Q) as proportional: $L \propto Q^{-n}$, where the value of n may change depending on the estuary regime (MacCready, 2004; Ralston et al., 2010; McKeon et al., 2021; Monismith et al., 2002; Hansen, Rattray, 1965). The longitudinal salt wedge intrusion length and the associated timescales of estuarine adjustment may be modulated by antecedent flow and intrusion conditions, bathymetry,

tidal phase and range, and anthropogenic modification (Monismith et al., 2002; McKeon et al., 2021; Payo-Payo et al., 2022; Ralston et al., 2010; Li et al., 2020). However, more episodic far upstream-reaching SWI events have received less attention outside the context of coastal flooding, particularly with respect to impacts on freshwater supplies.

Understanding the individual and combined contributions of offshore and inland drivers of SWI into coastal surface water and groundwater systems is important but lacking. There are multiple causes for this. First, coastal and inland hydrologic systems are frequently evaluated as separate systems, wherein the study of hydrodynamics, hydrology, and climatology is distinct with respect to data, models, and research products. Second, modeling studies may evaluate connected ocean and inland processes, but use spatial and temporal resolutions relevant only to a subset of planning and water management decisions. For example, the USGS Pajaro Valley Hydrologic Model (PVHM), which integrates conceptual water budget and numerical groundwater model components, captures relatively high resolution (monthly, 250 m) surface water and groundwater interactions in the Pajaro Valley and serves many regional water management planning activities (Hanson et al., 2014b). However, the model does not incorporate coastal wave conditions or estuary morphology, and is not designed to relate short timescale (hourly, daily, weekly) oceanic and inland hydrologic dynamics that contribute to surface SWI. Third, observational (monitoring) studies of coastal and inland freshwater interactions are valuable but face usability and generalizability challenges: reports from coastal water management communities present useful local data and model analyses, but typically pertain to specific geographic or infrastructure foci, target niche water management activities and regulatory mandates, and may not be published in peer-reviewed journals (e.g., Gomez, Sullivan Engineers, 2012; Susquehanna River Basin Commission, 2006). Lastly, data sparsity and complexity are exacerbated when water resources studies cross scales and domains, and particularly in human-modified or managed systems (Levy et al., 2016); synthesizing oceanic and terrestrial hydrologic data, groundwater and surface water data, water quantity and quality data,

and the role of infrastructure and management, is technically challenging. Thus, further data-driven and stakeholder-engaged exploration of ocean-inland hydrologic systems has the capacity to advance water science at the coastal-inland interface, as well as deliver local information to managers, planners, and policymakers (Jacobs et al., 2010; Vogel et al., 2015). Here, we provide a novel coastal-inland data harmonization, exploratory analysis, and quantify 'typologies' of coastal-inland connectivity, which provide information relevant to coastal water planning efforts under climate change.

We explore data from the Pajaro Valley, California, a groundwater-reliant coastal agricultural region located near the mouth of the Pajaro River and along Monterey Bay (Figure 3.1). This region represents an excellent opportunity to study a climate-challenged coastal freshwater system, wherein key water management questions and infrastructure investment decisions hinge on understanding ocean-inland connectivity. The Pajaro Valley faces SWI into its coastal surface water network and groundwater aquifer, both of which are managed jointly to maintain freshwater supplies (Pajaro Valley Water Management Agency, Montgomery & Associates, 2022; Hanson et al., 2014b). While SWI of the groundwater aquifer has been explored in previous research (Barlow, Reichard, 2010; Carollo, 2014; Pajaro Valley Water Management Agency, Montgomery & Associates, 2022), the surface water system has received less research focus even though it is connected to the groundwater system through local water management activities and natural interfaces.

We use the Pajaro Valley and its Harkins-Watsonville Slough (HWS) surface water system (Figure 3.1) as a setting within which to quantify, document, and describe patterns in observational data across the ocean-freshwater interface. Therein, we empirically document connectivity between climate, oceanic, inland hydrologic, and human water use and management processes, including the role of artificial (infrastructure) features. First, we provide a limited exploration of patterns in ocean and inland stage and salinity in the HWS during dry (summer) periods in order to understand baseline offshore-inland connectivity in slough stage and salinity. Next, we document time series patterns during

wet (winter) periods, and then conduct a statistical analysis to reveal thresholds in joint offshore and inland hydrologic conditions under which SWI occurs. Our primary objective is to address how oceanic drivers, such as wave height, wave period, and total water levels, interact with hydrologic drivers, including inland stage and river discharge, during open and closed lagoon mouth conditions, to generate surface water SWI events. This study represents an important step in the process of quantifying system variables and drivers of freshwater constraints in coastal systems, a hydrologic domain of research that is increasingly important with climate change, but understudied relative to other (e.g., inland freshwater) hydrologic domains. Importantly, the methods used in this case study are readily exportable to other coastal regions, and involve simple empirical approaches that can be used by practitioners to improve local to regional understanding and prediction of coastal surface water SWI.

3.3 Study Region: The Harkins-Watsonville Slough and intermittently closed Pajaro River estuary

3.3.1 Agriculture, climate and water supply

The Pajaro Valley is located on the central coast of California between Santa Cruz and Monterey counties (Figure 3.1). As of 2022, the Pajaro Valley contained about 28,500 acres of irrigated farmland that produces agricultural products valued at approximately $1 billion annually (Pajaro Valley Water Management Agency, Montgomery & Associates, 2022). This farmland houses a multitude of crops including high valued fruits such as berries, vegetable row crops, orchards, and vineyards (Hanson et al., 2014a). The region lies in a Mediterranean climate zone characterized by cool, wet winters and dry summers. Historically, the low-lying areas of the Pajaro Valley received an average 22 in/year of precipitation (Balance Hydrologics, 2014), an amount in between the average annual precipitation in the partially overlapping Santa Cruz and Monterey counties (29 and 20

in/year, respectively) (202, 2023c). The Pajaro Valley is arid and heavily irrigated, with annual average evapotranspiration rate (39.2 in/year) higher than annual precipitation (Balance Hydrologics, 2014). Unlike other arid California agricultural regions, the Pajaro Valley was never connected to state and federal water projects, the region has very limited local surface water supplies, and local freshwater streams terminate in saline ocean-connected waters. Hence, the region has historically been reliant on groundwater for domestic and irrigation uses. In the 2022 water year, groundwater accounted for 93% of the 53,756 acre feet/year of total water used in the region and 80% of this total water was used for irrigation (Pajaro Valley Water Management Agency, Montgomery & Associates, 2022).

3.3.2 Geography

The HWS surface water network within the Pajaro Valley (Figure 3.1 (a)) is the focus of our case study. The HWS is a coastal slough network that is part of a small 11,687 acre watershed that includes several upstream freshwater streams and a downstream slough segment connected to the Pajaro River lagoon. The HWS and its watershed are hydrologically separate from the Pajaro River and its tributaries within the Pajaro Valley, but both the HWS and Pajaro River watersheds terminate in the Pajaro River lagoon (Figure 3.1 (b)). The HWS overlies several water bearing geological formations: an Alluvium layer underlying the Pajaro River mainstem and upstream tributaries; Terrace Deposits and Alluvium underlying the lower-elevation segments of the HWS network; the Aromas Red Sands formation, which underlies both the Alluvium and Terrace Deposits and higher-elevation portions of the HWS watershed, and provides the majority of groundwater to the region; and the Purisima Formation, a deeper aquifer beneath the Aromas Sands that is only penetrated by a few deep wells (Hanson et al., 2014b). The Aromas Red Sands aquifer has an average thickness of 500 feet and consists of sorted brown to red sands with clay and gravel layers interspersed (Carollo, 2014). Groundwater connections

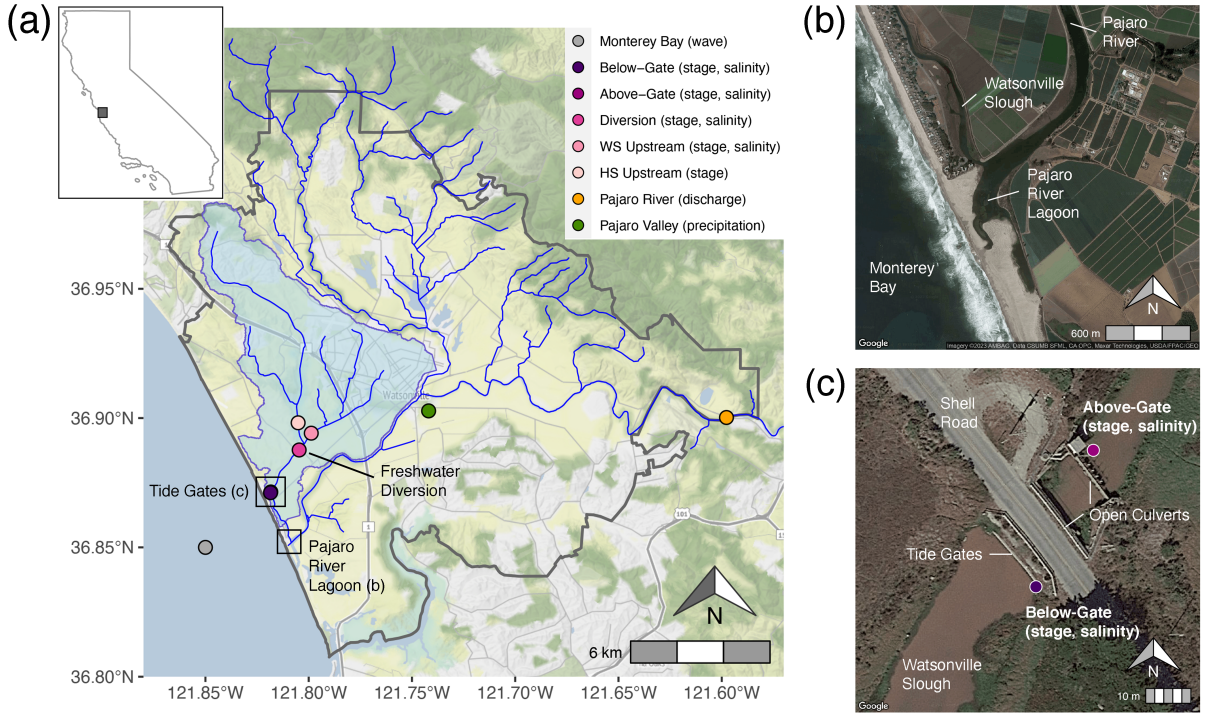

Figure 3.1. The Harkins and Watsonville Slough (HWS) system, connected river networks, and coastal zone in the Pajaro Valley, California. (a) Location of the Pajaro Valley along the California Central Coast (inset); the Pajaro Valley Water Management Agency (PV Water) statutory boundary (gray boundary); river, stream, and slough networks within the study area (blue lines); the HWS watershed (light blue region); oceanic (wave) and hydrologic (stage, salinity, discharge) measurement sites (colored points) used to assess ocean-inland connectivity in the HWS system; and the locations of the freshwater diversion site, slough tide gates, and the Pajaro River lagoon (black annotations). The HWS is hydrologically disconnected from the Pajaro River watershed, although both enter into the Pajaro River Lagoon. (b) Lagoon confluence of the Monterey Bay, Pajaro River, and Watsonville Slough, which corresponds to the annotated region in (a); the lagoon mouth is closed in this image. (c) Watsonville Slough tide gates and associated hydrologic (stage, salinity) measurement sites (colored points), which corresponds to the annotated region in (a). Note that schematics of the lagoon mouth shown in (b) and the tide gates shown in (c) are presented in Figure 3.3. Data source: Imagery sourced from Stamen and Google Maps imagery acquired through the R ggmap package (Kahle, Wickham, 2013); PV Water boundary and measurement site locations courtesy PV Water; river network is derived from National Hydrography Dataset Flowline data via the R nhdplusTools package (Blodgett, Johnson, 2022).

to the sloughs are mostly limited to areas with functioning tile drains during dry months and areas with shallow groundwaters (Balance Hydrologics, 2014). Surface waters and

the deeper primary aquifers are minimally connected within the HWS watershed (Pajaro Valley Water Management Agency, Montgomery & Associates, 2022).

3.3.3 Groundwater sustainability connections to surface waters

Overdraft of the coastal aquifer due to groundwater pumping for irrigation is a longstanding regional challenge on two connected fronts: water table decline owing to pumping, and SWI into the coastal aquifers as a result of water table decline. As of 2014, annual water table decline was estimated to be equivalent to a loss of 1,400 acre-feet (af) due to pumping and 1,900 af due to SWI (Carollo, 2014). Due to overdrafting of the groundwater aquifer and insufficient recharge from surface water supplies (i.e., from rainfall and stream bed infiltration and irrigation return flow), SWI has increased in the coastal aquifer since it was first observed in the basin in 1953 (Carollo, 2014). In order to eliminate basin overdraft and halt aquifer SWI while meeting water use needs, the local water management agency – the Pajaro Valley Water Management Agency, or "PV Water" – has executed several water management projects over the past several decades, including conservation programs, optimization of supplemental supplies, and development of new supplemental water supply facilities.

One such project is a managed aquifer recharge (MAR) (Levintal et al., 2023) program designed to infiltrate and store diverted surface water underground in a perched aquifer, and later extract and deliver that water to users in order to reduce groundwater demand (Pajaro Valley Water Management Agency, Carollo, 2018; Russo et al., 2015). The MAR project, combined with other local projects (e.g., recycled municipal water and piping of water to coastal growers located in areas of significant aquifer SWI), yielded 10,740-11,240 af of water annually, or 19.5-20.4% of average annual estimated water consumption (an average of 55,000 af/year between 2009 to 2013) (Pajaro Valley Water Management Agency, Montgomery & Associates, 2022; Carollo, 2014). Pajaro Valley groundwater

SWI and MAR, in particular, have been the subject of extensive hydrogeological research (Schmidt et al., 2012; Goebel et al., 2017, 2019; Beganskas et al., 2019; Racz et al., 2012; Schmidt et al., 2011; Hanson et al., 2014b). The MAR project began operation in 2002, and diverted approximately 10,000 af of water between the water years (Oct-Sep) 2002 and 2021, or just under 500 af/year on average. Of the total volume diverted over this 20 year period, two thirds were diverted in the first 10 years (6,750 af between 2002-2011 water years) and only a third in the subsequent 10 year period (3,200 af between 2012-2021 water years) that overlaps with our study period (Figure 3.2 (a)-(b)). On average, PV Water was able to divert only half the volume of water per year between 2012-2021 (320 af/year on average) relative to the previous decade (675 af/year on average), representing a significant decline in MAR capacity during a period when production was originally expected to stabilize or increase. The proximate cause of this decline is surface SWI.

The MAR project is supplied by surface water that is diverted from the HWS, and decline in diversion capacity is due to increasing variability in slough salinity that limits freshwater diversions for MAR. Thus, surface SWI destabilizes freshwater diversions and compromises planning of future water supplies by introducing uncertainty about the diversion and MAR storage capacity. Salinity conditions are known to align to some extent with both inland hydrology (Figure 3.2 (c)) and ocean water levels (Figure 3.2 (d)), although the specific relationships between these complex factors are not well understood or documented. This poses challenges for water management and planning activities like those of PV Water that are susceptible to change in water quantity and quality as a function of ocean-freshwater dynamics.

3.3.4 SWI and estuary dynamics

HWS surface water salinity intrusions stem from the slough network being connected to Monterey Bay via the Pajaro Lagoon (Figure 3.1 (b), Figure 3.3 (a) and (c)), wherein closure of the lagoon typically precedes surface SWI. Closure is a natural process that

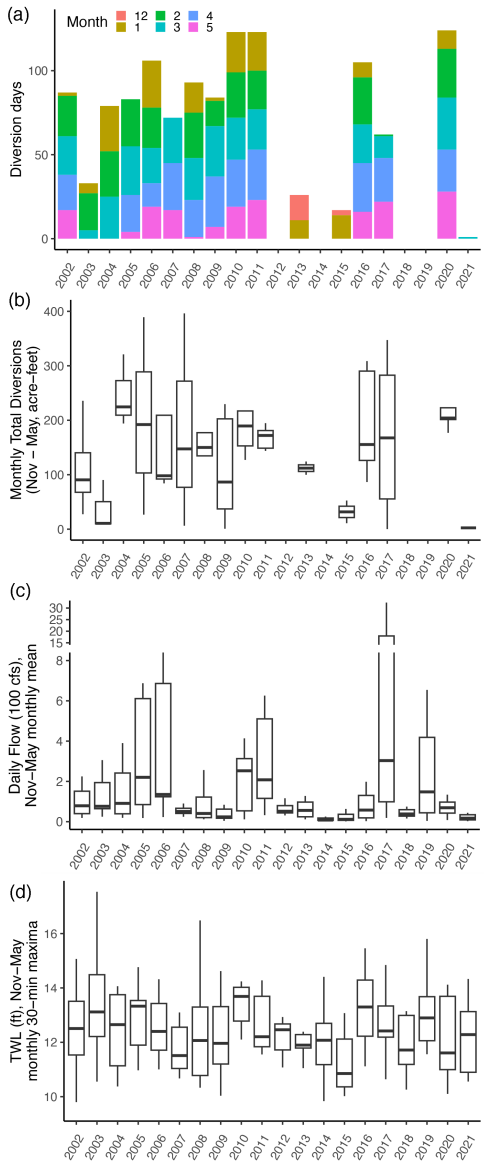

Figure 3.2. Distributions in slough freshwater diversions, inland freshwater discharge, and ocean water levels during freshwater diversion months of November-May, water years 2002-2021. (a) Monthly occurrence (count of days) of freshwater diversion from the HWS within each water year (Oct-Sep). (b) Water year distributions of Nov-May total monthly freshwater volumes (af) diverted from the HWS; years with no diversions show no values. (c) Water year distributions of Nov-May within-month means of daily mean discharge (100 cfs) in the Pajaro River, upstream of the Pajaro River lagoon. (d) Water year distributions of Nov-May within-month maxima of 30-minute total water levels (TWL, ft) in the Monterey Bay. Distributions in (b)-(d) show the interquartile range (IQR) boxes and ± 1.5*IQR whiskers, with outliers omitted from the visualization only. Data sources: see Methods.

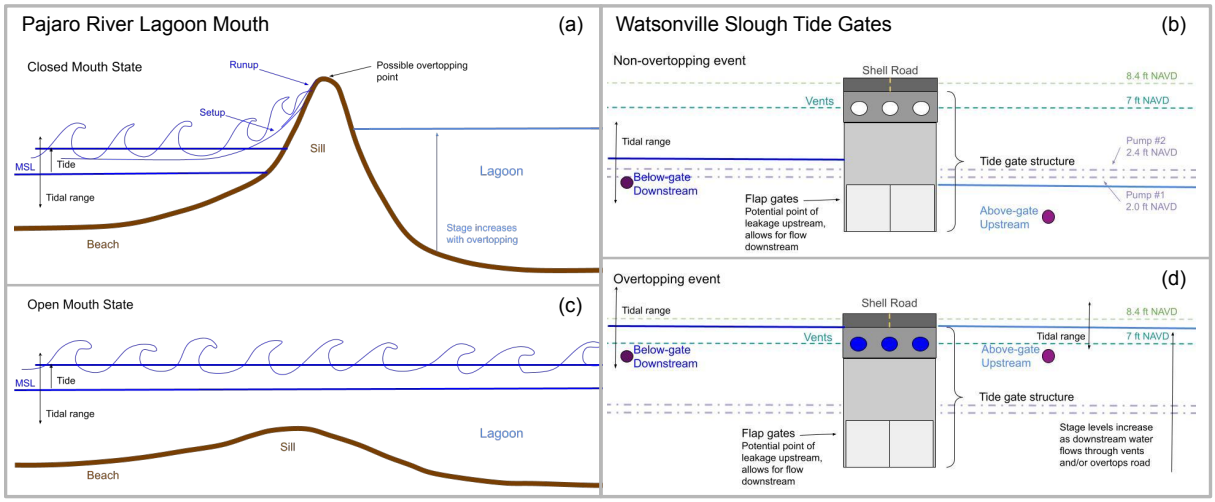

Figure 3.3. Schematics of the Pajaro River lagoon mouth and Watsonville Slough tide gates. (a) Schematic of closed versus (c) open lagoon mouth states, adapted from Nielsen (2009). For the closed mouth state, the buildup of the sill halts most oceanic connectivity, but if TWL exceeds the sill height, wave overtopping may occur and raise the stage within the lagoon. Mean sea level (MSL) refers to the long term average sea level, which the tidal range may oscillate around. For the open mouth state, the lower sill height allows for a dynamic connection between the coastal ocean and the lagoon. (b) Schematic of non-overtopping versus (d) overtopping event at the tide gate structure. For the non-overtopping event (b), water may move downstream through the tide gates under sufficient pressure, and minimal upstream leakage may occur. For the overtopping event (d), water may move upstream (reverse flow) through the vents or via overtopping of Shell Road and increase stage levels above-gate; during these events, stronger tidal variations in stage are observed above-gate due to the connectivity across the tide gate structure. When water is moving in a downstream direction due to high inland freshwater discharge, water may move through the flap gates, through the vents, and over the road depending on stage levels.

occurs when sediment deposition from coastal processes overwhelms the ability of tidal and riverine currents to maintain an open connection between the river and ocean. Thus, estuarine dynamics are central to understanding surface water SWI in the Pajaro Valley. The Pajaro Lagoon is a low-inflow, bar-built, intermittently closed estuary. These estuaries may be vertically mixed or stratified depending on winds, solar heating/convective cooling, evaporation, and tidal phase (Largier, Taljaard, 1991; Ranasinghe, Pattiaratchi, 2003; Harvey et al., 2023; Largier, 2023). They exhibit morphodynamically active mouths wherein sandbars are built by ocean waves and strong and/or persistent inflowing currents

(Largier et al., 1992; Clark, O'Connor, 2019), and are eroded by river discharge and strong and/or persistent outflows (Behrens et al., 2013; Orescanin et al., 2021).

During open lagoon conditions, the estuary is dynamically connected to the ocean (Figure 3.3 (c)), and typically has lower flushing times or a smaller ratio of the volume of freshwater within the estuary to the total rate of freshwater inflow (Dawson et al., 2023). However, sandbar buildup can close the river mouth and halt most oceanic connectivity, though there may be some leakage through or over the sill. During closures, ocean water from overtopping waves (Harvey, 2019; Williams, Stacey, 2015) can be trapped in the lagoon (Balance Hydrologics, 2014). This causes lagoon water levels to increase, and saline water from the lagoon can move upstream into freshwater bodies via multiple mechanisms, including gravitational adjustment and gravity currents initiated by wind-driven internal seiches (Behrens et al., 2016; Okely, Imberger, 2007). During open or partially-open estuary conditions, saltwater may still be retained in the estuary and may not be immediately flushed out (Largier, Taljaard, 1991; Williams, Stacey, 2015), which may exacerbate salinity conditions upstream in the slough system. Estuaries like the Pajaro River estuary that receive less freshwater input than a classical estuary and have mouths that close intermittently are common worldwide in Mediterranean climates and wave-dominated coasts, and are found across California (Duong et al., 2016; Harvey, 2019; Largier, 2010; McSweeney et al., 2017; Largier, 2023).

Several studies have analyzed the multiple factors that drive estuary closures and openings for bar-built, intermittently closed estuaries along the California coast. Using 60 years of data at the Russian River (90 km north of San Francisco Bay), Behrens et al. (2013), identified tidal, weather related, seasonal, and interannual cycles of mouth closure. At the tidal timescale, hydraulic parameters (river discharge, inlet aspect ratio, and tidal prism) appeared more important to mouth closure than wave conditions, and seasonal scale closures appeared connected to interactions between wave height and river flow. This is likely due to the fact that sufficient wave energy for closure is present for the majority

of the year, and thus other processes tend to control closures. At the longer, interannual timescale, closure was hypothesized to be related to the Pacific Decadal Oscillation (PDO) and Northern Oscillation Index (NOI) via connections with river flow patterns. Mouth closures may also be heavily wave-dominated (Hanes et al., 2011; Orescanin, Scooler, 2018; Bertin et al., 2019; Harvey et al., 2023). Lagoon breaches, on the other hand, tend to occur under high river discharge conditions following heavy precipitation and may be modulated by longshore wave forcing, as observed in the nearby Carmel River State Beach (Orescanin, Scooler, 2018; Orescanin et al., 2021).

The Pajaro River estuary experiences closures and openings throughout the year. Along with other central California sites, closure events at the Pajaro River estuary can occur in most months of the year, but tend to be most common in the summer or fall (Clark, O'Connor, 2019). This is because streamflow tends to be low from May to October, while long-period swell waves are often present in late spring and early fall. While powerful swell waves can initiate closure events and rapidly build up a sill in front of the estuary, coincidence with low streamflow is a requirement for closure events to last for more than several days. This is because the closed estuary can rapidly fill and overtop the sill (reopening the inlet) during periods of high flow. Nevertheless, the reliance of closure events on coincident river and coastal conditions leads to sharp variations in the closure pattern from year-to-year. For example, in drought years such as 2014, 2015, and 2021, the estuary was closed for more than 6 months of the year (typically from late spring through late fall). In wet years, the estuary sometimes remains open throughout the year. In most years, brief closure events lasting only a few days occur in winter or spring (coincident with strong wave events), and the longest closure events occur beginning in summer or fall (when strong wave events coincide with low streamflow).

Thus, Pajaro Lagoon closures followed by natural or mechanical openings, have occurred in the November-May time period during which PV Water can divert freshwater from the HWS. During closures, the estuary may open naturally or be manually dredged by

the County of Santa Cruz (CSC) during a particularly lengthy closure for the purposes of flood control and public safety (i.e., to cause a water level decline in the lagoon and sloughs adjacent to residential and agricultural land). However, manual breaching is only carried out when the closure poses significant and immediate flood risk to people or property, not for water management purposes.

The same factors that have been found to drive estuary closure and opening dynamics (climate patterns, weather, tides, hydraulics and hydrology) also necessarily govern coastal SWI in estuary-connected freshwater environments. In the Pajaro Valley, the movement of saline water into the HWS can be described as a function of multiple observable drivers – the same drivers that govern estuary closures: inland and offshore climate (precipitation, storm events), coastal hydrodynamics (tides, wave runup and overtopping), estuarine dynamics (inlet mouth morphology), inland hydrology (freshwater runoff), and infrastructure and management (tide gates, freshwater diversion, lagoon dredging). Yet, the drivers of salinity pulses into surface freshwater supply systems – in the Pajaro Valley and elsewhere – are not well understood in the context of coastal freshwater management, even if the joint roles of river discharge and coastal hydrodynamics are somewhat more well-defined within the coastal storm surge and flood frequency estimation literature (Lucey, Gallien, 2022; Ganguli, Merz, 2019; Vitousek et al., 2017).

3.4 Methods

3.4.1 Data

We utilized a variety of datasets to obtain offshore, estuarine, inland hydrologic, and climatologic conditions, the consistency and durations of which vary (Table 3.1). Details are provided with respect to each dataset below.

Table 3.1. Data types, resolutions, and durations available for the Pajaro Valley and Monterey Bay.

Description	Data type	Temporal resolution	Temporal duration	Source
Deep water wave buoy	significant wave height, peak period	hourly	1987-present	NDBC, NOAA stations 46042 & 46114
Offshore tide gauge	water level	6 min	1996-present	NOAA station 9413450
River mouth/lagoon conditions	manual breach dates	intermittent	2008-2020	County of Santa Cruz (CSC)
Watsonville/Harkins Slough Monitoring	stage, specific conductivity	30 min (with gaps)	2011-2020	PV Water
Pajaro River Monitoring	stage	15 min	1911-present	USGS
Harkins freshwater diversion	volume of water diverted	daily	2002-2021	PV Water
Weather station	precipitation	hourly	1995-present	CIMIS station 129

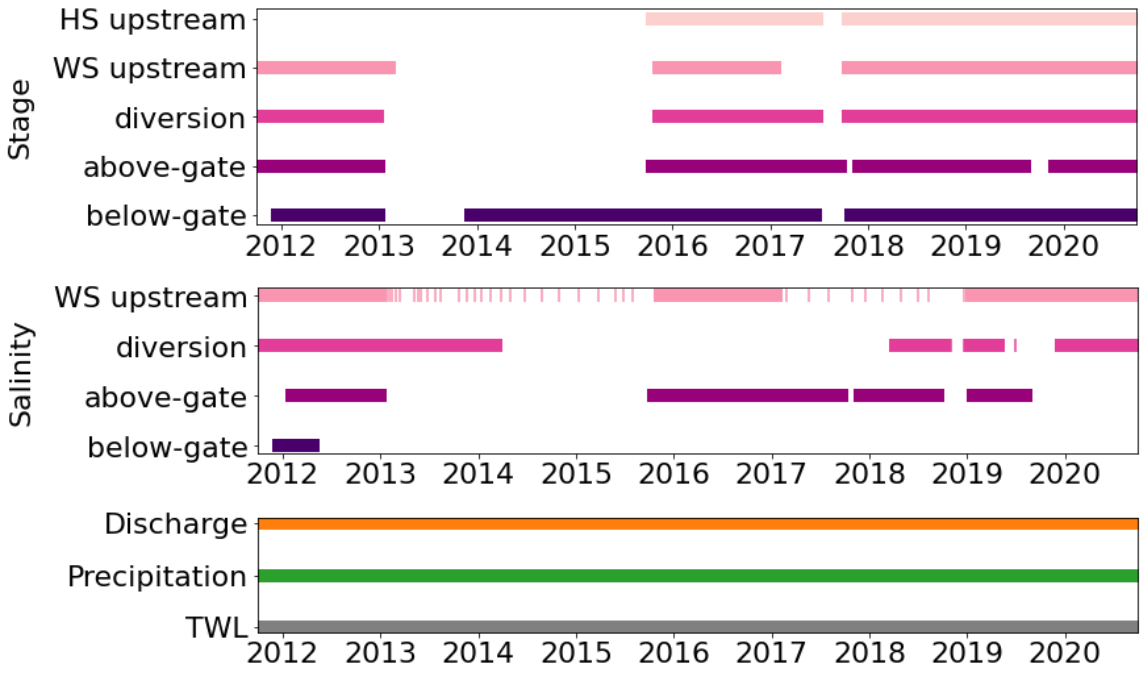

Figure 3.4. Data availability for stage, salinity, discharge, precipitation, and total water level (TWL) between October 2011 and December 2020. Colored bars indicate that data are available for the corresponding variable and sensor. All data were aggregated to a 30 min resolution, except for precipitation, which is hourly, and discharge, which is measured every 15 minutes. Note that estuary/slough sensors are colored from downstream (darkest) to upstream (lightest) as indicated on Figure 3.1.

Offshore oceanic and estuary conditions

Offshore water level (OWL) and total water level (TWL)

To represent offshore tide conditions in the Monterey Bay, we acquired publicly available hourly offshore water level (OWL, converted to ft NAVD) measurements from the NOAA tide gauge closest to the study region (station 9413450) in Monterey Bay, CA between the dates of 10/1/2011 and 9/30/2020 (202, 2023a). To represent wave conditions at the Pajaro Valley coastline, we used data from the National Data Buoy Center (NDBC) from NOAA, which outputs hourly deep water significant wave height and wave period; we acquired data between the dates of 10/1/2011 and 9/30/2020. We used the Monterey Buoy Station 46042 (NOAA, 2023a) and the West Monterey Buoy Station 46114 (NOAA, 2023b)

for dates 1/1/2012-1/9/2012 when Station 46042 was unavailable. We used the significant wave height (Hs, m) and peak wave period (Tp, seconds), which provide measures of coastal ocean wave magnitude and frequency that are relevant to estuary closure and surface SWI along the Pajaro coastline.

The estimated hourly total water level (TWL, converted to ft NAVD) at the Pajaro Valley shoreline is the sum of the Monterey Bay OWL and Pajaro Valley coastline-specific wave runup, and was calculated for the period between 10/1/2011 and 9/30/2020. TWL provides a measure of the total height of ocean water incident upon the Pajaro Valley coastline, and specifically upon sandbars of the Pajaro River lagoon mouth. The actual TWL was not observed during this period of time and is likely lower than our estimates due to limiting factors like the beach width and lagoon mouth sill height. However, our approach to TWL estimation is intended to capture an upper-bound combination of wave energy and water levels at the shoreline during the study period.

The OWL component is the directly observed offshore water levels from the NOAA tide gauge that includes the combination of astronomical tides, storm surge, sea level anomalies, and possible wave setdown (Pugh, 1987; Chelton, Davis, 1982). Runup is defined as the vertical position of discrete (ocean) water level maxima due to the uprush of broken waves and wave setup at the shoreline. We chose to estimate TWL with the $R_{2\%}$ exceedance value because of its prominence in coastal flooding and storm impact literature (Almar et al., 2021; Sallenger, 2000; Stockdon et al., 2007b; Ruggiero et al., 2001). Here, we estimated an hourly 2% exceedance runup value with the widely used Stockdon parameterization (Stockdon et al., 2006). Inputs to this parameterization include deep water wave height and period, and beach slope for the Pajaro Valley shoreline. Deep water wave height is taken from the NDBC Buoy, and deep water wavelength is calculated from the buoy-measured wave period following the linear dispersion relationship, $L = gT^2/(2\pi)$ (Stockdon et al., 2006). We calculated beach slopes from beach elevation data collected at Pajaro dunes (lat, lon) via GPS walking surveys using a Spectra GPS antenna and

a Post-Processing Kinematic correction technique on 2/18/22, 3/11/22, and 4/15/22. GPS walking surveys include a perimeter outlining the beach low water line, the mouth boundary, and into the lagoon region, coupled with 20 m transect spacing filling the perimeter. Any high-gradient areas (scarps, dunes) included higher resolution transects. We linearly interpolated GPS point cloud data onto a 1x1 m grid, creating a surface of the entire beach, and extracted cross-shore transects (perpendicular to the mean longshore beach direction) near the lagoon mouth to establish an estimated measure of beach slope. Because beach slopes change with time and location (i.e., along the coast), and due to the lack of continuous beach morphology observations for our study period, we used the average of multiple beach slope measurements. For consistency with inland hydrologic data, we linearly interpolated hourly oceanic water level variables (OWL and TWL) to a 30 minute temporal resolution.

Observations of the date of manual breaching events and several closure observations were provided by the County of Santa Cruz (CSC). Manual (visual) observations of lagoon closures and openings, including openings through natural and manual breaching, were conducted by CSC on an intermittent daily basis. CSC utilized a binary open/closed classification to describe the lagoon mouth conditions between December 1, 2008 and January 31, 2020. However, this dataset did not identify all closure events and durations of lagoon closures, so we manually identified closure periods as periods when the stage at the below-gate site on the Watsonville Slough (see section 3.1.2) had diminished tidal variation and consistently increasing stage values. Lagoon mouth openings were identified by events in which below-gate stage quickly decreased and tidal variability was re-introduced. We cross-referenced these opening events with the CSC-provided breach records, validating the accuracy of our manual identification; for every available manual or natural opening recorded in the CSC records, our method correctly catalogued the event.

Inland hydrologic conditions

Infrastructure complicates hydrology in the HWS system, and specifically the presence of a tide gate in the Watsonville Slough portion of the lower HWS system (Figure 3.3 (b) and (d)), located approximately 2.5 km upstream of the lagoon (Figure 3.1 (a) and (c)). The tide gate structure consists of the following features: vertical flap gates that open with downstream slough discharge, but close if downstream flow is insufficient; vents above the flap gates that allow flow over the gates in either direction under high water conditions (i.e., during lagoon closure-induced high water levels); and two pumps located just above the gates that pump pooled water from above the gates to a location just below the gates in order to maintain sufficiently low water levels above the gates for irrigation drainage from adjacent agricultural plots. The two pumps are automatically triggered when the above-gate stage reaches 2 and 2.4 ft NAVD (North American Vertical Datum of 1988), respectively; during high stage events ($>$ 7 ft NAVD), i.e., during tide gate overtopping, the pumps are rendered useless and are manually shut off. The tide gates prevent significant SWI into the HWS so long as ocean water levels remain lower than the top of the tide gates (below the open vents located at 7 ft NAVD), however some upstream leakage may occur. We used hydrologic monitoring data provided directly by PV Water at five locations within the HWS (Figure 3.1): immediately downstream of the tide gates on Watsonville Slough ("below-gate" site), immediately upstream of the tide gates on Watsonville Slough ("above-gate" site), near the MAR diversion location on Watsonville Slough ("diversion" site), 600 m upstream of the diversion site on the Watsonville Slough ("WS upstream"), and 950 m upstream of the diversion site on the Harkins Slough ("HS upstream" site). The monitoring station we refer to as the "diversion site" is located 300 m downstream of the true point of MAR diversion at the confluence of the Harkins and Watsonville Sloughs. We use the "diversion site" location to reflect diversion conditions (as done previously, see Balance Hydrologics, 2014) due to its more

consistent data, relative to monitoring at the true diversion point, and its location at a point that conveniently reflects the combined flows of Harkins and Watsonville Slough under typical downstream flow conditions.

At these monitoring sites, PV Water provided 30 minute resolution measurements of inland surface water stage and salinity from water logger sensors (In-Situ Aqua Troll 200 or In-Situ Rugged Troll 100, depending on location). The water loggers have a potential level of error of $\pm$ 0.05 ft. These data were provided for the period between September 2011 and September 2020. However, the logger data are intermittent; missing stage data range from 14% (below-gate) - 47% (HS upstream), while missing salinity data range from 49% (above-gate) - 95% (below-gate). Data coverage stems from the nature of PV Water monitoring and management needs; in situ measurements are collected by Balance Hydrologics, a hydrologic consulting firm contracted by PV Water, for regular monitoring needs as well as infrastructure-specific objectives and time periods. Increasingly consistent logger data is available in more recent years (after 2018). PV Water also provided approximately monthly "grab sample" measurements of salinity, which were collected as a part of routine agency water quality monitoring.

Measurements of stage are recorded in ft NAVD, and measurements of salinity in units of microsiemens per centimeter at 25 $^{\circ}C$ (µS/cm). Salinity was converted to practical salinity units (psu) for ease of comparison with oceanic conditions. Calculations of volumetric discharge (cubic feet per second- cfs) were calculated using rating curves at some, but not all, PV Water stream monitoring locations in the HWS; thus we use stage in our analyses. Pajaro River stage and discharge were measured at 15 minute intervals upstream of the Pajaro lagoon at station 11159000 (Pajaro River at Chittenden) by the USGS (USGS, 2023); we used discharge in our analysis due to the use of that metric in previous assessments of lagoon closure conditions (Balance Hydrologics, 2014; Orescanin, Scooler, 2018). We acquired daily precipitation data from the California Irrigation Management Information System (CIMIS) station 129 located in the Pajaro

Valley west of Watsonville (California Department of Water Resources, 2023).

Much of the data used in our analysis has been used in previous studies commissioned by PV Water for its own planning and management purposes (e.g., see "Watsonville Slough System Hydrologic Monitoring Water Year" reports) (Pajaro Valley Water Management Agency, 2023). For all PV Water data, we performed quality assurance and quality control (QA/QC), which included visual inspection of time series, removal of outliers and data indicating sensor failure (e.g., exact zeroes, static measurements, irregular/artificial patterns), and checking that data distributions conformed with expectations.

Salinity data required significant QA/QC. Salinity data were collected only at HWS sites with demonstrated historical salinity intrusion relevant to PV Water management activities. There were four HWS sites with usable salinity measurements: the below-gate, above-gate, diversion, and WS upstream sites. Salinity at the below-gate site was only available in 2012. We would expect below-gate salinity to be related to lagoon salinity at some depth; lagoon salinity is unmeasured but may exhibit vertical stratification as similar systems do (Harvey et al., 2023; Williams, Stacey, 2015). For these sites, we identified time periods within which salinity records were not available or biased. We evaluated bias by comparing daily-aggregated logger salinity to monthly grab sample measurements taken by PV Water during the study period. For three of the sites (above-gate, diversion, and WS upstream sites), we confirmed consistency between logger and grab sample salinity records at the daily time scale over the full period of study. For the diversion site between March 2014 and March 2018, records were either missing or logger records were biased upwards according to comparisons with grab sample data; the logger and grab sample records were consistent for other dates within the study period at this site. The diversion site bias was likely caused by brackish water backflow in the stilling well. We replaced the biased diversion site salinity with available logger measurements from the site of true MAR diversions – the Harkins Slough Pumphouse, which is located approximately 300m upstream of the diversion site (Supplementary Figure S1). We confirmed the Pumphouse

site salinity to be statistically consistent (according to interquartile range overlap) with diversion site salinity during non-biased time periods, and thus a suitable substitute. PV Water typically uses stage and salinity measurements at the Pumphouse site to monitor freshwater availability and suitability for MAR.

We use a diversion site salinity threshold of 0.5 psu to represent the upper limit of salinity in water suitable for MAR. This salinity threshold is an approximation because salinity ranges within which freshwater diversion can occur are in practice variable (Supplementary Figure S1) and a function of salinity in the slough and MAR basin; slough salinity must be less than that of the water in the recharge basin at the time of diversion as to not degrade groundwater quality. Furthermore, vertical mixing of stratified saline water as well as mixing of converging slough waters at the confluence of Harkins and Watsonville Sloughs can occur as a result of diversion pumping itself, altering diverted water (sample) salinity relative to logger measurements (Supplementary Figure S1). Given this complexity, we use a simple threshold of 0.5 psu at the diversion site to represent the salinity threshold for freshwater diversion. This is consistent with the greater of available logger and grab sample salinity mean values on diversion days (0.5 and 0.4 psu, respectively) and is the same threshold used previously in modeling studies of slough salinity conditions (Environmental Science Associates, 2020).

In coordination with PV Water and the CSC, which are responsible for above-gate and below-gate components of HWS management, respectively, we outlined a set of tide gate "rules" governing flap gate behavior with respect to HWS stage (Supplementary Table S1). These rules document ocean-slough connectivity conditions that are governed by the tide gates: vent overtopping occurs when above-gate or below-gate stage exceeds 7 ft NAVD (i.e., during lagoon closures); downstream (open tide gate) flow occurs when the above-gate stage is greater than the below-gate stage (i.e., during high freshwater discharge periods); and upstream leakage (closed tide gate) occurs when the above-gate stage is lower than the below-gate stage (i.e., during low freshwater discharge periods).

With regard to the height at which vent overtopping can occur, we use 7 ft NAVD as an approximate height to represent vent overtopping conditions based on a combination of previous measurement and modeling efforts (Balance Hydrologics, 2014), and observed maximum stage at the tide gates, which ranges between 7 ft NAVD-8 ft NAVD during closure and overtopping events documented by PV Water. Although precise vent height and vent overtopping measurements were made in the past, and specifically with respect to the 2012 event, there remains uncertainty in the precise vent overtopping height in subsequent years due to one or more of the following: head differences above and below the tide gate, with associated pressure head that opens or closes flap gates, which can create head differences across the gate even during lagoon closure events; calibration error in the pressure transducer used to generate stage measurements; or error in the surveyed elevation at the tide gate.

3.4.2 Time series analysis

Using the synthesized data, we first inspected connectivity between ocean and inland hydrologic signals graphically using aligned time series visualizations. To understand different types of connectivity, we focused on two primary conditions: wet/extreme and dry/baseline conditions. Our analysis focused on wet/extreme conditions that pose the greatest challenge to freshwater availability, but we also provide a limited analysis of dry/baseline conditions. For both, we selected representative time periods and visualized oceanic and hydrologic conditions along a transect from ocean waters in the Monterey Bay, to inland freshwater levels and salinity in the HWS system, to Pajaro River discharge and Pajaro Valley precipitation.

For the wet/extreme case, we isolated periods of time in wet/winter diversion months (November-May) during which below- and/or above-gate stage levels approached and/or exceeded levels at which tide gate vent overtopping occurs, representative of conditions under which there may be flow of saline lagoon water upstream into the freshwater system,

i.e., surface water SWI. Using visualizations alongside contextual knowledge from local water managers, we provide qualitative descriptions of the observed dynamics within and across events. For the dry/baseline conditions, we identified periods of time in dry/summer non-diversion months (June-August) during which there was no or minimal precipitation and associated freshwater discharge in the HWS system, and when gates were closed (i.e., below-gate water levels exceeded above-gate levels). To establish an understanding of baseline ocean-slough connectivity conditions (relative to those under wet/extreme conditions), we performed a spectral and coherence analysis of summer month data to understand features of ocean-inland connectivity in the HWS (Supplementary Text S1, Supplementary Figure S2).

3.4.3 SWI event Typology

With respect to the wet/extreme conditions, we sought to investigate joint offshore and inland hydrologic conditions that correspond to SWI events in the HWS system. Although PV Water previously qualitatively identified the drivers of salinity intrusion for a single event, we used multiple events over the period between 2012-2020 to quantify these drivers generally, and establish criteria for when we might anticipate salinity intrusion in the Pajaro Valley's HWS system. We subset Hs, Tp, TWL, upstream stage, and Pajaro River discharge time series data into three categories representing the following events: 1) tide gate overtopping events with associated SWI; 2) tide gate overtopping events without associated SWI; and 3) events during which stage levels approached the height of the tide gates, but wherein no overtopping occurred. We categorized these events using the following ordered criteria: first, stage relative to the tide gate vent, and second, salinity levels. Specifically, we defined tide gate overtopping events with associated SWI using observations from the 12 hours before and 1 hour after the below-gate stage exceeded the tide gate vent height (7 ft NAVD), and with a concurrent or subsequent (within 24 hours) increase in salinity at the above-gate and/or diversion site (depending on data

availability). Similarly, we defined tide gate overtopping events without associated SWI events using observations from the 12 hours prior to and 1 hour following the onset of stage at the below-gate site exceeding the tide gate vent height with a concurrent decrease or no change in salinity at the above-gate and/or diversion site. Finally, we defined events during which stage levels approached the height of the tide gates, but no overtopping occurred, using observations from the 12 hours prior to and 1 hour following the onset of stage at the below-gate site reaching 6 ft NAVD but not exceeding the vent height (7 ft NAVD); salinity was not considered during these non-overtopping events. We based our selection of 12 hours before and 1 hour following event onset to define events because it encompasses a full tidal cycle leading up to the event. We performed a supplementary analyses in which we varied the number of hours included prior to and immediately following the overtopping onset to understand the sensitivity of our results to variation in the selected time frame.

We then calculated the percentiles of the values of each of the variables (Hs, Tp, TWL, upstream stage, and discharge) using all data from November to May (months during which freshwater diversion can occur) across all available years, and then recorded the percentiles of those variables for data in the 13 hour windows of the 3 event types. For upstream stage percentiles, which were based on a time series with missing data, the number of stage observations ranged from 67% of the total possible number of observations (March, 8,916 observations) to 76% of the total possible observations (December, 10,183 observations); these constitute sufficiently large samples sizes that are adequately balanced across months. For an event to be included in the percentile analysis, data available for the duration of the event needed to include the offshore data: Hs, Tp, TWL; stage at the below-gate site for establishing whether the vent was overtopped; salinity at the above-gate or diversion site for determining whether the event included SWI; and Pajaro River discharge. We also evaluated WS upstream stage data for 2 of the 4 events in which it was available. We visualized the distribution of the event percentiles using box and whisker plots, representing the interquartile range (IQR, box) and $\pm 1.5 * IQR$ (whisker) of those

event percentile values; outliers of the $\pm 1.5 * IQR$ are shown as scatter points. The suitable data used to represent overtopping events with SWI (4 events with 50 observations of Hs and Tp, 108 observations of TWL, 54 observations of upstream stage, and 216 observations of Pajaro River discharge) and without SWI (32 events with 417 observations of Hs and Tp, 837 observations of TWL, 702 observations of upstream stage, and 1620 observations of Pajaro River discharge) were limited relative to the high but non-overtopping events (96 events, with 830 observations of Hs and Tp, 1809 observations of TWL, 1161 observations of upstream stage, and 3461 observations of Pajaro River discharge). We performed a limited sensitivity analysis by iteratively calculating leave-one-out estimates of percentiles within event categories and variables, and assessing variability in resulting distributions for the overtopping with SWI case (Supplementary Figure S7).

3.5 Results and Discussion

3.5.1 Dry/Baseline Connectivity

We evaluated baseline conditions of the slough during summer periods to compare to winter/wet conditions in which we observe large salinity intrusion events. During the summer/dry season, Pajaro Valley water managers observe minimal connection between downstream and upstream stage due to low upstream stage conditions and presence of tide gates designed to block reverse flow of higher stage ocean water into the slough. Furthermore, leakage that does occur is generally understood to not extend further upstream than the diversion site due to channel gradients and sediment fans in the stream channel downstream of the diversion site. In several summer periods, we observed salinity at the above-gate site slowly increase, despite gate closure. Consistent with local understanding, management-relevant salinity increases were not observed further upstream. For example, between June and August of 2016, we observed above-gate salinity gradually increase from 2.4 to 7.1 psu (Figure 3.5 (d)). During this time, there was minimal or no

precipitation (Figure 3.5 (e)), and stage at the diversion and both upstream sites gradually decreased. Stage decreases were steady in the case of the diversion and HS upstream sites, and the WS upstream site stage shows minor fluctuations potentially associated with minor (< 1mm/hour) precipitation, diurnal baseflow variation, and/or irrigation drainage. Based on this alone, it may be possible to conclude that gradual salinity increases are associated with decreased freshwater discharge, evaporation, and resulting concentration of salts in the above-gate water pool, wherein salts are contributed by agricultural drainage (Thorslund et al., 2021). Leakage of saline water across the tide gate may also play a role in this increasing salinity, however defining the contributions to salinity from each of these processes is complex and outside the scope of this work. Because we observed regular small amplitude stage fluctuations at both the below- and above-gate sites potentially indicative of connectivity (Figure 3.5 (c)), we investigated the drivers of these fluctuations further using a spectral and coherence analysis (Supplementary Text S1, Supplementary Figure S2). We found that multiple drivers of variability in stage may be present, including minor leakage and/or atmospheric pressure variations, but that additional observations would be needed to properly attribute driver contributions to those fluctuations.

3.5.2 Wet/Extreme Connectivity

During wet/extreme conditions, the timing and magnitude of interactions between coastal water levels (TWL), climate (precipitation), and hydrology (stage, river discharge) govern the presence or absence of SWI, and its intensity. From a collection of 36 events wherein slough stage at the tide gates exceeds the overtopping height of the tide gate vents according to stages measured at the below-gate site, we demonstrate time series relationships for several key illustrative examples.

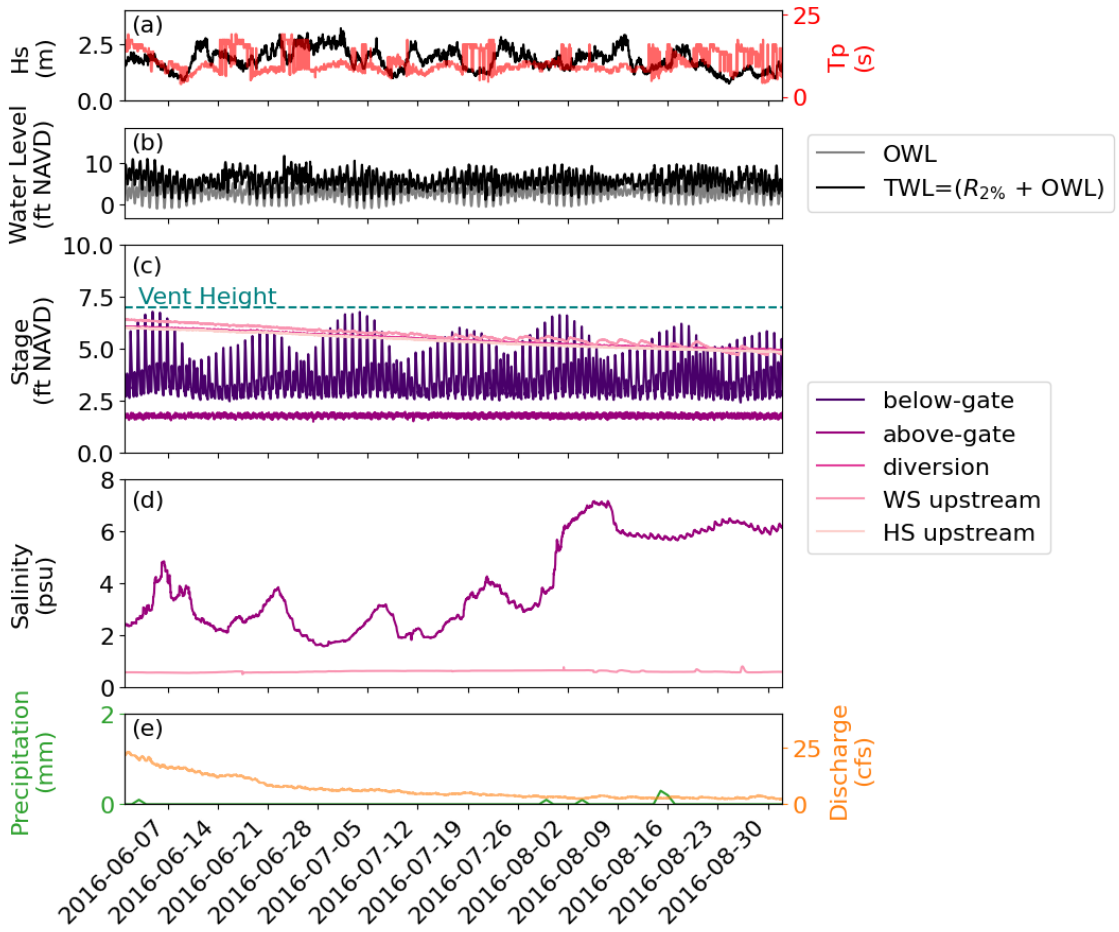

Figure 3.5. Coastal to inland stage and salinity connectivity under dry/baseline conditions over 2 months (June 1, 2016–August 31 2016). (a) Significant wave height (Hs) and peak period (Tp); (b) offshore water level (OWL) and total water level (TWL); (c) stage at the below-gate, above-gate, diversion, and upstream stations, with the elevation of the tide gate vent (dashed turquoise line). (d) salinity at the above-gate and WS upstream stations; (e) precipitation and Pajaro River discharge.

January 2012: SWI following vent overtopping with a closed lagoon, high TWL, and subsequent manual breach coincident with storm-driven freshwater flow

During wet periods, the tide gates open to facilitate HWS discharge during rainfall-runoff events, or close to block reverse flow of higher stage ocean water into the slough (similar to dry/baseline conditions). However, the tide gates do not prevent SWI during

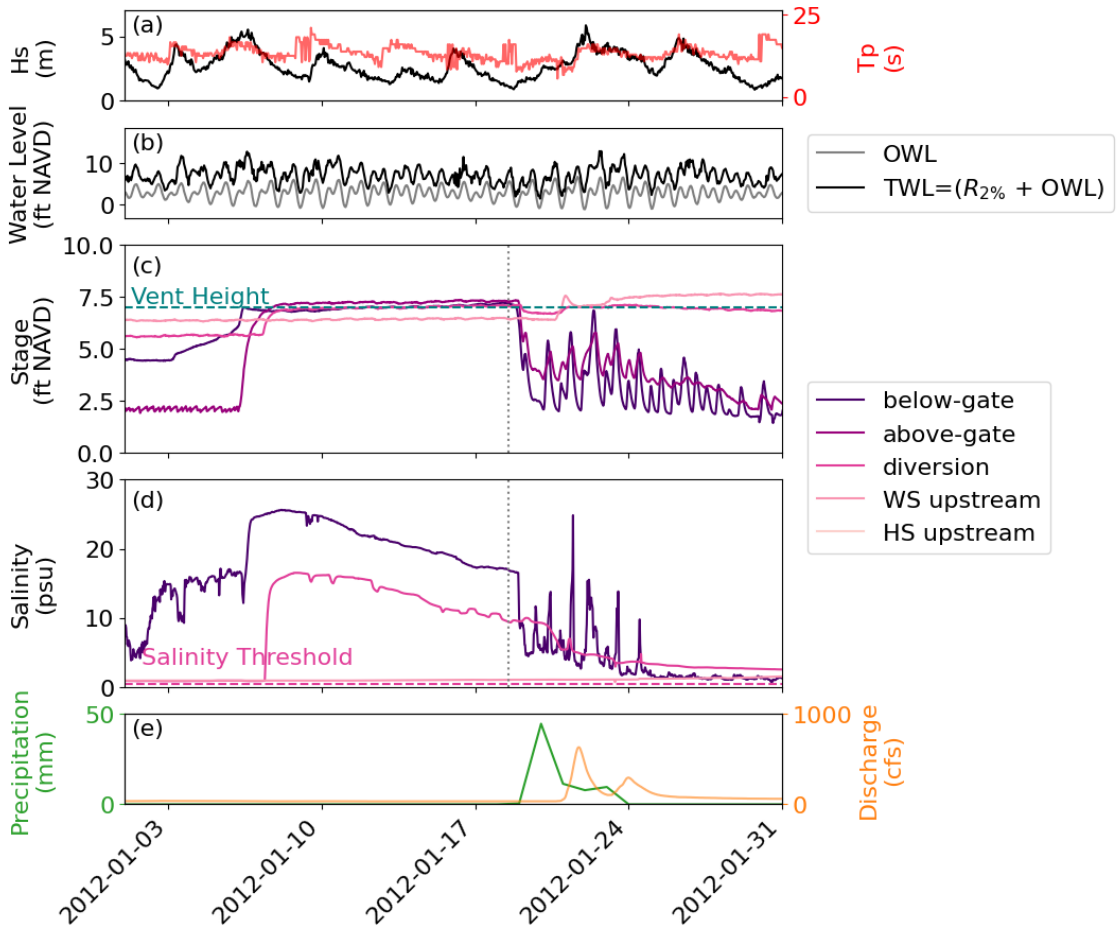

Figure 3.6. Coastal to inland stage and salinity connectivity under wet/extreme conditions over 1 month (January 1, 2012–January 31 2012). (a) Significant wave height (Hs) and peak period (Tp); (b) offshore water level (OWL and total water level (TWL); (c) stage at the below-gate, above-gate, diversion, and upstream stations, with the elevation of the tide gate vent (dashed turquoise line); (d) salinity at the below-gate, diversion, and upstream stations with the salinity threshold for diversion (dashed line); (e) precipitation and Pajaro River discharge. Note that the estuary mouth was closed at the start of this record. The vertical gray dotted line indicates when the mouth was manually breached by the County of Santa Cruz on January 18, 2012 (no time listed). Note vertical axes on (a), (d), (e) are different from Figure 3.5 (dry/baseline conditions).

high-stage events when below-gate waters overtop the tide gate, which typically co-occurs with periods when the lagoon mouth is closed. The closed-mouth state and slough SWI event that occurred in January 2012 illustrates this wet/extreme condition connectivity

between the ocean, lagoon, and slough (Figure 3.6), which resulted in salinity levels exceeding the threshold at which freshwater diversion from the HWS was allowable.

In a previous investigation by PV Water (Balance Hydrologics, 2014), below-gate stage and salinity conditions were assessed with respect to wave height, and findings supported an association between wave height and overtopping, Pajaro River discharge, lagoon mouth closures, and below-gate salinity. During the closed-mouth state in January 2012, indicated by non-tidal below-gate water levels (Figure 3.6 (c)), large wave heights drove overtopping of seawater over the sill at the mouth, into the lagoon, and thus increases in stage and salinity within the lagoon were observed. High, non-tidal, water levels were sustained until the occurrence of a sill breaching event, which was manual in this case. Here, we additionally connected this previously-documented January SWI event with supplemental oceanic measurements (Hs, Tp, OWL, and TWL) and measurements of stage and salinity at multiple sites above the tide gate in order to observe specific lag times at which stage and salinity increases propagated upstream.

We observed that high significant wave heights and corresponding long peak periods (Figure 3.6 (a)), which together resulted in high TWL (Figure 3.6 (b)), coincided with the rapid rise in stage at the below-gate site (i.e., in the lagoon), which propagated upstream through and over the tide gate. Specifically, on January 6th, 2012, in association with maximum TWL within a 31 day period (Figure 3.6 (a) and (b)), stage at the below-gate site (Figure 3.6 (c)) was high enough to overtop the vents located at the top of the tide gate (7 ft NAVD), thus establishing connectivity across the tide gate. This is evidenced by an increase in stage from 2.4 ft NAVD to 7.1 ft NAVD at the above-gate site, which began 1 hour after the below-gate stage reached the vent height (7 ft NAVD). At the time of vent overtopping, salinity levels at the below-gate site were near oceanic levels at 27 psu. The increase in stage above the gate then propagated further upstream and reached the diversion point 26 hours later, at which point stage increased by 1.2 ft (Figure 3.6 (c)). Salinity at the diversion site also increased at a 24 hours lag following vent overtopping,

reaching 16 psu (Figure 3.6 (d)). An investigation of this event by Balance Hydrologics suggests that roughly 270 af of ocean water moved into the HWS (Balance Hydrologics, 2014).

Dissimilar from the more immediate salinity increases that occurred at the above-gate and diversion sites following the vent overtopping, increases in salinity at the WS upstream site were not immediately observed in the logger data (Figure 3.6 (c)). Instead, increases in salinity at the WS upstream site were smaller, and more gradual and delayed. Relatively small salinity increases started approximately 6 days later on January 12th, 2012, and were observed as both a spike in grab sample salinity accompanied by a subsequent slow longer-term climb in logger salinity (Supplementary Figure S4). For salinity incursions to occur in the Watsonville Slough, the SWI event must be sizable due to the slough's steeper channel gradient compared to the gradient at the confluence of the Harkins and Watsonville sloughs, which directs the water's preferential flow path up the Harkins slough. When reverse flow of saline waters does pass the diversion site in the Watsonville Slough, this reverse flow resembles a slow-moving, low-sitting plume that may vertically stratify. During this event, PV Water observed that salinity incursion also went into and stratified within the deeper body of Harkins Slough, as far as a point located 2.5 km upstream of the Harkins-Watsonville confluence; the freshwater diversion site is located just downstream of this confluence. Specifically, grab sample salinity measurements at two Harkins Slough locations located 350 m and 2.5 km upstream of the Harkins-Watsonville confluence (Supplementary Figure S3) show elevated salinity levels in February and extending through the rest of the 2012 water year (Supplementary Figure S4). In subsequent years, PV Water also observed that runoff events would mix the stratified saline water and further limited the ability to divert water.

The lagoon mouth was opened through manual breaching on January 18, 2012 and was followed by a precipitation and discharge event in the Pajaro River (Figure 3.6 (e)) which helped naturally decrease the lagoon's stage and salinity levels (Balance Hydrologics,

2014). At this point in time, we observed an accompanying drop in stage at the diversion, above-gate, and below-gate sites, and tidal influences on stage returned at the below-gate and above-gate sites, indicating connectivity across the gates during open gate discharge, and an open lagoon mouth. With the onset of precipitation, stage increased at the WS upstream site (and presumably in the upper HWS as well, although this was unmeasured) due to freshwater flow. At the same time, with the lagoon mouth breach and onset of precipitation and discharge, below-gate salinity dropped rapidly and experienced tidal fluctuations (as with stage). However, diversion site salinity dropped much more slowly over time, and remained above the MAR diversion threshold through the entirety of the remaining wet season months; ultimately, there was no freshwater diversion possible during this year. This, combined with reports from water managers that freshwater flow would mix lingering vertically-stratified salinity in upper reaches of the HWS, indicates that SWI impacts on freshwater use may far exceed the duration of the SWI event itself.

February–March 2014: SWI following vent overtopping during a closed lagoon and high tide, and a subsequent breach coincident with storm-driven freshwater flow

A persistent lack of tidal variability in stage was evident at the below-gate site during the February 5th–March 7th, 2014 time period (Figure 3.7), which is attributable to a prior lagoon mouth closure. The precise closure date cannot be determined with study data due to missing stage data in early 2013 through November 2013. However, a lack of tidal stage oscillations between the measured period beginning in November 2013 until the end of February 2014 suggests that the closure occurred during the period of missing data. A manual breach on February 28th, 2014 occurred just prior to a large wave and TWL event (Figure 3.7 (a) and (b)) and a moderate precipitation and discharge event (Figure 3.7 (e)).

Similar to the 2012 case, during a lagoon mouth closure, vent overtopping occurred and coincided with reverse flow of saline water up into the HWS, leading to increased

salinity levels at the diversion site. Upon manual lagoon breaching, the below-gate stage immediately decreased and tidal variability returned. Diversion site salinity decreased, but slowly – remaining above the freshwater diversion threshold for another month at a minimum; there is a gap in the logger record after March 25th, 2014, but grab sample salinity confirms an eventual decrease (Supplementary Figure S5).

Dissimilar to the 2012 case, the 2014 vent overtopping did not coincide with a high wave and TWL event. Rather, it occurred with increasing OWLs during a transition to a spring tide (during which higher tidal amplitudes occur), suggesting that the sill was overtopped due to higher tidal water levels, and when lagoon water levels were already high following the prior closure. Both the 2012 and 2014 events had a high wave and TWL event that occurred after a lagoon mouth breach, and coincident with a precipitation and discharge event. Following the breach, neither of these coincident events (high TWL and discharge) resulted in upstream flow of saline water due to the open estuary mouth and increased river discharge driving overall lower water levels and downstream flow directions in the slough. Both the 2012 and 2014 overtopping and SWI events occurred during closed mouth conditions, which is important in setting the high background estuary water levels on top of which high wave and TWL events can induce SWI. The much higher salinity values during the 2012 SWI event, relative to the 2014 event, suggest that high wave and TWL events, coincident with lagoon mouth overtopping and closure conditions, exacerbate SWI.

October–December 2016: SWI following vent overtopping during a closed lagoon and high TWL, and a subsequent manual breach with no coincident storm-driven freshwater flow

The period between October 1, 2016–December 10, 2016 (Figure 3.8) is notable due to oceanic and inland conditions that occurred during an extended closure period (October 16, 2016–December 1, 2016) and an ensuing SWI event between November 7, 2016 and December 5, 2016. Therein, CSC carried out an emergency manual breach on December 1,

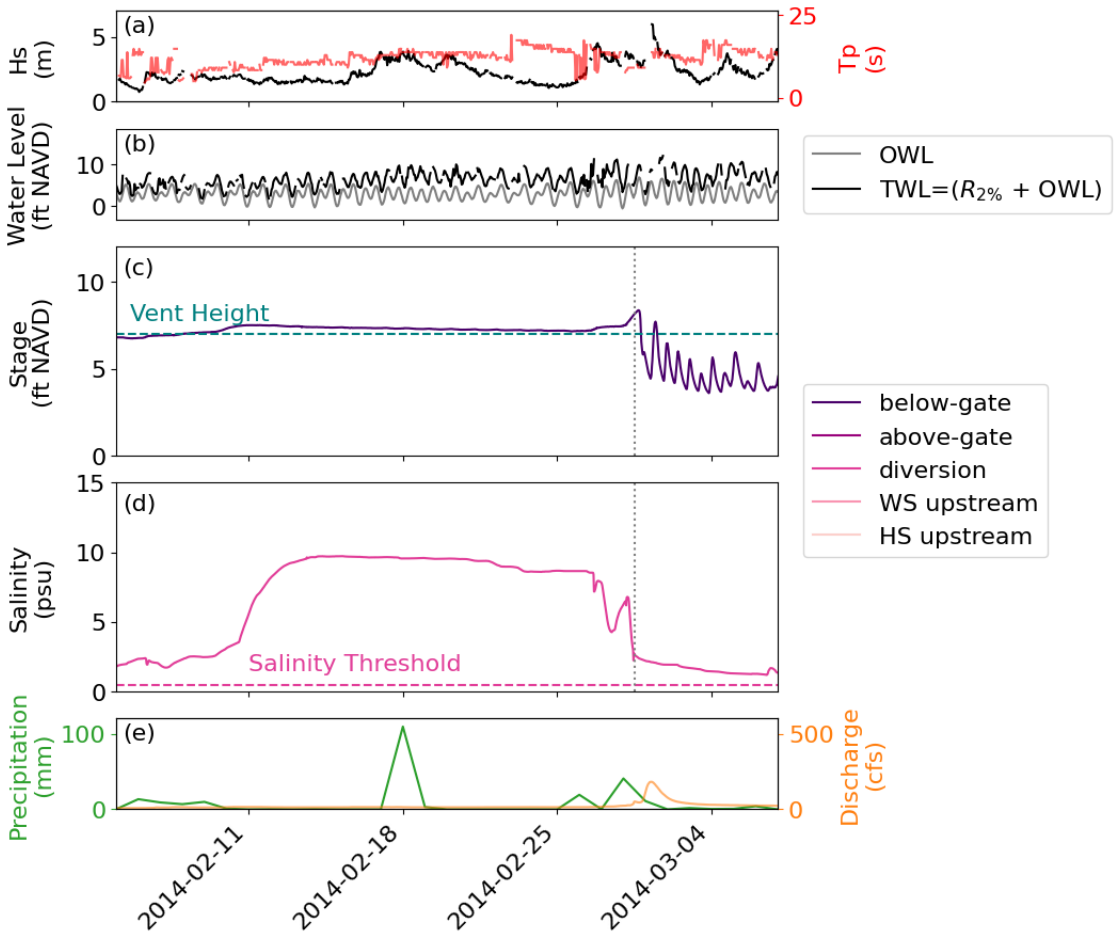

Figure 3.7. Coastal to inland stage and salinity connectivity under wet/extreme conditions over 1 month (February 5, 2014–March 7, 2014). (a) Significant wave height (Hs) and peak period (Tp); (b) offshore water level (OWL) and total water level (TWL); (c) stage at the below-gate site (above-gate, diversion, and upstream stage data missing during this time), with the elevation of the tide gate vent (dashed turquoise line); (d) salinity at the diversion station (below-gate and upstream salinity data missing during this time) with the salinity threshold for diversion (dashed line); (e) precipitation and Pajaro River discharge. The vertical gray dotted line indicates when the mouth was manually breached by the County of Santa Cruz on February 28, 2014 (no time listed)

2016, but the Pajaro river was not fully draining through the lagoon until December 5, 2016. This event in many ways resembles the 2012 event, with several differences. Due to the increased fidelity of monitoring available during this time period (relative to earlier years), the 2016 event more comprehensively demonstrates full HWS system behavior

during and following a lagoon mouth closure with wave overtopping, and how the system responds to a manual breach of the mouth, especially regarding the persistence of slough salinity. Additionally, the 2016 event demonstrates salinity conditions at, and upstream of the diversion site under conditions wherein there was no precipitation-driven runoff event coincident with the lagoon mouth breach itself, as there was in 2012.

The onset of lagoon closure during the latter half of October, marked by the rising of below-gate stage and loss of tidal variability, appears to have been a function of wave-driven high TWL events and relatively low early wet season discharge. However, the precipitation and consequential discharge event in mid-October likely eroded the berm height, but did not fully open the lagoon, as evidenced by the drop in below-gate stage levels between October 17th and October 22nd that then hovered around 6 ft NAVD (Harvey et al., 2020). Stage at this site did not significantly increase again until early November. During the first 11 days of November 2016, which centered on a neap tide (a period of time during which there were mostly lower tidal amplitudes), several large waves events with long periods drove increases of stage at the below-gate sensor, which eventually propagated to upstream sites once the 7 ft NAVD vent threshold was reached. Concurrently, salinity moved upstream into the Watsonville Slough, including at the diversion site, and potentially briefly into upstream segments of the Harkins Slough (Supplementary Figure S6). Salinity at the diversion site remained high throughout the closure, although it began to steadily decrease after November 19th and prior to the manual breach. Following the manual breach on December 1st, the diversion site salinity continued to decline for the next several months (Supplementary Figure S6). Salinity at the above-gate site remained elevated throughout the closure, and only decreased after the manual breach.

This example emphasizes that the combination of OWL and wave runup within TWL are important to understanding wave overtopping and SWI in this system, as wave overtopping of the closed lagoon mouth occurred in early November, despite the reduced OWL during neap (low amplitude) tides. Similar to the 2012 event, both logger and

grab sample salinity measurements demonstrate that saltwater moved upstream past the diversion site to the WS upstream site and likely stratified vertically there. By mid December 2016, the WS upstream site's logger salinity levels exceeded those at the diversion site, and remained higher than at the diversion site until mid-January 2017 (Supplementary Figure S6) when precipitation and discharge finally drove down upstream salinity levels (Figure 3.9). Thus, the 2016 event confirms prior understanding of the 2012 event (Balance Hydrologics, 2014), bolstering the argument that the confluence of low precipitation and discharge, lagoon closure, and high wave and TWL conditions constitute a recurrent feature of the Pajaro estuary system highly relevant to water supply planning.

December 2016–January 2017: No SWI following vent overtopping during open lagoon, high TWL, and high storm-driven freshwater flow conditions

The period between December 10, 2016–February 1, 2017 (Figure 3.9) immediately follows the 2016 period (Figure 3.8). As in December, 2016, January 2017 is characterized by continuing post-breach declines in salinity. However, in January, the lagoon mouth remained open, and there were multiple precipitation events over a 13 day span that drove 3 large discharge events, which were some of the largest seen during the study period. In January 2017, precipitation and discharge were responsible for slough stage increases that propagated downstream, sequentially raising stages (with short $<$ 1 hour lag times) at the upstream, diversion, above-gate, and below-gate sites – briefly above the vent height. Downstream flow opened the tide gates, allowing tidal connectivity across the gates: stage at the above-gate site oscillated tidally with stage fluctuations at the below-gate site due to the open gate conditions during downstream flow (Figure 3.9). Until the onset of precipitation in early January, relatively high salinity had persisted at the diversion site stemming from the previous closure (Figure 3.8), but with sustained precipitation and discharge, salinity gradually declined to pre-SWI levels by February, 2017 (Supplementary Figure S6).

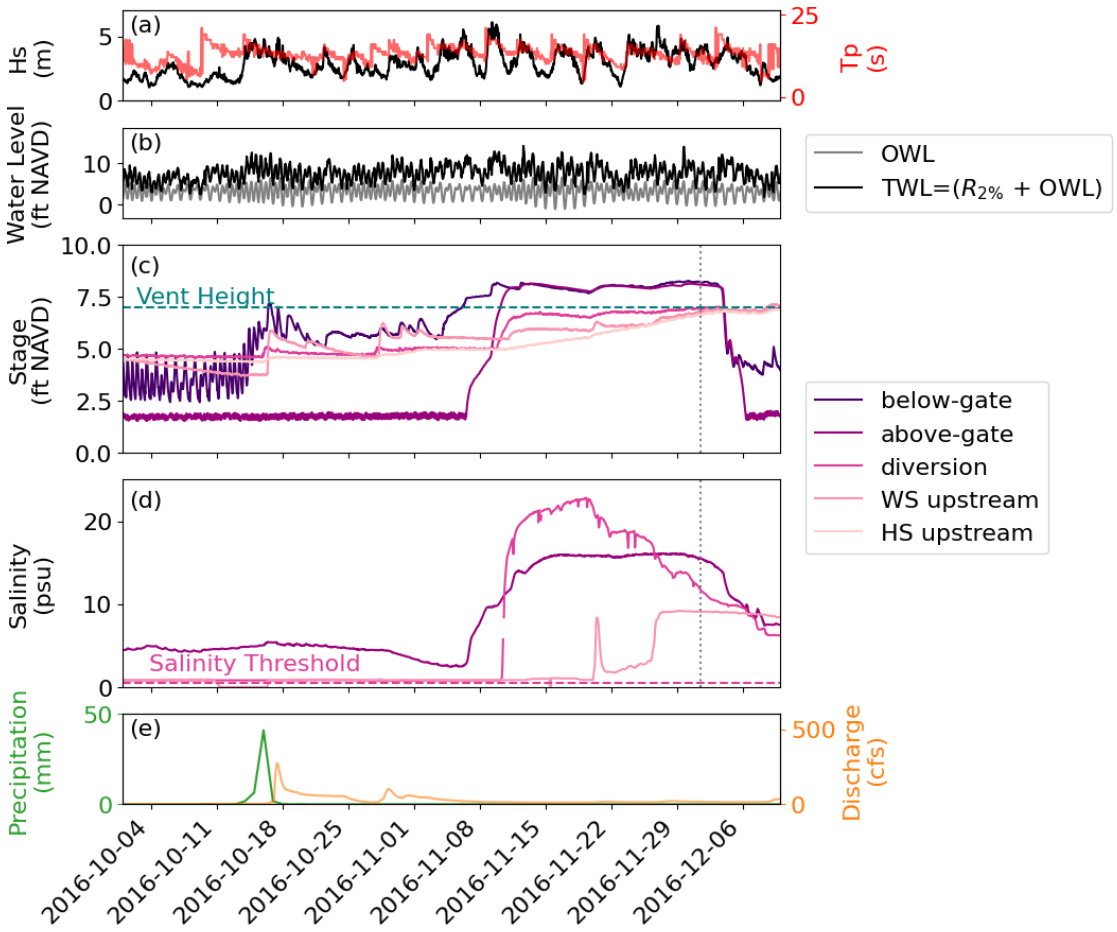

Figure 3.8. Coastal to inland stage and salinity connectivity under wet/extreme conditions over 2.3 months (October 1, 2016–December 10, 2016). (a) Significant wave height (Hs) and peak period (Tp); (b) offshore water level (OWL) and total water level (TWL); (c) stage at the below-gate, above-gate, diversion, and upstream stations, with the elevation of the tide gate vent (dashed turquoise line); (d) salinity at the below-gate, diversion, and upstream stations with the salinity threshold for diversion (dashed line); (e) precipitation and Pajaro River discharge. The vertical gray dotted line indicates when the mouth was manually breached by the County of Santa Cruz on December 1, 2016 (no time listed).

During this time period, moderately-sized wave events did occur, but coincided with precipitation and discharge that drove substantial downstream flow. At the tide gates, two brief vent overtopping events occurred (1/9/2017, 1/21/2017) due to a combination of heightened TWL and storm-driven (downstream) discharge in the HWS, which occurred

during open lagoon conditions. The maximum Harkins and Watsonville Slough stage values were reached when large wave events with long periods (thus high TWL) coincided with high precipitation and discharge. The first vent overtopping event occurred during a spring (high amplitude) tide, and the second event occurred during coincident large, long period waves during a neap (low amplitude) tide. Both vent overtopping events occurred despite different tide conditions, and during an open lagoon mouth, wherein overtopping was enabled by pre-existing discharge-driven high stage levels. Salinity levels continued to decline during vent overtopping. Thus, high wave and TWL, in the absence of a lagoon mouth closure, and with high rather than low flow river discharge conditions, did not result in SWI. This example demonstrates how ocean conditions alone do not drive surface SWI in systems like the Pajaro River estuary.

3.5.3 SWI Event Typology

In observing time series patterns across multiple years' wet periods (Figures 3.6-3.9, Figures S4-S6), a typology of ocean-inland interactions emerges, which we quantify statistically (Figure 3.10, see Methods). For events in which SWI occurred (Figure 3.10 (a)), high percentiles from November-May observations of Hs (median 95th percentile), Tp (median 85th percentile), and TWL (median 84th percentile) coincide with relatively low percentiles of freshwater flow as measured by WS upstream stage (median 17th percentile) and Pajaro River discharge (median 37th percentile); these conditions occurred predominantly while the Pajaro River lagoon mouth was closed.

This pattern is distinct from the distribution of these same variables for overtopping events without SWI (Figure 3.10 (b)) and non-overtopping events (Figure 3.10 (c)). These two event types are described by a wider range of oceanic and hydrologic conditions, have lower median percentiles of Hs, Tp, and TWL, and higher median percentiles of WS upstream stage and Pajaro River discharge. For overtopping events without SWI, WS upstream stage and Pajaro River discharge percentiles are much higher (median 78th

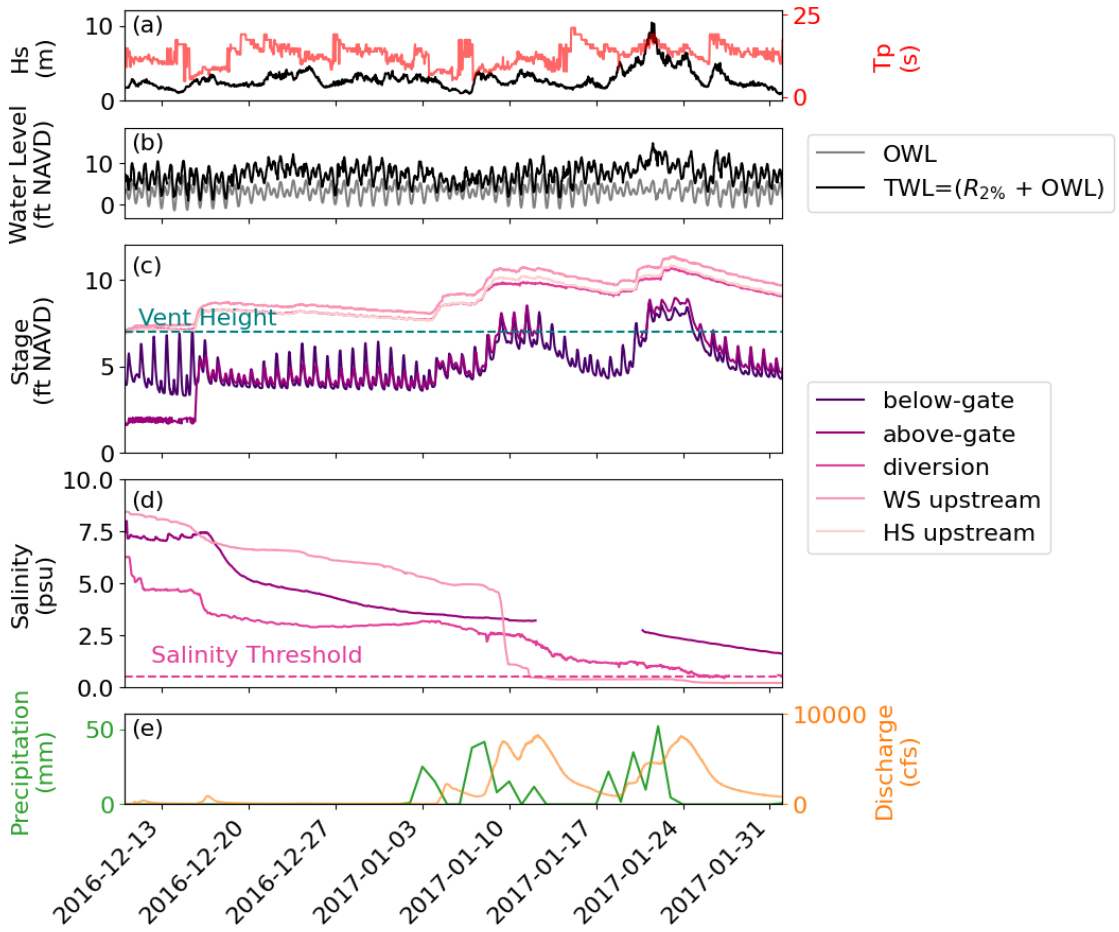

Figure 3.9. Coastal to inland stage and salinity connectivity under wet/extreme conditions over 1.6 months (December 10, 2016-February 1, 2017). (a) Significant wave height (Hs) and peak period (Tp); (b) offshore water level (OWL) and total water level (TWL); (c) stage at the below-gate, above-gate, diversion, and upstream stations, with the elevation of the tide gate vent (dashed turquoise line); (d) salinity at the below-gate, diversion, and upstream stations with the salinity threshold for diversion (dashed line); (e) precipitation and Pajaro River discharge.

percentile and 80th percentile, respectively) than those seen during overtopping events with SWI. Overtopping events without SWI occurred predominantly while the Pajaro River lagoon mouth was open (66% of observations were during open periods). Overtopping events without SWI encompass conditions during which discharge in the HWS causes increases in stage above the tide gates, coincident with discharge in the Pajaro River

that maintains open lagoon conditions, and conditions in which below-gate stage is high enough to overtop the tide gate vents, but salinity is not affected due to predominantly downstream flow and/or brief enough timescales of vent overtopping. High stage but non-overtopping events with/without SWI (Figure 3.10 (c)) represent a control condition that establishes that the patterns observed for overtopping events (SWI and non-SWI) are distinct from otherwise similar events. For the non-overtopping events, there is a wide range of percentiles for most variables, representing the range of conditions under which stage downstream of the tide gates may reach levels close to the tide gate height, without overtopping.

This analysis relied on a necessarily limited number of suitable overtopping events with (4) and without (32) SWI. Nevertheless, the identified pattern (Figure 3.10) is consistent with and extends the prior qualitative understanding of the joint role of lagoon closure and high TWL in the January 2012 event (Balance Hydrologics, 2014). This analysis therefore highlights the utility and potential generalizability of analyzing specific variable (TWL, stage, discharge) statistics. We conclude that high significant wave height (median 95th percentile), long wave period (median 85th percentile) and thus high total water levels (median 84th percentile), in association with distinctly low flow conditions in the HWS system (median 17th percentile of diversion period WS upstream stage) and through the Pajaro River lagoon (median 37th percentile of diversion period discharge) are associated with SWI at levels that affect coastal freshwater use in the Pajaro Valley.

While we expect that the availability of additional SWI event samples would alter these percentile thresholds, we expect the identified pattern (high ocean levels coupled with low inland stage/discharge) to persist; according to our leave-one-out event sensitivity analysis, the identified percentile medians varied by ± 5 percentile units. Notably, the February 2014 event was distinct from the other three SWI events because of high background stage levels due to a prior lagoon closure that allowed for a SWI event without a particularly high TWL event (Figure 3.7). This is evident in the leave-one-out sensitivity

analysis, which indicates that the removal of this event from the statistical analysis narrows the range of Hs, Tp, and TWL percentiles under which SWI occurs in this system (Supplementary Figure S7 (b)). Additionally, this sensitivity analysis suggests that the lack of upstream stage data for 2 of the 4 SWI events does not greatly affect the median percentile of the WS upstream variable during SWI events. The median of the related inland flow variable, Pajaro River discharge, increases marginally with the removal of the 2014 event (Supplementary Figure S7 (b)), but does not change with the removal of the 2018 event (Supplementary Figure S7 (d)). Thus it is reasonable to assume that the range of upstream stage could grow wider and the median of upstream stage could slightly increase if upstream stage data were available during these two events, however we expect that the percentiles would remain distinctly low. Lastly, the sensitivity analysis in which we varied the number of hours included prior to and immediately following events (Supplementary Figure S8) demonstrated that a longer event time frame increased the number of outliers for some variables, and the pattern identified for SWI events slightly diminished, suggesting that the timescale of the overtopping events relevant to SWI occurs within a tidal cycle.

Complicating this analysis is the fact that drivers of lagoon mouth closure and SWI are very similar in the Pajaro system, although they may be more or less similar in other systems – depending on estuary dynamics and infrastructure (e.g., presence or absence of tide gates). 3 of 4 SWI events occurred when the lagoon was in a fully closed-mouth state and 1 occurred coincidentally with a closure, whereas 66% of non-SWI and high stage events occurred when the lagoon was in an open-mouth state (Supplementary Table S2). An SWI event in January 2018 occurred 9 days after the lagoon had been mechanically breached. However, below-gate stage records indicate that the mouth coincidentally closed during the high TWL event (the highest recorded during our study period) that caused the SWI event (Supplementary Figure S9). This indicates that lagoon closures are part of the identified oceanic and hydrologic process that drives propagation of saline water

upstream in this particular system. Prior research has shown that large waves alongside weak downstream flow (discharge or outflow) or strong upstream flow (e.g., strong flood tides) can lead to sill accretion and closure, while strong downstream flow leads to sill erosion and opening (Largier et al., 1992; Clark, O'Connor, 2019; Behrens et al., 2013; Orescanin et al., 2021). Here, the lagoon mouth must be closed, or have been recently closed to allow lagoon water levels to build up high enough to overtop the tide gate vents from the downstream side. High discharge conditions can not only force downstream flow and eliminate the possibility of SWI, they can also maintain or create an open estuary mouth. We therefore acknowledge that low river discharge and flow conditions are drivers for both our observed SWI events and for maintaining a closed-mouth state at the lagoon (Orescanin et al., 2021). Further investigation of this phenomenon and its generalizability would require more regular lagoon mouth observations in conjunction with more SWI event samples – here and in other systems.

The presence of tide gates complicates the estuarine dynamics in this system. Without these tide gates, salinity intrusions would likely be able to move further upstream under closed and open lagoon mouth conditions. Under open conditions, in bar-built estuaries, salinity likely moves inland via some variation of flood tide intrusion controlled by internal hydraulics, followed by a basal density current (Largier, Taljaard, 1991). Though most studies of bar-built estuaries during closures focus on the biogeochemical drivers that may contribute to hypoxia/anoxia, a few studies observed the mechanisms of landward salinity movement. At the Russian River in Northern California following lagoon mouth closures, salinity moved upstream into areas usually devoid of saline water under open conditions within two separate phases. The first phase was driven by the relaxation of longitudinal gradients in the outer estuary, which initiated a rapid intrusion of near-bottom saline water that was blocked by bathymetric sills in the estuary. In the second phase, these sills aided in one-directional wind-driven movement of saline water upstream as a gravity current, which became trapped in bathymetric deep pools (Behrens et al., 2016). Similar

sills and deep pools are present in the HWS slough system, and we hypothesize that deep pool trapping may be occurring according to previous reports (Balance Hydrologics, 2014) and observations made by PV Water (e.g., grab sample documentation of upstream slough salinity mixing in the months following an otherwise concluded SWI event). Nevertheless, the presence of tide gates interrupts similar salinity intrusion mechanisms and distances in the HWS. Given the high elevation of the tide gates and the vents that allow for saline water to move upstream only under high stage conditions below the tide gate (aside from some upstream leakage through closed tide gates), estuary mouth closure and wave overtopping of the closed mouth are likely necessary for stage to increase to levels high enough to reach the tide gate vents and drive reverse flow and SWI.

Notably, even very short SWI events result in elevated salinity in the HWS system – at the freshwater diversion site and further upstream – for weeks to months past the SWI event itself. On average, according to logger salinity data, it took 25 weeks after the onset of a SWI for salinity levels at the HWS diversion site to return to levels that permit freshwater diversion; this length of time represents 48% of the entire allowable diversion period each winter season. However, for some events, like the January 2012 vent overtopping, diversion was impacted for years due to upstream stratification of salinity in the water column. This significantly impacts the amount of water that may be diverted in a given year from the HWS. In the water years during which a SWI event occurred (2012–2014, 2016–2017, 2019), freshwater diversion volumes were approximately half the diversion volumes in years where no SWI event occurred (2009–2011, 2015, 2018, 2020). In the PV Water case, these freshwater diversions supply a MAR project intended to help limit withdrawal from critical coastal groundwater aquifers. Thus, ironically, a MAR project intended to help a coastal region adapt to the impacts of climate variability and change on groundwater is stymied by the impact of that same climate variability and change on the surface water system.

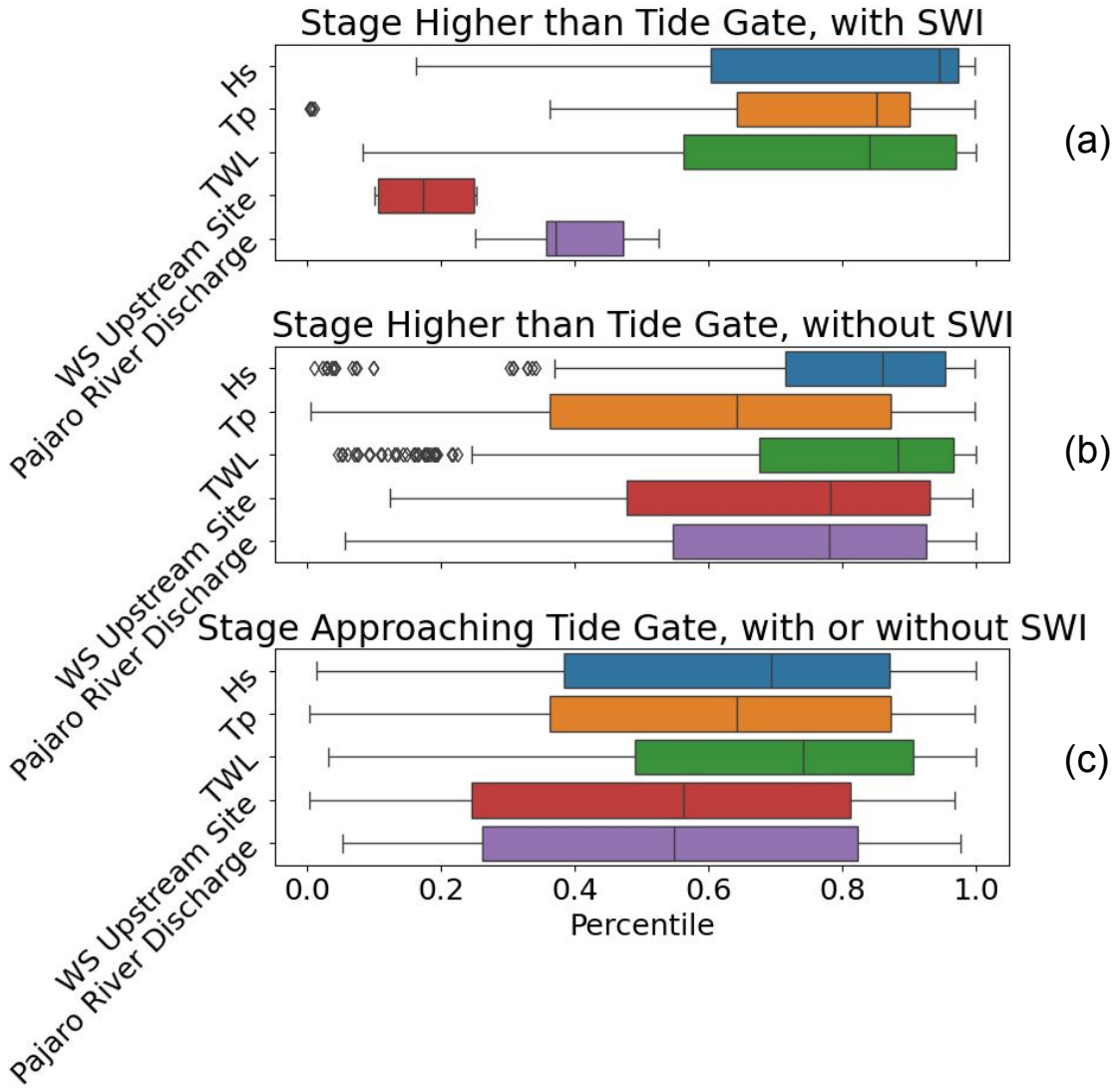

Figure 3.10. Distribution of offshore and inland hydrologic variables during tide gate overtopping events with and without SWI. (a) tide gate overtopping events with associated SWI; (b) tide gate overtopping events without associated SWI; (c) high stage events that approach but do not overtop the tide gate vent, with or without SWI. Data summarized in all panels include percentiles, relative to all November - May freshwater diversion period observations of each variable across all years (2012-2020), of significant wave height (Hs), peak wave period (Tp), total water level (TWL), WS upstream site stage, and Pajaro River discharge within the (13-hour) time periods of events categorized within the three event types (a, b, c).

3.5.4 Water management implications

Surface SWI events have substantially impacted PV Water's ability to operate their existing MAR facility and pose a challenge for similar future projects. More broadly, SWI has impeded the region's progress toward an overarching goal of achieving groundwater sustainability while maintaining existing beneficial water uses. Nevertheless, water planning and infrastructure investments are proceeding despite data limitations and uncertainty, highlighting the importance of the present research.

In response to documented surface SWI events (Figures 3.6-3.8) and associated freshwater diversion deficits (Figure 3.2), and alongside the continued updating and development of other inland supplemental water supply projects, PV Water plans to improve its existing MAR facility and also develop an additional new MAR facility (202, 2023b). Specifically, a second MAR diversion site will be located further upstream than the present site, approximately 1,150 meters upstream of the WS Upstream site (see Figure 3.1) in order to provide greater resiliency to SWI (Pajaro Valley Water Management Agency, Carollo, 2018). This greater resiliency and improved operational capability is critical given that diverted water is ultimately delivered to coastal growers and utilized in lieu of pumping groundwater in the coastal areas that are historically affected by aquifer SWI. Single year and multi-year water quality impacts that result from SWI events pose a significant risk of limiting or prohibiting MAR operations, which could result in lost opportunities to divert thousands of acre-feet of supplemental supply water. It remains that larger SWI events have reached the new proposed upstream site for freshwater diversion (i.e., the WS Upstream site in the 2012 and 2016 events, see Figures 3.6 and 3.8). Additionally, post-SWI event salinity has been observed to persist in upstream slough locations within vertically stratified water (see Figures S4 and S6). This underlines the importance of understanding the conditions that contribute to SWI events, including estuary flushing dynamics in stratified systems and in the presence of deep salt pools, as well as assessments

of potential measures to mitigate their occurrence.

PV Water is proceeding with its MAR plans while also anticipating SWI risk will increase with sea level rise and inland hydrologic variability as a result of climate change. This reality poses the question to PV Water, and coastal water managers globally, of how frequently large surface SWI events will occur in a climate changed future. While we leave this question for future research, the present study reveals key process understanding and simple analytical tools – joint threshold quantification based on observational ocean and hydrology data (Figure 3.10) - that are critical for beginning to answer questions about the timing, frequency, and magnitude of water supply-relevant SWI in the Pajaro Valley, and that are replicable in other coastal regions.

3.6 Conclusions

This study represents an important step in the process of quantifying system variables and drivers of freshwater constraints in coastal systems, a hydrologic domain of research that is increasingly important with climate change, but understudied relative to other hydrologic domains. Pulses of saline ocean water disrupt capacity to divert freshwater along coasts, making coastal hydrodynamic processes directly relevant to the sustainability of inland freshwater management – in the Pajaro Valley, and in other regions facing similarly complex ocean-inland connectivity. Our results demonstrate that offshore and inland hydrologic drivers jointly determine coastal freshwater use capacity, the quantification of which is novel and presently limited globally. Our findings complement those of previous surface water SWI studies in other locations that find that both sea levels and inland hydrologic conditions modify the extent of SWI (Rice et al., 2012). Additionally, results complement those of coastal flooding studies in which the extreme event of flooding, rather than SWI, is similarly attributed to the co-occurrence of joint drivers (Lucey, Gallien, 2022; Ward et al., 2018). Previous work on salinity intrusions in

estuaries suggests that discharge, OWL, and wind may be factors in driving upstream SWI at various timescales (MacCready, 2004; Behrens et al., 2016; Tian, 2019). In the HWS system, which has been heavily modified by infrastructure, TWL (the combination of OWL and wave runup) and low upstream flow conditions coupled with a closed lagoon mouth appear to consistently drive SWI at the event timescale.

The methods used in this study are readily exportable to other coastal regions, and involve simple empirical approaches that can be used by practitioners to improve local to regional understanding of surface water SWI. With the availability of similar datasets – measured or modeled, this approach is replicable in other environments. Specifically, because SWI-relevant thresholds can be calculated using only ocean level and hydrologic stage/discharge measurements, for which the record is more comprehensive than when also including salinity, it is possible to use observation-based thresholds to identify change in the occurrence and frequency of threshold events throughout the historical record and under modeled future conditions. We leave this exercise for future research.

As a case study, our data and analyses are specific to the Pajaro Valley, but are nevertheless relevant to coastal regions elsewhere, and especially to other low-inflow bar-built estuaries, which constitute a significant fraction of coastal communities along the U.S. Pacific Coast. The Pajaro Valley is not alone in facing SWI challenges to freshwater (Rodrigues et al., 2019; Medellín-Azuara et al., 2014; Hong, Shen, 2012; Knowles et al., 2018; Chen et al., 2016). Thus, these findings are not only important to help guide water management decisions in a specific location, but are also novel and extensible in their synthesis of coastal oceanography, inland hydrology, and water management practices relevant to climate change adaptation in human-modified coastal water systems.

3.7 Acknowledgments

This work was funded by a combination of the following: a Hellman Fellows Program Award; a UCSD School of Global Policy and Strategy – Center on Global Transformation Policy Fellow Award; a University of California (UC) California (CA) Climate Action Matching Award, Application ID R02CM7222; a CA Department of Parks and Recreation Natural Resources Division's Oceanography Program under contract #C21820002 with Scripps Institution of Oceanography, UCSD; and NSF project #2044884. We would like to thank Jason Parke at Balance Hydrologics and Antonella Gentile at the County of Santa Cruz for their technical feedback.

Chapter 3, in full, has been submitted for publication as it may appear in Water Resources Research 2024. L.N. Kim, C. Meusel, R. Barker, B. Lockwood, M. Strudley, D. Behrens, M.M. Orescanin, M.A. Merrifield, S.N. Giddings, and M.C. Levy. The dissertation author was the primary investigator and author of this paper.

3.A Dry/Baseline Connectivity

We attempted to evaluate possible connectivity across below-gate and above-gate sites during the summer dry/baseline season, when the tide gates are typically closed but may experience leakage, by examining corresponding variability in stage at the below-gate and above-gate sites using a spectral analysis. The working assumption of both PV Water and CSC is that tide gate leakage occurs, but that it is sufficiently minimal for salinity management purposes. From a scientific perspective, and with respect to the question of establishing baseline ocean-slough connectivity conditions (rather than water management function) several factors motivated additional exploration of this baseline connectivity. First, gradually increasing levels of salinity were observed during several summer periods upstream of the tide gates, the causes of which were hypothesized to be tide gate leakage (unmeasured), agricultural return flow (unmeasured), or a combination of both; the cause

did not appear to be sensor drift according to comparison with available salinity grab samples. Second, stages at both the above-gate and diversion sites demonstrated small, potentially tidal fluctuations. Third, research in other ocean-connected freshwater estuaries has demonstrated that salinity transport can occur far upstream under sufficient vertical stratification and wind conditions (Behrens et al., 2016). Thus, we briefly evaluated connectivity across the tide gates (while lacking sufficiently detailed salinity data). We selected 30 min below-gate and above-gate stage between the months of June–August 2016 (which we use as a representative dry/baseline time period), and calculated the power spectral density (PSD) of the stage timeseries to identify the frequencies that account for the most timeseries variance. Additionally, we used barometric pressure (in millibars) data from the NOAA Monterey Bay tide gauge (downloaded at 6 min intervals and aggregated to 30 min intervals to match our stage datasets) and similarly calculated the PSD of the pressure timeseries. We then calculated the squared coherence between the below-gate and above-gate power spectral density estimates and between the pressure and above-gate PSD estimates to characterize the correlation between the spectral density estimates at each frequency.

The PSD of the below-gate site (Figure 3.C.2 (a)) shows variability in several tidal frequency bands (roughly 1, 2, 3, 4, and 5 cycles per day), with the most prominent peaks in the diurnal and semidiurnal tidal frequencies. The PSD of the above-gate site indicates that the stage record is dominated by mostly diurnal, with some semi-diurnal, variability. A coherence analysis across the below-gate and above-gate sites (Figure 3.C.2 (b)) show high coherence in the diurnal band, which may suggest that water is somehow moving across the tide gates in the upstream direction once a day, possibly on the higher high tides or via wind-driven movement. If the coherence were wind driven diurnal stage fluctuations (i.e., Behrens et al., 2016), we would expect stage peaks to occur at the same time every day. Analysis of the original time series (Figure 5 (c)) shows that above-gate and diversion stage peaks do not occur at the same time every day, but that they also don't

evolve in a way that appears tidal. A coherence analysis with barometric pressure (Figure 3.C.2 (b)) also indicates high coherence with above-gate stage in the diurnal band, which suggests that atmospheric pressure is likely playing a role in the small-scale fluctuations of stage above-gate. These analyses suggest that multiple drivers of variability in stage may be present. However, further observations would be needed to properly separate the contributions of each of these drivers.

3.B Supplementary tables

Table 3.B.1. Tide gate rules for interpretation of stage at above- and below-gate sites, shown on Figure 1 (c) and 3 (b).

Connectivity feature	Criteria (NAVD)	Description
Vent overtopping	below-gate or above-gate >= 7	Water flowing through vents above tide gate structure
Road overtopping	below-gate or above-gate >= 8.4	Water flowing over the road above the vents
Downstream flow	below-gate < above-gate	Water flowing downstream
Upstream leakage	below-gate > above-gate	Water potentially flowing through closed tide gate due to partial openings
downstream pump 1 flow, pump 2 flow	above-gate >= 2, above-gate >= 2.4	Pumps that move water upstream to downstream are on
Upstream-downstream connectivity	below-gate = above-gate	Tide gates are likely open and no longer blocking flow up or down stream

Table 3.B.2. Dates of gate overtopping events with SWI and the corresponding dates of nearest closure (before SWI event) and opening (after SWI event) of the lagoon mouth, as recorded by the CSC. For events 1, 2 and 4, observations of below-gate stage were missing prior to 12/2011, 12/2013, and 10/2017, respectively, and thus we were not able to identify a more specific closure date. *The opening date of event 4 is based on below-gate stage levels rather than CSC-identified opening dates due to the coincident closure during the event that occurred 9 days after a CSC manual breach.

Event	Event date	Lagoon mouth state	Closure date (approx.)	Open date (rec.)
1	1/6/2012	closed	before 12/2011	1/18/2012
2	2/7/2014	closed	before 12/2013	2/28/2014
3	11/5/2016	closed	10/16/2016	12/1/2016
4	1/17/2018	coincidentally closed	before 10/2017	1/29/2018*

3.C Supplementary figures

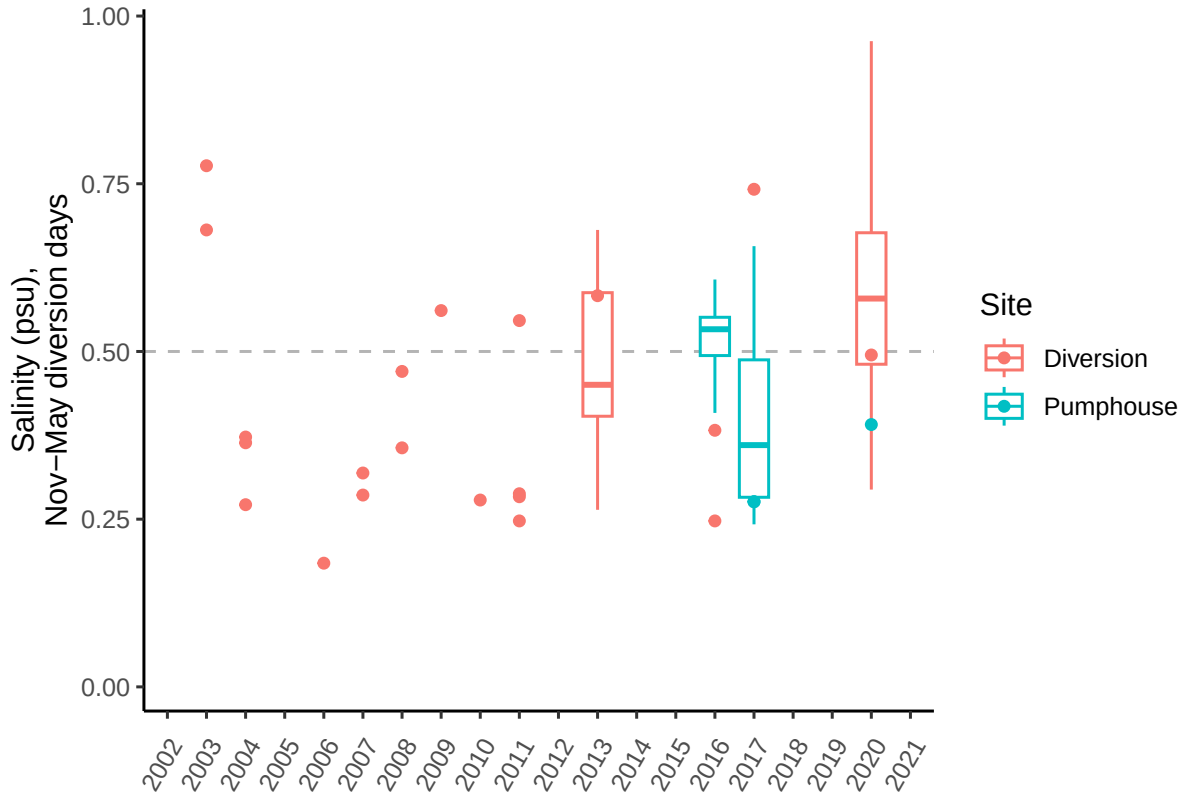

Figure 3.C.1. Salinity (psu) from 30 minute logger (boxplot) and monthly grab sample (point) data at the diversion and pumphouse sites (colors) for days on which PV Water diverted freshwater (only) during the 2002-2021 water years. The modeled salinity threshold for MAR diversion suitability is 0.5 psu (dashed line). Boxplot distributions show the interquartile range (IQR) boxes and $\pm 1.5*$ IQR whiskers of the 30 minute logger data, with outliers omitted from the visualization only.

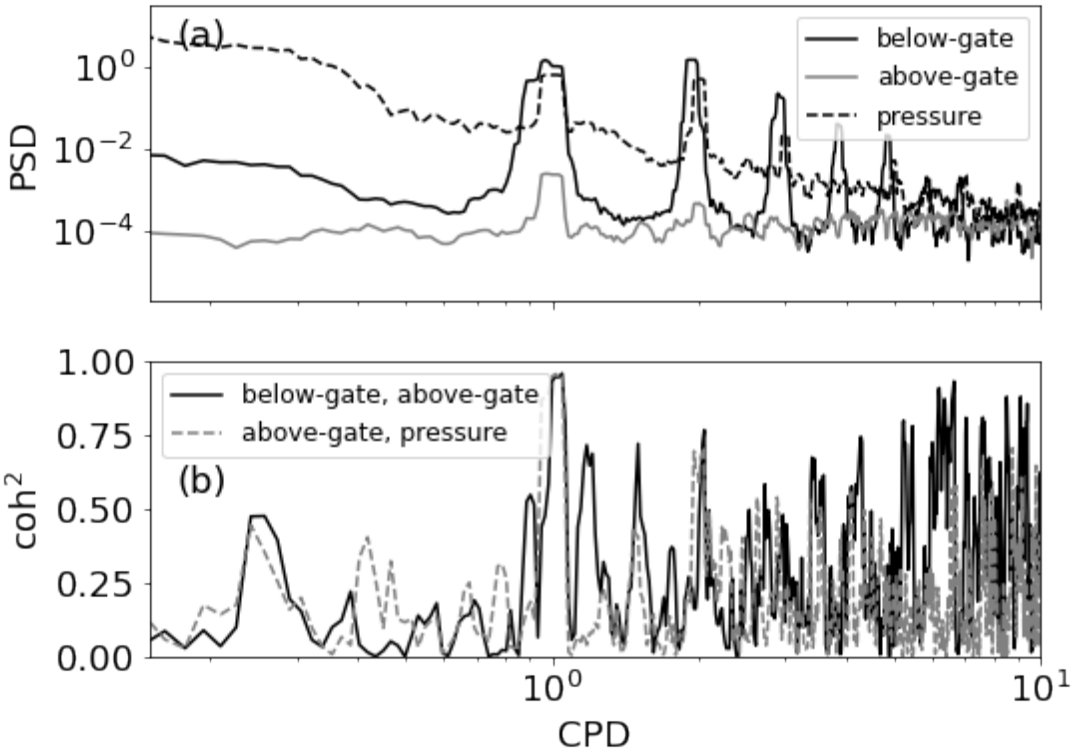

Figure 3.C.2. Power spectral density and Coherence between below-gate and above-gate stage and barometric pressure. (a) Power spectral density estimates for below-gate stage, above-gate stage, and barometric pressure from the NOAA tide gauge in units of ft $NAVD^2$/cycles/day for stage data and $millibars^2$/cycles/day for barometric pressure. (b) Calculated coherence-squared across frequencies between the below-gate and above-gate stage and between the above-gate stage and barometric pressure. Units of the x-axis are cycles per day (CPD).

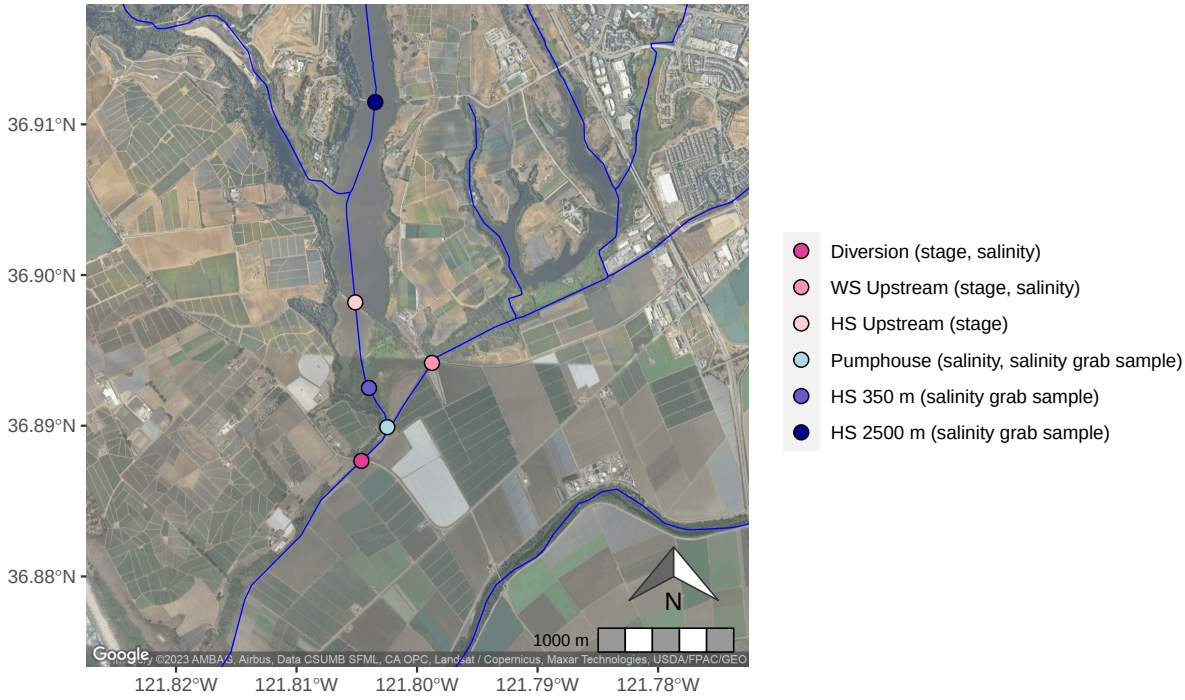

Figure 3.C.3. Salinity grab sample site locations. Location of the (MAR) Pumphouse, located 300 m upstream of the diversion site, and HS 350 m and HS 2500 m grab sample sites, which are located on the Harkins Slough 350 m and 2500 m upstream of the Harkins-Watsonville confluence (above the diversion point). Other sites (diversion, WS upstream, and HS upstream) refer to sites, and corresponding logger stage and salinity measurements, used in the main analysis (see Figure 1). Data source: Imagery sourced from Stamen and Google Maps imagery acquired through the R ggmap package (Kahle, Wickham, 2013); PV Water boundary and measurement site locations courtesy PV Water; river network is derived from National Hydrography Dataset Flowline data via the R nhdplusTools package (Blodgett, Johnson, 2022).

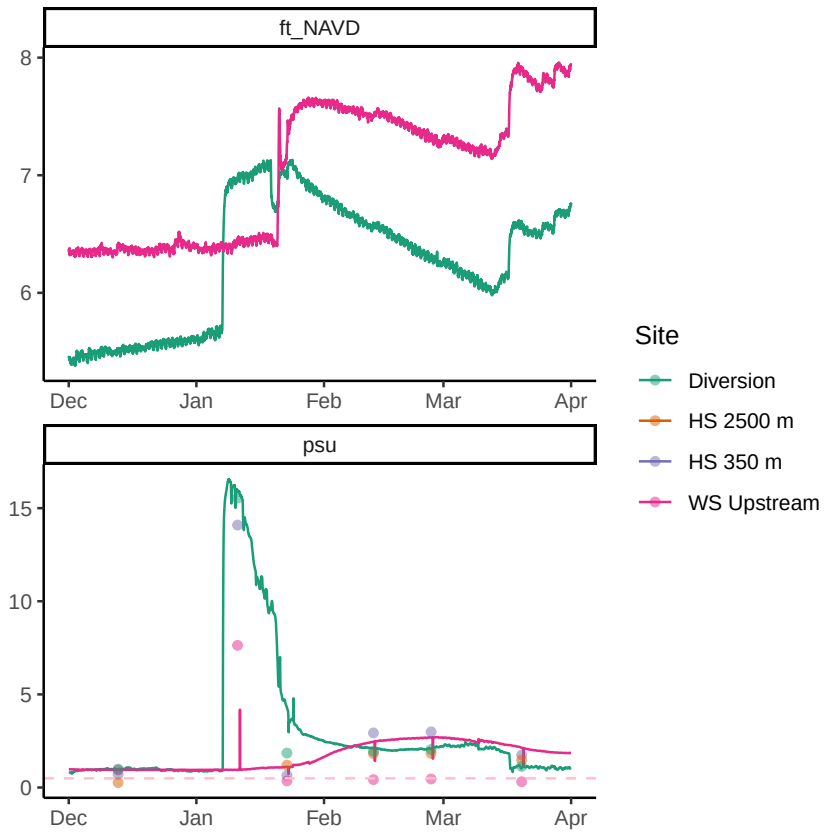

Figure 3.C.4. Stage and salinity from logger and grab sample data at and above the diversion site, December 1, 2011 – April 1, 2012. (Top) Available stage measurements. (Bottom) Available logger salinity (solid lines), grab sample measurements (points), and salinity threshold for the Diversion site (dashed line). HS 350 m and HS 2500 m refer to grab sample sites located on the Harkins Slough 350 m and 2500 m upstream of the Harkins-Watsonville confluence (above the diversion point), and show long-lasting elevated post-SWI salinity within upstream segments of the Harkins Slough. Water managers attribute mismatch in WS upstream site logger and grab sample observations to sensor/sample placement within vertically stratified water that can occur at these upstream sites.

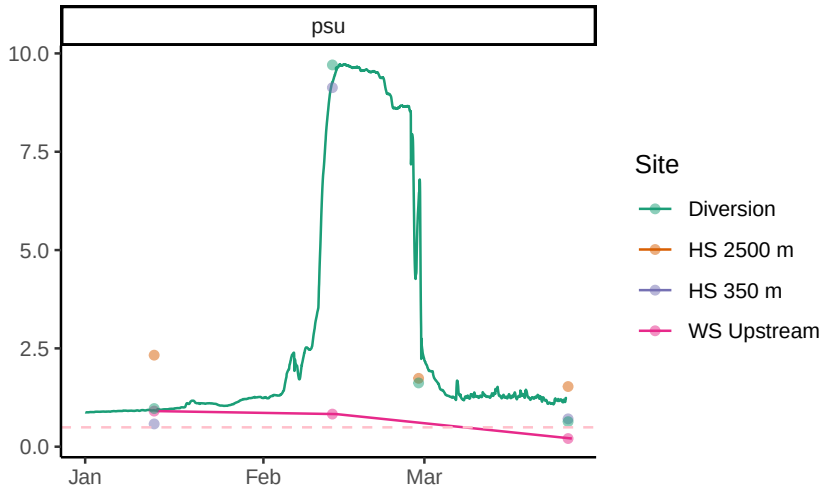

Figure 3.C.5. Salinity from logger and grab sample data at and above the diversion site, January 1, 2014 – April 1, 2014. Available logger salinity (solid lines), grab sample measurements (points), and salinity threshold for the Diversion site (dashed line). HS 350 m and 2500 m refer to grab sample sites located on the Harkins Slough 350 m and 2500 m upstream of the Harkins-Watsonville confluence (above the diversion point), and show no elevated post-SWI salinity within upstream segments of the Harkins and Watsonville Sloughs.

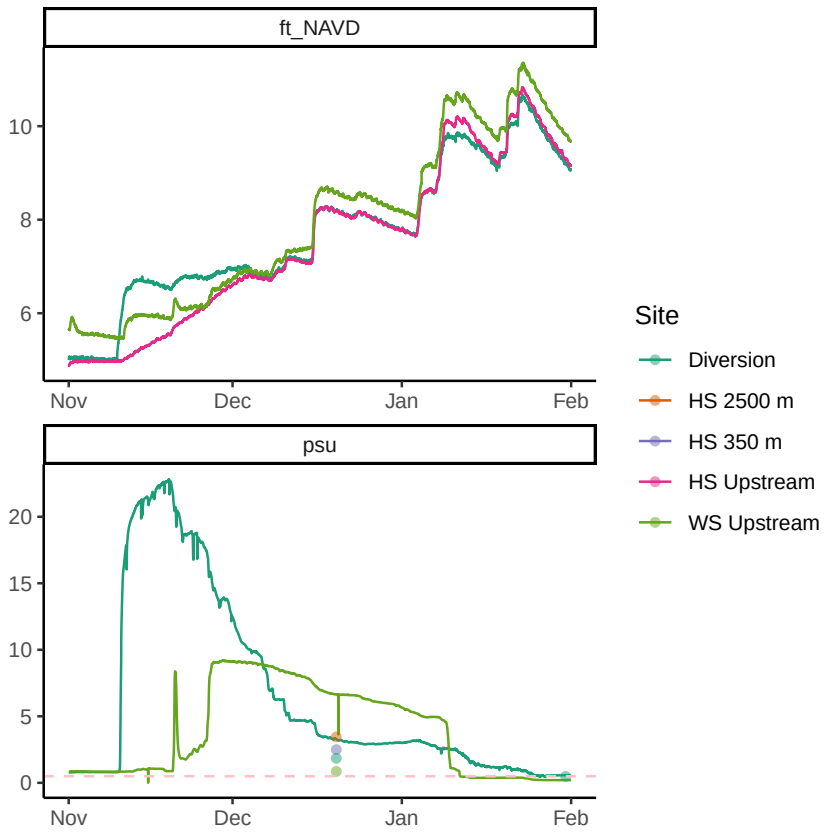

Figure 3.C.6. Stage and salinity from logger and grab sample data at and above the diversion site, November 1, 2016 – February 1, 2017. (Top) Available stage measurements. (Bottom) Available logger salinity (solid lines), grab sample measurements (points), and salinity threshold for the Diversion site (dashed line). HS 350 m and 2500 m refer to grab sample sites located on the Harkins Slough 350 m and 2500 m upstream of the Harkins-Watsonville confluence (above the diversion point), and show elevated post-SWI salinity within upstream segments of the Harkins and Watsonville Sloughs through February 2017. Water managers attribute mismatch in WS upstream site logger and grab sample observations to sensor/sample placement within vertically stratified water that can occur at these upstream sites.

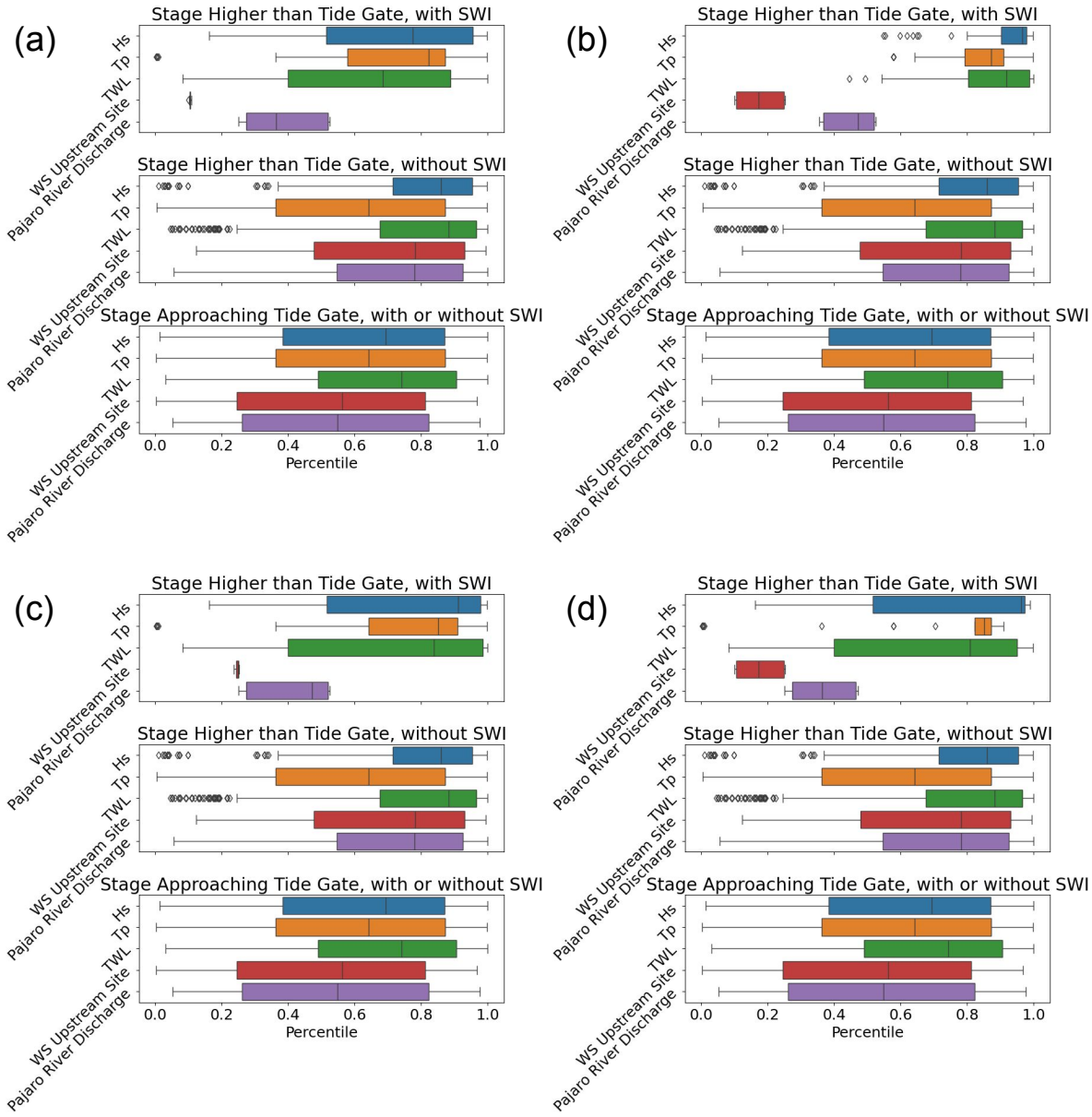

Figure 3.C.7. Leave-one-out sensitivity analysis of event sampling for the SWI event typology analysis. Calculations replicate those described in the Methods section for the SWI Event Typology analysis, while leaving out (a) salinity event 1 on 1/6/2012, (b) salinity event 2 on 2/7/2014, (c) salinity event 3 on 11/5/2016, and (d) salinity event 4 on 1/17/2018. Median percentiles for the variables remain relatively stable despite event selection.

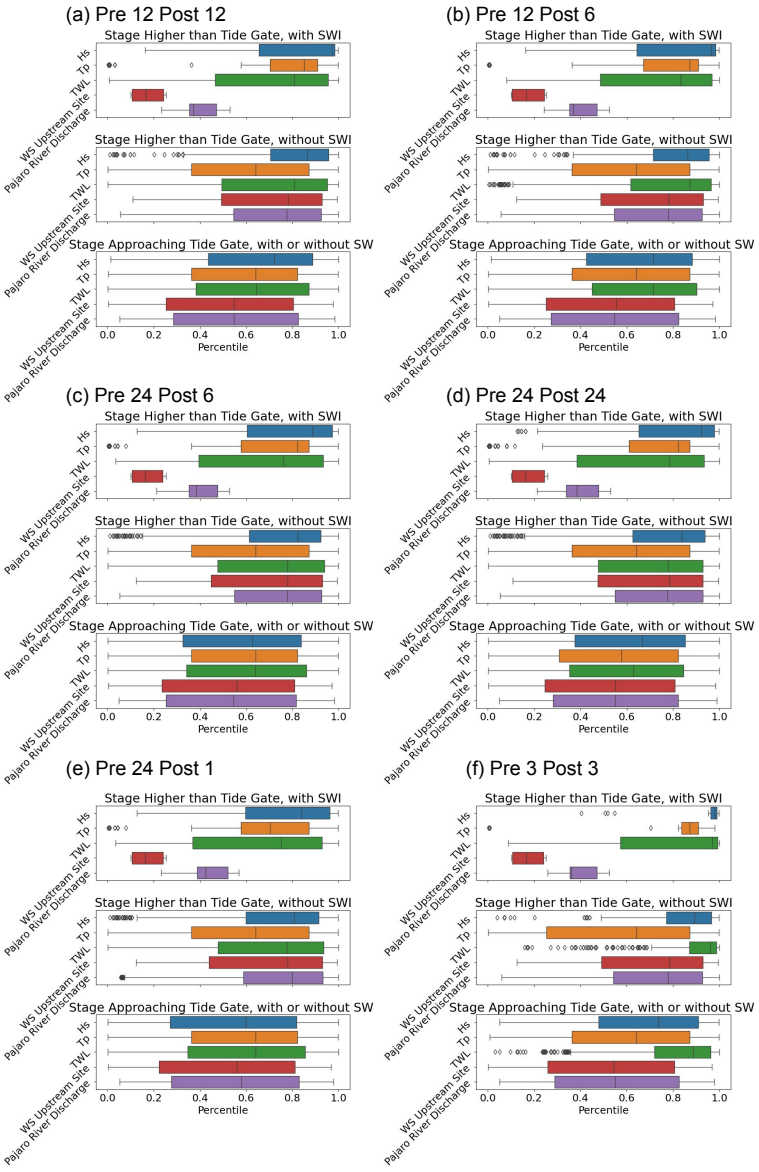

Figure 3.C.8. Timescale sensitivity analysis of event time duration for the SWI event typology analysis. Calculations replicate those described in the Methods section for the SWI Event Typology analysis, but with different windows of time prior to and immediately following the tide gate vent overtopping onset as labelled on panel titles (a)-(f).

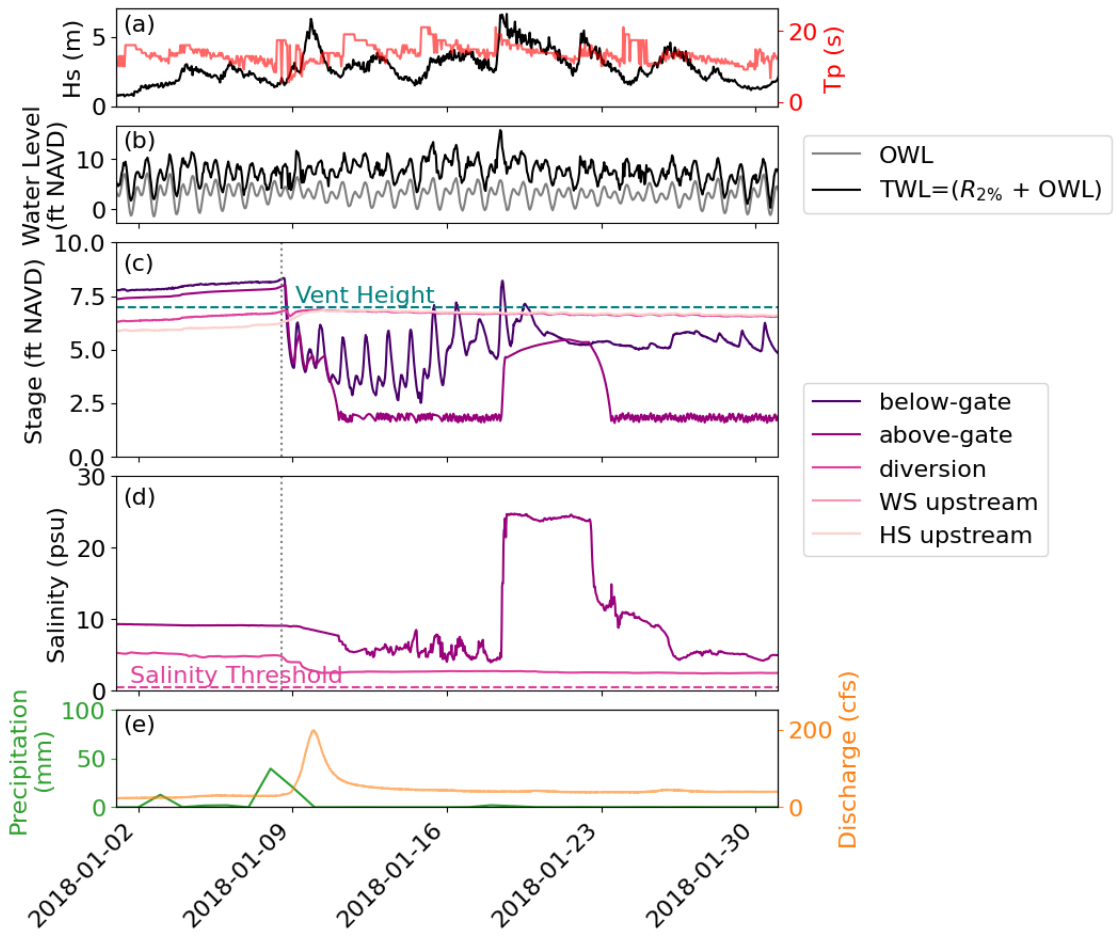

Figure 3.C.9. Coastal to inland stage and salinity connectivity under wet/extreme conditions over 1 month (January 1, 2018-January 31 2018). (a) Significant wave height (Hs) and peak period (Tp); (b) offshore water level (OWL and total water level (TWL); (c) stage at the below-gate, above-gate, diversion, and upstream stations, with the elevation of the tide gate vent (dashed turquoise line); (d) salinity at the below-gate, diversion, and upstream stations with the salinity threshold for diversion (dashed line); (e) precipitation and Pajaro River discharge. Note that the estuary mouth was closed at the start of this record. The vertical gray dotted line indicates when the mouth was manually breached by the County of Santa Cruz on January 8, 2018 (no time listed).

Chapter 4

Assessing future SWI risk using projections of TWL and precipitation

4.1 Abstract

In the coastal watershed of the Pajaro Valley, CA, USA, saltwater intrusion (SWI) has historically threatened freshwater supplies and an established managed aquifer recharge program. SWI risk is expected to increase under climate change scenarios, however the magnitude of this increase has not been previously explored. In this study, we utilized projections of sea level and precipitation from the Coupled Model Intercomparison Project 5 (CMIP5) general circulation models (GCMs) under the 'business-as-usual' climate change scenario (RCP 8.5) combined with simulations from a stochastic wave emulator to explore the joint distributions of variables that drive SWI: high oceanic total water level (TWL) and precipitation representative of low upstream flow conditions. We established thresholds of TWL and precipitation that indicate SWI risk along the Monterey Bay coast, and estimated the percentage of time in which SWI risk would occur for historical (1950-2005), early century (2006-2050), and late century (2051-2100) periods. Although there was variability in the frequency of SWI risk amongst the models for each time period, there was a clear upward trend with time in this percentage, primarily driven by the sea level rise component of TWL. Uncertainty in SWI risk frequency was driven by both precipitation variation across GCMs and variation across wave simulations. Although this study is

inherently limited due to uncertainty in climate change projections, it offers a framework in which future projections of SWI risk can be studied in the Pajaro Valley and other coastal watersheds.

4.2 Introduction

Saltwater intrusion (SWI) in coastal watersheds is a threat to coastal populations and industries. Coastal regions are expected to house more than one billion people by the end of the century (Hauer et al., 2020). SWI is a coastal hazard that this population is anticipated to face given that it limits the usability of freshwater supplies .

SWI driven by sea level rise is likely to affect surface freshwater habitats and drinking water supplies. Several modelling studies have identified that under sea level rise scenarios, water within tributaries of the Chesapeake Bay (USA), the Yangtze River (China) and the Rhine River (Europe), will become undrinkable for extended periods of time (Rice et al., 2012; Chen et al., 2015; Brink van den et al., 2019). In the Yangtze River Estuary, for example, four reservoirs, which provide water for 50 million people, will have undrinkable water over 7 times more often than current conditions if sea levels rise by 2 m (Chen et al., 2015). SWI in groundwater aquifers has also been well documented (Jasechko et al., 2020; Sawyer et al., 2016; Houben, Post, 2017), and is expected to increase around the globe due to sea level rise and increases in groundwater pumping (Ferguson, Gleeson, 2012; Jasechko et al., 2020; Loáiciga et al., 2012). Whether SWI affects a region's groundwaters or surface waters, SWI has been identified as a serious concern for coastal water managers and planners (Michael et al., 2017).

At our study site, the Pajaro Valley in Monterey County, CA, USA, SWI affects both surface water (Ch.3) and groundwater supplies (Barlow, Reichard, 2010; Carollo, 2014; Pajaro Valley Water Management Agency, Montgomery & Associates, 2022). While surface SWI has been less well documented in the Pajaro Valley, as elsewhere, SWI in the Pajaro

Valley can have far-reaching impacts on freshwater supplies. The movement of oceanic water upstream through the Pajaro Lagoon and into the Harkins-Watsonville slough has greatly diminished the local water managers' ability to divert freshwater from the slough system. SWI has impeded the region's progress towards groundwater sustainability by negatively impacting managed aquifer recharge programs that rely on freshwater withdrawals from coastal sloughs. Nevertheless, water planning and infrastructure investments have been made and more are required despite uncertain climate change outcomes. Thus, improved understanding of future change and SWI risk with climate change is needed to help adapt water sustainability programs in the Pajaro Valley and other regions.

Through previous work (Chapter 3), we identified that the coupling of oceanic total water level (TWL), which is a combination of sea level and wave runup, with low upstream flow conditions drive SWI in the surface waters of the Pajaro Valley. These drivers are expected to be affected by climate change within the coming century. California's Fourth Climate Change Assessment for the Central Coast, where the Pajaro Valley is located, reports heightened variability in precipitation and drought risk, and an acceleration of sea level rise (SLR) in this time frame (Langridge, 2018). These environmental changes will likely influence saltwater intrusion in the Pajaro Lagoon as well as freshwater (groundwater and surface water) availability in the Pajaro Basin. This presents a challenge to regional water managers as they assess and adapt water management strategies under a changing climate.

To assess changes in oceanic and hydrologic variables under climate change scenarios, studies frequently rely on projections from GCMs provided by CMIP. These models, which are frequently used in combination with hydrologic models, have been used to assess climate change driven hazards in coastal regions, such as flooding (Bai et al., 2019; Try et al., 2022), drought (Basharin et al., 2016), and sea level rise (Hermans et al., 2021). While GCMs have been used to understand coastal freshwater SWI, particularly in large delta systems (Bellafiore et al., 2021; Anh et al., 2018; Eslami et al., 2021), GCM projections

have more frequently been applied in coastal flooding contexts (Bai et al., 2019; Try et al., 2022; Xu et al., 2023).

The co-occurrence of high oceanic TWL and low upstream freshwater flow, which indicates SWI risk (Ch.3), is analogous to the more often studied co-occurrence of high TWL and high upstream flow that typifies compound coastal flooding conditions (Lucey, Gallien, 2022; Ward et al., 2018; Xu et al., 2023). Within that analogous literature, future projections of compound coastal flooding suggest an increase in this phenomenon, mainly due to sea level rise, under the 'business-as-usual' (RCP 8.5) climate change scenario (Bevacqua et al., 2019). However, even under a more conservative scenario (RCP 4.5) coastal flooding is expected to increase across the US (Bates et al., 2021). These studies focus on the confluence of high TWL and inland flow conditions driven by high precipitation and river discharge. Alternatively, SWI in the Pajaro Valley, and other similar coastal regions (Tian, 2019), is reliant on the confluence of high TWL and low inland flow conditions. The co-occurrence of these drivers has received little to no attention in climate change studies.

The Pajaro Valley offers a unique study site wherein we build on understanding of the joint drivers of SWI risk (Ch.3) to assess change in the occurrence of those joint drivers in the future. In this study, we assess changes in the frequency at which SWI risk conditions occur in the next century, relative to the historical observational period and the modeled past century, using sea level and precipitation projections from CMIP5 GCMs combined with a stochastic wave emulator. In section 4.2.1, we describe the types of data used in this study, including observed data, CMIP5 GCMs, and simulated wave time series. In section 4.3, we establish thresholds in which we may expect SWI to occur at our study site, compare observed data to modelled and simulated data, and explore the joint distributions of TWL and precipitation-proxied inland flow conditions for historical and projected time periods. Next, in section 4.4, we discuss the limitations and applications of our novel study, and finally, we discuss conclusions in section 4.5.

4.2.1 Data

In order to expand our findings from chapter 3 into historical and projected periods, we developed analogous total water level (TWL) and inland flow condition time series in which we could explore the joint occurrence of high TWL and low flow conditions that have been documented to coincide with SWI events. We evaluated the frequency with which these conditions occurred for historical (1950-2005), observed (2011-2020), early century (2006-2050), and late century (2051-2100) periods at our study site. We utilized a wide range of datasets, including observed sea level, wave height and period, discharge, and precipitation (See Ch.3 for details on these datasets); downscaled regional sea level rise and precipitation estimates from 8 Coupled Model Intercomparison Project Phase 5 (CMIP5) general circulation models (GCMs); and wave height and period from 100 TESLA wave simulations. The details of these datasets are discussed in the following subsections.

Observations

We utilized the observations of ocean water level (OWL), wave height and period, beach slope, precipitation, and river discharge, as outlined in Chapter 3, Section 4.1 for the observed time period, 10/2011-05/2020. We then split the data into wet and dry periods by similarly defining the yearly wet periods as the months of November through the following May, which corresponds to the time periods in which the local water management agency, Pajaro Valley Water Management Agency (PV Water) is permitted to divert freshwater from the Harkins-Watsonville Slough. For this study, we focused solely on wet periods during which SWI can disrupt the diversion of freshwater from the sloughs.

CMIP5 Models

Modelled sea level and precipitation time series of the historical, early century, and late century periods were available at regional scales from 8 CMIP5 GCMs: ACCESS1-

0, CanESM2, CMCC-CMS, CNRM-CM5, GFDL-CM3, HadGEM2-CC, HadGEM2-ES, and MIROC5. We used the hourly downscaled regional sea level at the location of the NOAA tide gauge in Monterey Bay (station 9413450). These data are publicly available (https://albers.cnr.berkeley.edu/data/scripps/hourly_sea_level/). The GCMs output values of secular sea level rise, tides, and weather/ocean components for each site, but for our purposes we will use the sum of these 3 contributors to generate oceanic water level (OWL, or the equivalent of TWL minus the wave component – see below).

We also utilized daily precipitation values from LOCA-downscaled (Pierce et al., 2014) CMIP5 meteorology at the grid cell that overlapped with the location of a weather station used previously to establish SWI drivers in the Pajaro Valley (Ch.3), CIMIS station 129. LOCA CMIP5 data are publicly available (Livneh et al., 2023).

CMIP5 GCM runs for sea level and precipitation were available for historical (1950-2005) and projected (2006-2100) periods for the RCP 4.5 and 8.5 scenarios. For this study, we focused on the most extreme scenarios: RCP 8.5 and the 99.9th percentile for sea level rise projections. We then further split the projected time series into early century (2006-2050) and late century (2051-2100) periods for analysis.

TESLA wave simulations

Simulated time series of wave height and period were generated using TESLA, a wave emulator that generates wave time series based on historical statistics following the methods of Anderson et al. (2018, 2019) and Cagigal et al. (2020). The historical statistics were generated using significant wave height, peak period, and wave direction time series from 06/1987-12/2021 from the NDBC buoy described in Chapter 3 section 4.1. We assumed that the wave climate will not change extensively throughout the rest of the century, an assumption that we confirmed to be valid by comparing the distributions of the MIROC5 modelled wave component time series for the historical, early century, and late century periods. There was little change across these distributions. Similarly, Erikson

et al. (2016) project that mean significant wave height and peak period will have little to no change in the early and late century periods along the West Coast of the US. Thus, we generated all wave simulations based on statistics from the 1987-2021 NDBC wave buoy dataset. The wave emulator generated daily wave parameters (significant wave height, peak period, and incident direction) by establishing 25 daily weather types (DWTs) based on sea level pressure fields and gradients in the Pacific Basin. Then a synthetic sequence of DWTs were generated using an autoregressive logistic regression, following Anderson et al. (2019) and Guanche et al. (2014). Synoptic states were established and defined by sets of consecutive days in which the DWT was constant, spanning 1 to 5 days. Then Gaussian copula generated from historical distributions were used to generate significant wave height, peak period, and incident direction for each synoptic state (Cagigal et al., 2020; Ben Alaya et al., 2014). To explore the most extreme events, we used the same wave parameter values for all the days within the same synoptic state. We generated 100 daily 150-year wave simulations (representing the date range of 01/01/1950-12/31/2100) at the location of the NDBC buoy from which historical data was used. These statistical sets of wave simulations are not dynamically coupled to the climate projections' atmospheric states. However, since SWI events rely on the coupling of high wave events and low inland flow, we utilized the 100 TESLA simulations to better explore the timing of these combined events and to offer multiple realities under which the conditions of SWI may or may not be satisfied in a given day.

Total water level (TWL)

TWL was calculated as detailed in Chapter 3 section 4.1. For the OWL component we used the observed OWL from the NOAA tide gauge in Monterey or the modelled OWL total from the CMIP5 GCMs. The same average beach slope value of 0.033 m/m from Chapter 3 section 4.1 was used as an input to the 2% runup exceedance value parameterization from Stockdon et al. (2006). For the significant wave height and peak

period inputs we used either observed wave parameters from the NDBC buoy or simulated wave parameters from the 100 TESLA runs, as described above. TWL was then calculated at the daily scale for observed data by adding the hourly observed OWL to the hourly $R_{2\%}$ calculated from observed wave parameters and using the maximum hourly value per day. For the modeled data, we calculated daily TWL by taking the maximum hourly OWL value per day for each CMIP5 GCM and adding $R_{2\%}$ calculated from the daily resolution TESLA simulations. Thus we have 100 time series of daily TWL for each model for all time periods.

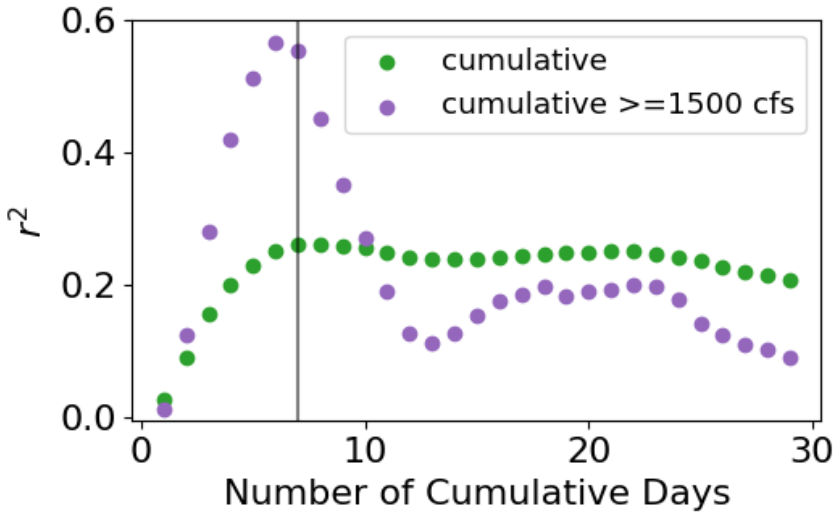

Figure 4.1. R^2 correlation coefficient values for cumulative precipitation over 1-30 day timescales and river discharge (green) and for cumulative precipitation over 1-30 day timescales for days in which mean daily discharge is greater than or equal to 1500 cfs and river discharge (purple). 7 days is marked by the vertical gray line.

Upstream flow conditions: Precipitation

Downscaled freshwater discharge specific to our study region was not available at the time of this study, so we used cumulative precipitation (antecedent to TWL) to represent inland flow conditions. First, we evaluated the relationship between observed

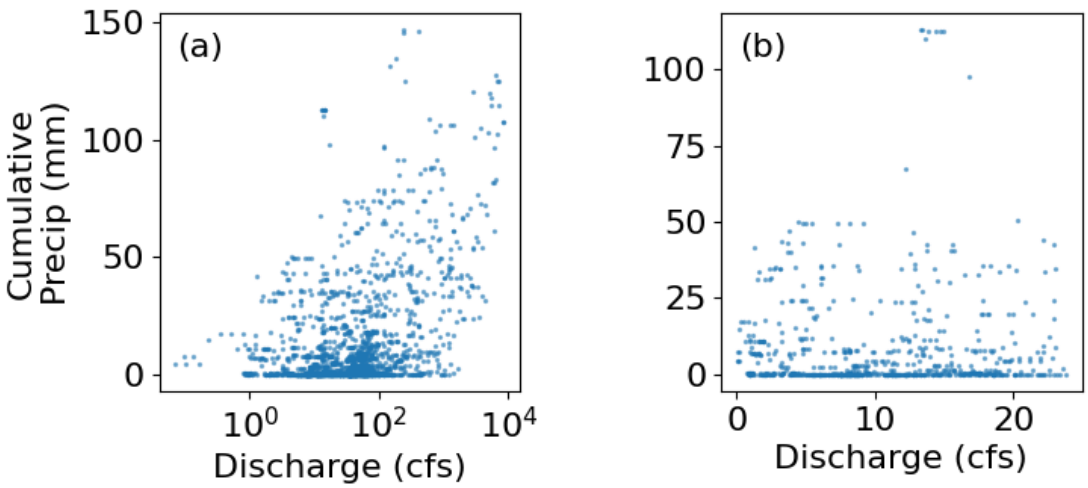

Figure 4.2. Scatter plot of cumulative 7-day precipitation (mm) versus mean daily discharge (cfs) for (a) the full study period and (b) all times when discharge is below the 37th percentile (24 cfs). Note that the scale of the x-axis in panel (a) is logarithmic.

discharge and cumulative precipitation to determine an appropriate formulation of a precipitation variable for this analysis. We calculated the daily mean value of 15-min river discharge from the Pajaro River (see chapter 3 section 4.1 for details on dataset) and calculated the daily mean discharge's correlation with cumulative precipitation over a range of the preceding 1-30 days, as shown in Figure 4.1. Daily discharge and cumulative precipitation is most correlated for high values of discharge (>= 1500 cfs), so we calculated the correlation both for the full dataset (all levels of discharge) and separately for times in which discharge was greater than 1500 cfs. The greatest correlation values are for cumulative precipitation over the preceding 7 days for all data and cumulative precipitation over the preceding 6 days for data above discharge values of 1500 cfs. For simplicity, we use the cumulative precipitation for the preceding 7 days or 1 week as our proxy for upstream freshwater discharge.

We compare the 7-day cumulative precipitation to the mean daily discharge in Figure 4.2. Although visually there is lower correlation between precipitation values

associated with discharge values under 1500 cfs, low values of precipitation generally represent low values of discharge that satisfy the threshold-based conditions for SWI. Thus we suggest that precipitation is a suitable proxy for river discharge in the following analyses.

4.3 Methods and Results

4.3.1 SWI Thresholds

Using observational data in Chapter 3, we established a range of percentiles of significant wave height (H_s), peak wave period (T_p), total water level (TWL), river discharge, and upstream stage that occurred during saltwater intrusion (SWI) events in the ocean-connected Harkins-Watsonville Slough. To explore the prevalence of SWI events under future climate scenarios, we first defined periods of SWI risk as periods of time during which TWL exceeded, and upstream flow fell below, levels during which documented SWI events occurred, as discussed in chapter 3 section 5.4. SWI risk percentages refer to the percentage of days during the wet season (November-May) in which conditions for SWI risk are satisfied. To define these thresholds, we used the median of percentile values of 30-minute TWL (84th percentile, 2.7 m NAVD) and of 15-minute river discharge (37th percentile, 24 cfs) over the 12 hours that preceded and the 1 hour that followed a documented SWI event. These thresholds then represent conditions under which it is possible for SWI to occur in the freshwater slough during the wet season. To convert the river discharge threshold to a cumulative precipitation threshold, we take the median value of all 7-day cumulative precipitation that occurs when daily mean river discharge is at the 37th percentile or below, which results in a precipitation threshold of 9.5 mm. Thus, we suggest that if daily maximum TWL is above 2.7 m NAVD and the coincident 7 day cumulative precipitation is below 9.5 mm, then the conditions for possible SWI are met.

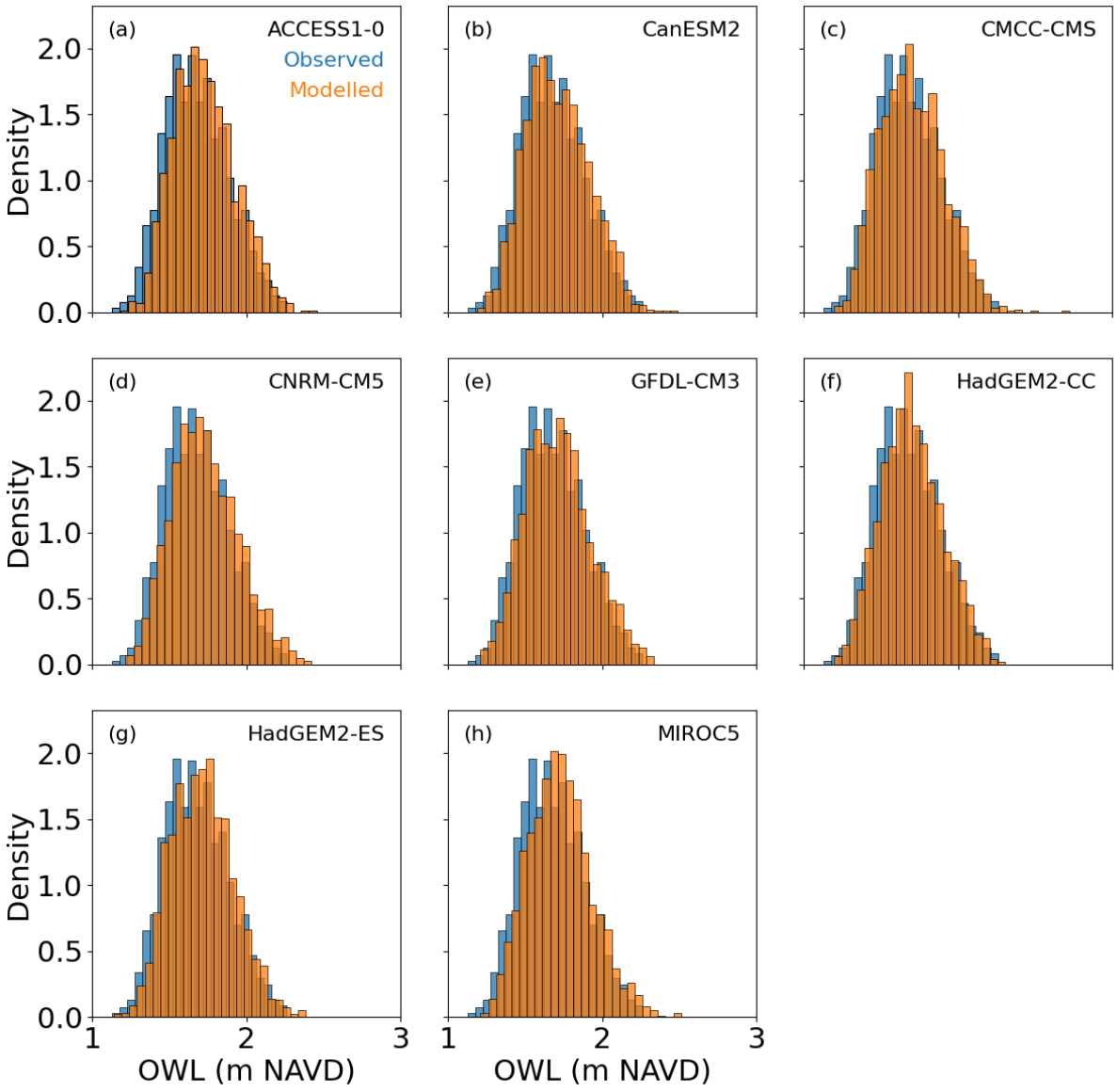

Figure 4.3. Distributions of observed OWL (blue) and modelled OWLs (orange) from the 8 CMIP5 GCMs (panels a-h) for the observed period (2011-2020).

4.3.2 Observed vs. Modelled data comparisons

TWL

TWL is comprised of an ocean water level component (OWL) and a wave runup component ($R_{2\%}$). To validate the accuracy of modeled TWL, we compared the observed and modelled components (OWL and waves separately) as well as the combined TWL

within the observed period (2011-2020). Thus OWL is compared between observations and CMIP5 modeled values, and waves are compared between observations and TESLA wave simulations. Finally TWL is compared between observations (observed OWL + $R_{2\%}$ from observed wave parameters) and modelled (CMIP5 OWL + $R_{2\%}$ from TESLA wave parameters).

For modelling historical and projected periods of OWL, we used the output of 8 CMIP5 GCMs, as described in Section 4.2.1. We compared the observed OWL from our observed period (2011-2020) to the modelled OWL in Figure 4.3. The modelled data had similar distributions across GCMs, but all were biased slightly higher than the observed OWL distributions: GCM median OWL exceeded observed median OWL by a mean of 0.05 m. Therefore, the modelled OWL data may contribute to slight over-estimations of TWL.

For the wave component of TWL, we used simulated wave data from the TESLA emulator and compared those to the observed wave data from the NDBC buoy (Figure 4.4). The distributions of H_s, T_p, and wave direction from TESLA during the observed period were similar to the observed datasets, however the distributions from TESLA were smoother in shape across ranges of H_s, T_p, and wave direction, because TESLA wave components are generated from prescribed statistical distributions. The TESLA H_s distribution had a heavier upper tail, with more waves above 2.5 m. T_p, on the other hand, was biased slightly lower (median of 12.9 s for TESLA vs. 13.8 s for the observed values). Although wave direction was not used to calculate $R_{2\%}$, we included it as further validation of the TESLA simulation. The distribution of wave direction from TESLA also resembled the observed data, but had more weight in the lower tail (wave angles below 250 degrees). For $R_{2\%}$, there are few differences between the distributions of observed and TESLA-simulated data, with slightly more density in values over 2 m for the observed dataset. Therefore, the TESLA-simulated waves may bias the TWL slightly lower than true values. The empirical cumulative distribution functions (ECDFs) show

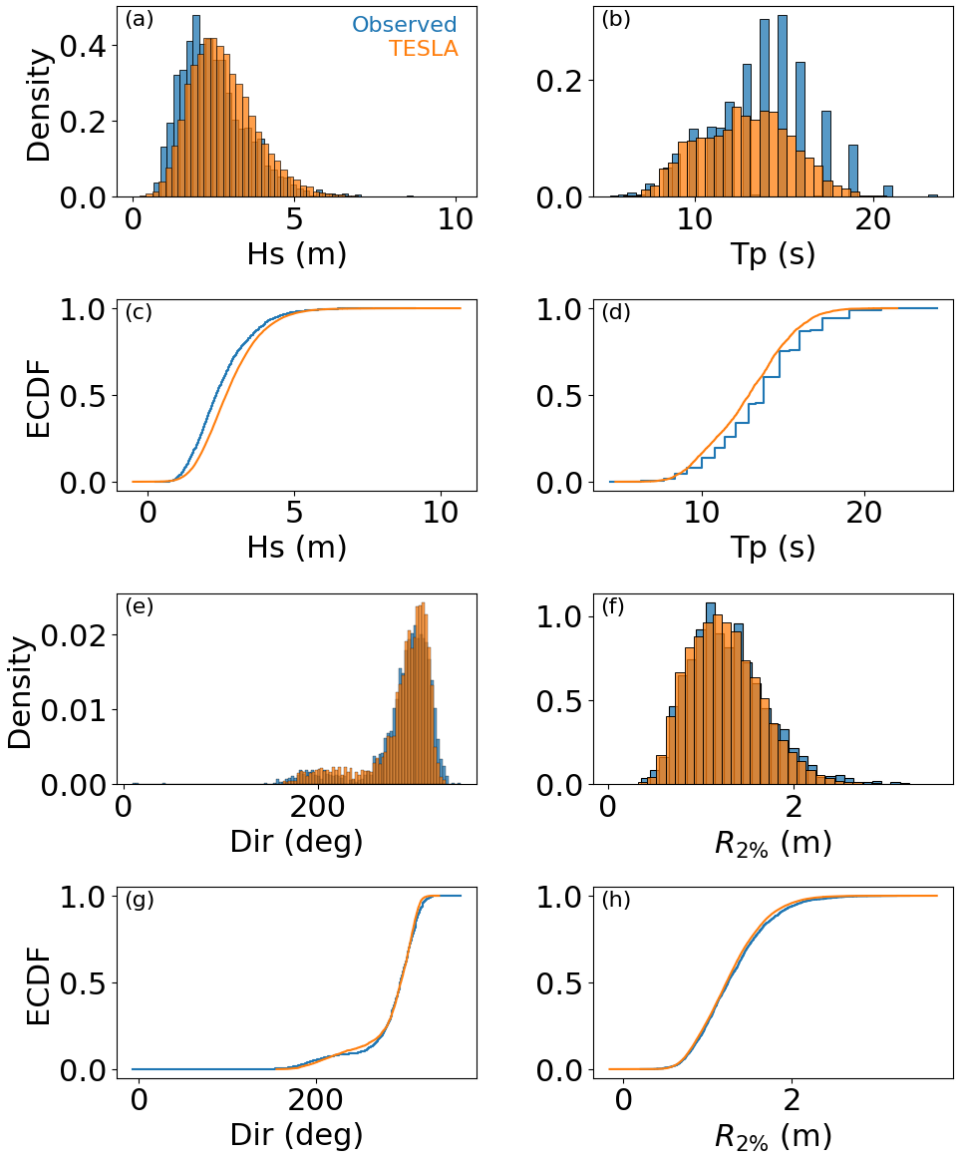

Figure 4.4. Distributions of daily (a) significant wave height, H_s, (b) peak period, T_p, (e) wave direction, and (f) wave runup, $R_{2\%}$, and empirical cumulative distribution functions for (c) H_s, (d) T_p, (g) wave direction, and (h) $R_{2\%}$ for observed (blue) and TESLA-simulated (orange) datasets for the observed period (2011-2020).

some differences between the observed and TESLA-simulated H_s and T_p (Figure 4.4(c) and (d)), however, these differences do not materialize in large differences between observed and TESLA-simulated $R_{2\%}$. Here we do not conduct more formal comparisons, like the Kolmogorov-Smirnov test, due to their sensitivity to sample sizes.

We compared the distributions of TWL generated from observed OWL and observed

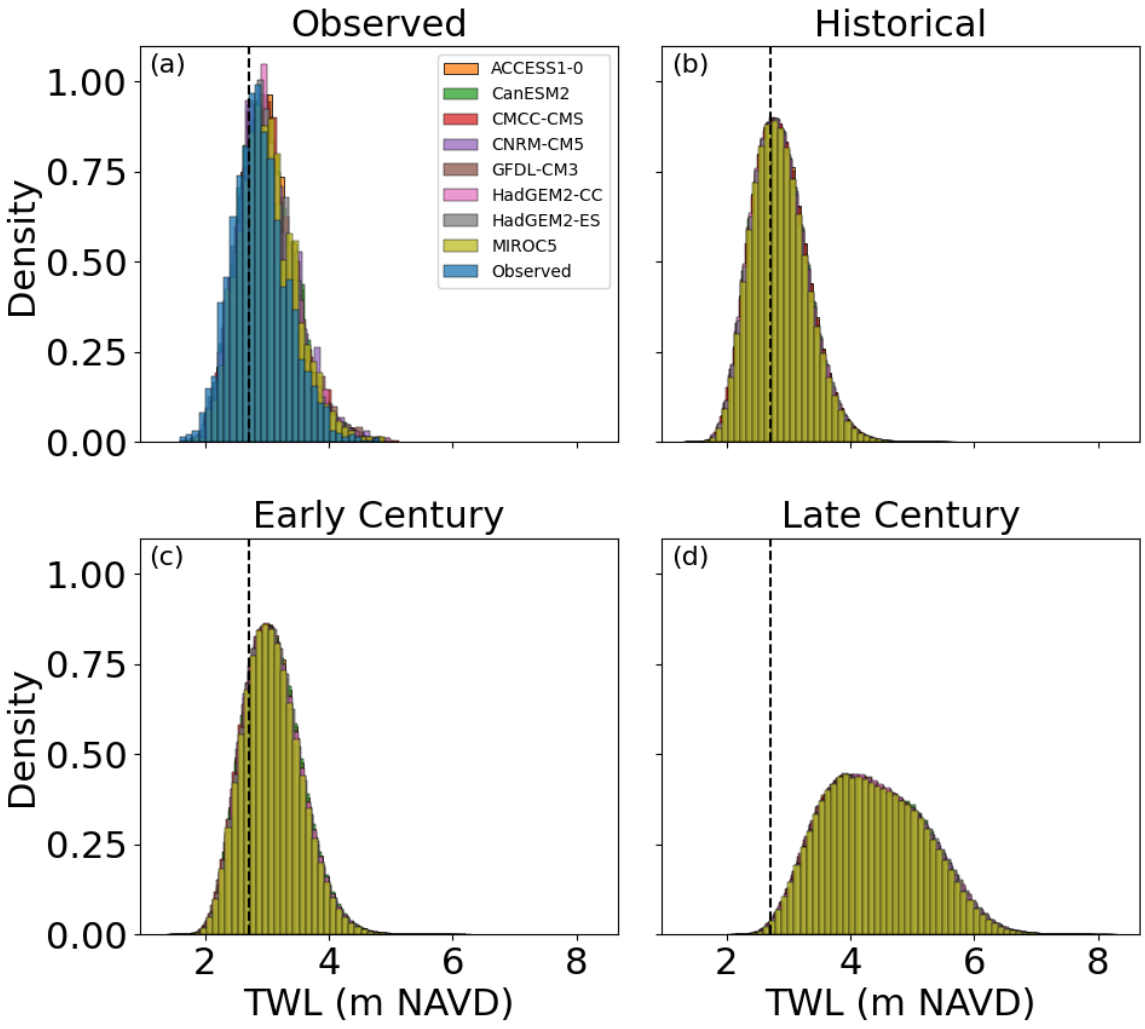

Figure 4.5. Distributions of TWL for the (a) observed period, using each CMIP5 GCM's OWL with $R_{2\%}$ calculated from observed wave parameters, and (b) historical, (c) early century, and (d) end century time periods using each CMIP5 GCM's OWL (colors) with $R_{2\%}$ calculated from the 100 simulated wave time series from TESLA (identical for all GCM TWLs). Dashed black line indicates the SWI risk threshold for TWL (2.7 m).

wave parameters to TWL distributions generated from CMIP5 GCM modelled OWL and observed wave parameters (Figure 4.5(a)). As stated previously, the slight bias towards higher values in the modelled CMIP5 GCM OWLs led to a similar bias in TWL values for the observed period. However, the distributions of observed TWL and all modelled TWL are fairly similar in shape. We also generated 100 time series of TWL per model for the

historical, early century, and late century periods by calculating $R_{2\%}$ for the 100 TESLA wave simulations and adding the resulting time series to the CMIP5 GCM modelled OWL time series. We then compared these distributions across time periods in Figure 4.5(b)-(d). The modelled TWL distributions had few differences from each other for all time periods. The historical and early century TWL distributions were similar in shape, however the distributions shifted towards higher values in the early century period. By the late century period, the distributions had a greater spread and the majority of the data shifted to values higher than the TWL threshold. Thus, the greatest change in TWL distribution will likely be seen during the late century, and we would expect this shift to increase the amount of time in which SWI may occur.

Precipitation

We compared the observed precipitation distributions with CMIP5 GCM modelled distributions for the observed period in figure 4.6 (a). The observed data had more weight in the lower tail (values under 10 mm of cumulative precipitation), while the modelled values had more weight in the upper tail (between 20 mm and 150 mm). The variability in precipitation distributions across models was greater than the variability seen in TWL across the same models. The CanESM2, CNRM-CM5, and HadGEM2-ES models produced more large precipitation events ($>$ 150 mm) than the other models for the observed period. This higher density of larger precipitation events was less distinct in the historical period (Figure 4.6 (b)), however it was prominent in the early century and late century time periods (Figure 4.6 (c) and (d)). We suggest that the decreased probability of lower precipitation events for these models may lead to under-estimates of amount of time in which SWI may occur for future scenarios.

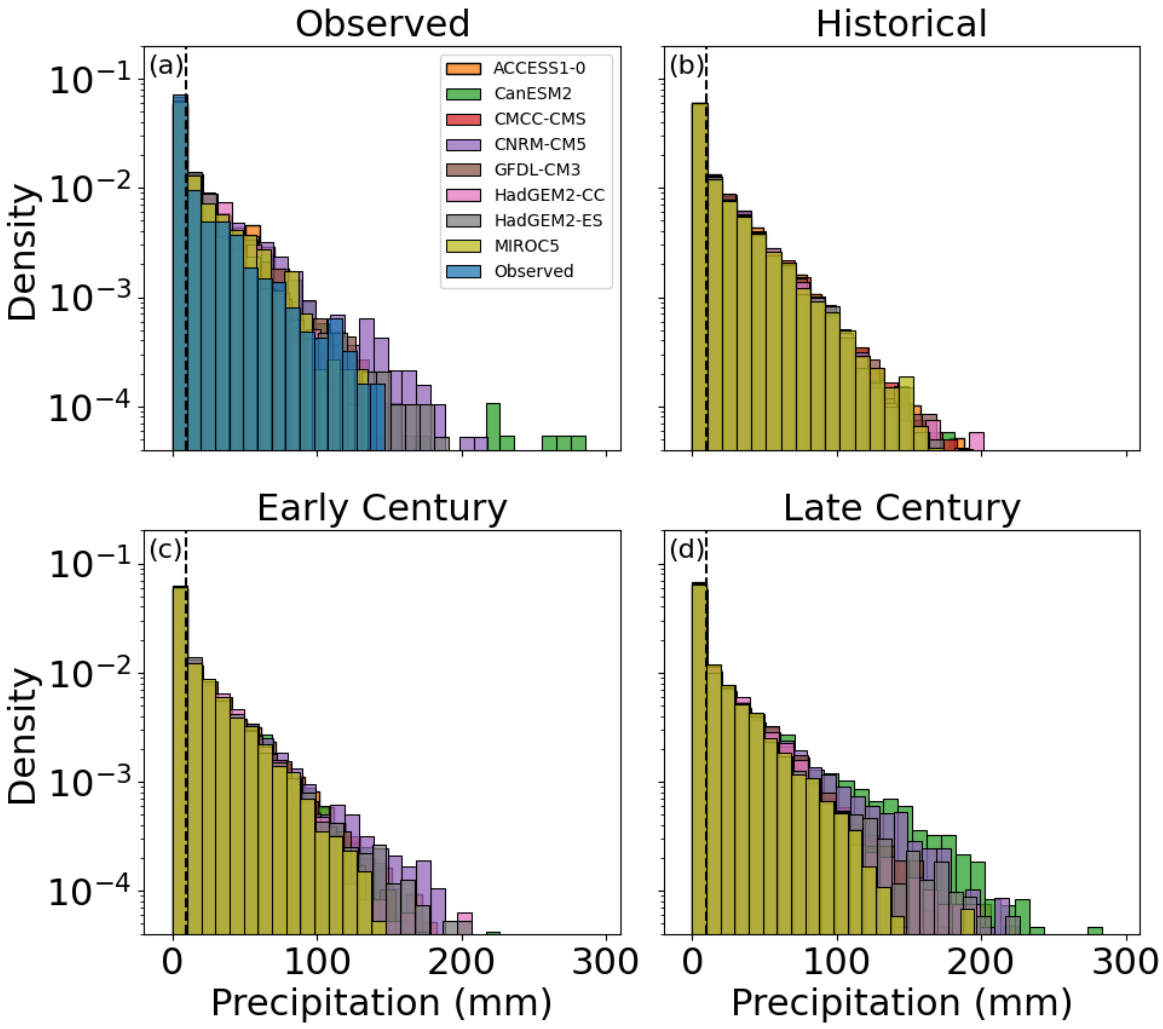

Figure 4.6. Distributions of precipitation for the (a) observed period, using observed 7 day cumulative precipitation and each CMIP5 GCM's modelled 7 day cumulative precipitation (colors), and similarly for (b) historical, (c) early century, and (d) end century time periods. The density axis is on a logarithmic scale.

4.3.3 Joint distributions of TWL and precipitation for historical, early century, and late century periods

Finally, we explored the joint distributions of TWL and precipitation to better understand how the frequency of SWI risk conditions may change under future climate scenarios. To begin, we looked at the observed period and compared the distributions of observed data to the combination of CMIP5 GCM modelled data and TESLA simulated

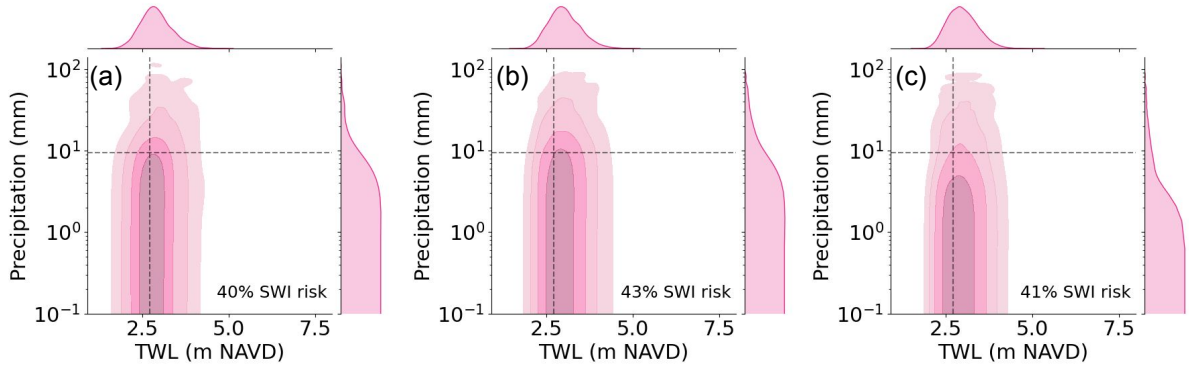

Figure 4.7. Joint distributions of TWL and precipitation for (a) observed TWL and precipitation, (b) TWL comprised of MIROC5 OWL and observed wave components and MIROC5 precipitation, and (c) TWL comprised of MIROC5 OWL and the 100 TESLA simulated wave components and MIROC5 precipitation. Dashed gray lines indicate the TWL and precipitation thresholds and outline the lower-right quadrant space that represents SWI risk conditions, and percentages listed on the figure indicate the percentage of time in which those SWI risk conditions occur for each dataset.

data. Using observed data within the observed period, the conditions for possible SWI were met 40% of the time (Figure 4.7(a)). The percentage of time within the SWI risk thresholds changed marginally to 43% when we used a GCM-modelled OWL, specifically MIROC5 as an example, with the observed wave components and the corresponding modelled MIROC5 precipitation (Figure 4.7(b)). For this MIROC5 example, the TWL distribution is shifted upwards due to the bias in modelled OWL, but the precipitation distribution is fairly similar across the different modelled and observed sources of precipitation data. We also compared the distributions of the 100 time series of TWL generated from the simulations of TESLA wave parameters combined with MIROC5 modelled OWL, and the MIROC5 modelled precipitation (Figure 4.7(c)). This also resulted in a similar estimate of SWI risk occurrence (41%). The similarities in percentages of time in which SWI may occur suggest that the CMIP5 GCM modelled OWL and precipitation, and the TESLA wave simulations are suitable for generating representative joint distributions of TWL and precipitation under future climate scenarios.

Using MIROC5 as an example, we compared the joint distributions of TWL

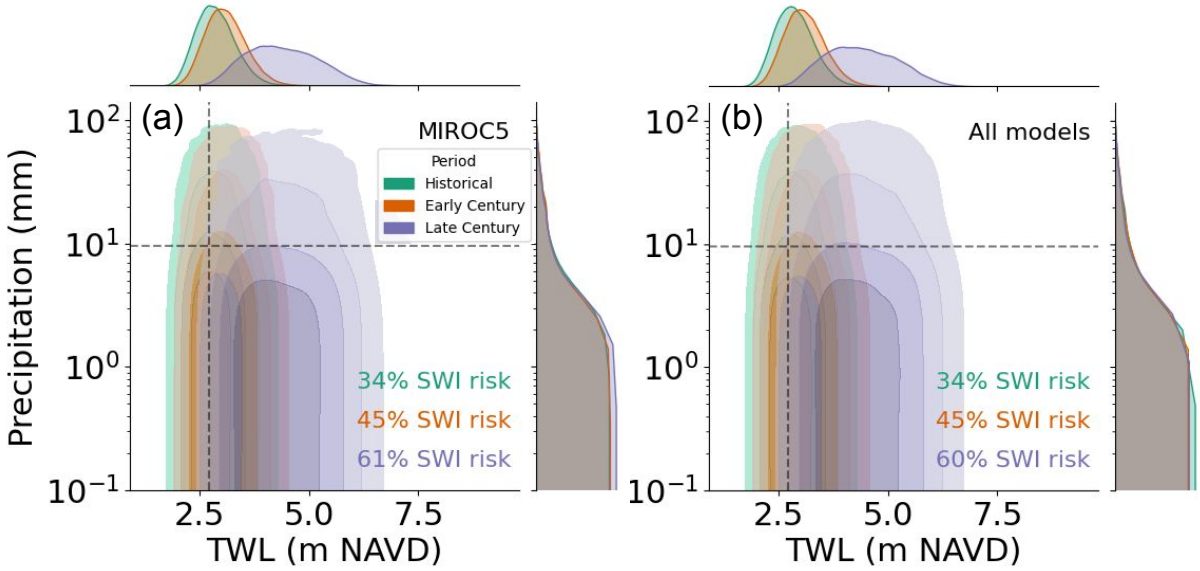

Figure 4.8. Joint distributions of TWL comprised of CMIP5 GCM modelled OWL and TESLA wave components and CMIP5 GCM modelled precipitation for (a) the MIROC5 model only for the historical (green), early century (orange), and late century (purple) periods, and for (b) all CMIP5 GCM models. Dashed gray lines indicate the TWL and precipitation thresholds and outline the lower-right quadrant space that represents SWI risk conditions, and percentages listed on the bottom right of the panels indicate the percentage of time in which those SWI risk conditions occur for the dataset.

and precipitation for the historical (1950-2005), early century (2006-2050), and late century (2051-2100) periods (Figure 4.8 (a)). Moderate increases in the frequency of lower precipitation events coupled with significant increases in the frequency of higher TWL correspond to increased SWI risk. Time spent within the joint distribution threshold of SWI risk (represented by the lower right quadrant of the figure) increased from 34% in the historical period to 45% in the early century period. The greatest change in this percentage was estimated between the early century and late century periods, in which the frequency of SWI risk increased by 16%, indicating that this system could be vulnerable to SWI 61% of the time. Similar joint distributions from all CMIP5 GCM models (Figure 4.8 (b)) demonstrate a similar shift with time. Slight variations between joint distributions from each of the CMIP5 GCMs were observed, but the overall pattern was similar (Supplementary Figure 4.A.1).

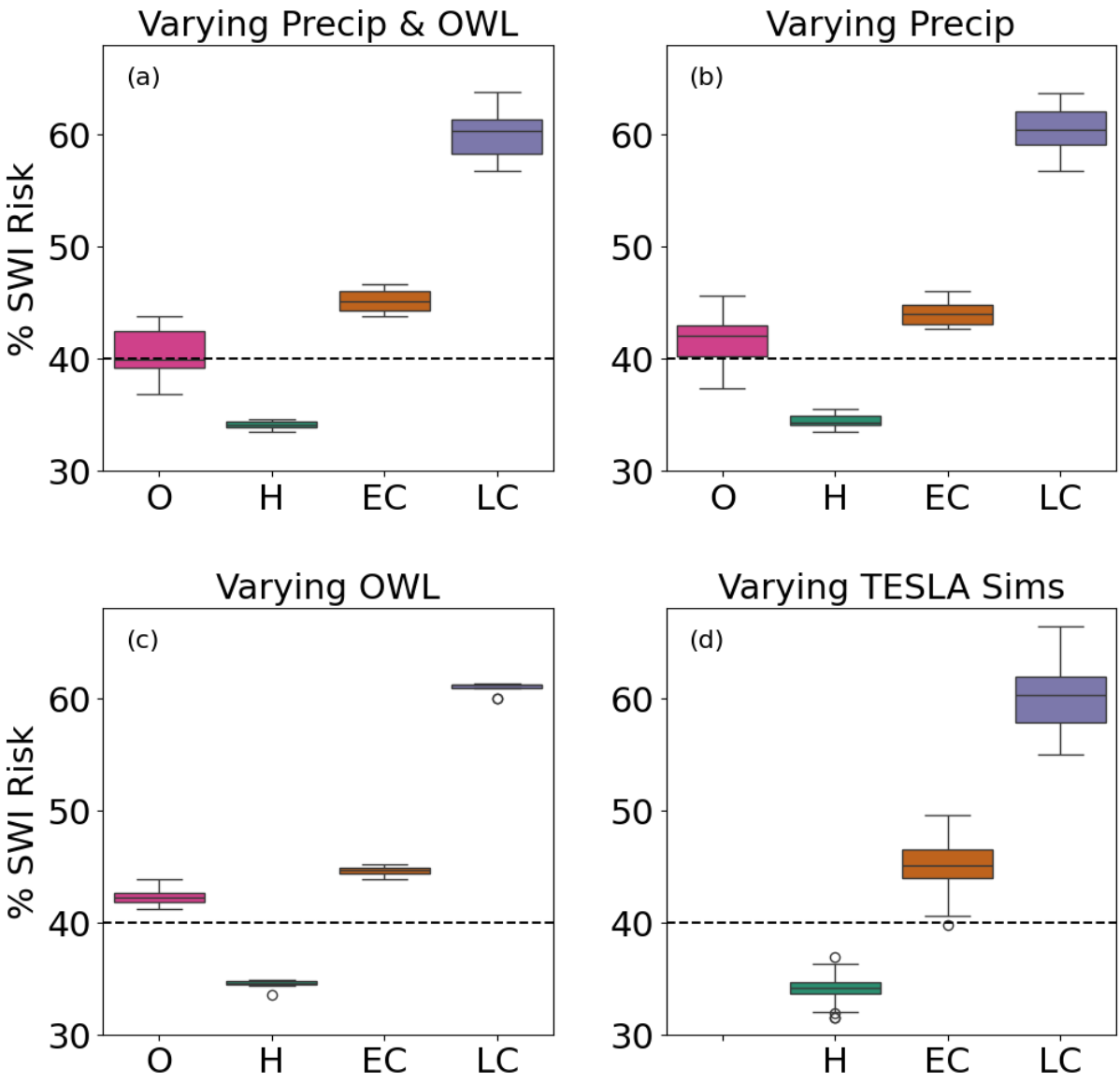

Figure 4.9. Boxplots showing the median and 1.5*IQR of the percentage of time in which SWI risk occurs for different datasets during the observed (O), historical (H), early century (EC), and late century (LC) periods. Boxplots are comprised of datasets in which we (a) vary precipitation and OWL (8 values per boxplot), (b) vary precipitation only (8 values per boxplot), (c) vary OWL only (8 values per boxplot), and (d) vary wave simulations (800 values per boxplot). The dashed black line on the panels indicate the % SWI risk for the observed period from the observed variables (4.7(a)).

In addition, we explore which component of TWL or precipitation contributed the most to the increase in SWI risk under future scenarios. Figure 4.9 shows the variability

in the % SWI risk amongst the CMIP5 GCMs for each time period. We first varied both precipitation and sea level (Figure 4.9(a)): TWL was composed of OWL from each of the 8 CMIP5 GCMs and the 100 simulations of wave parameters from TESLA, and precipitation was taken directly from each of the 8 (corresponding) CMIP5 GCMs. % SWI risk was calculated over all 100 TWL time series for each model (8 values per boxplot). We then varyied precipitation only (Figure 4.9(b)): TWL was composed of the MIROC5 OWL and one randomly chosen simulation of wave parameters from TESLA, and precipitation was taken from each of the 8 CMIP5 GCMs (8 values per boxplot). Then we varied sea level only (Figure 4.9(c)): TWL was composed of OWL from each of the 8 CMIP5 GCMs and the same randomly chosen simulation of wave parameters from TESLA, and precipitation was taken from MIROC5 (8 values per boxplot). Finally, we varied waves (Figure 4.9(d)): TWL was composed of OWL from each of the 8 CMIP5 GCMs and 100 unique simulations of TESLA wave parameters, and precipitation was taken directly from each of the (corresponding) 8 CMIP5 GCMs (800 values per boxplot). The boxplots in Figure 4.9(d) differ from Figure 4.9(a) because the SWI risk percent was calculated for each individual run of the TESLA simulation instead of calculating it for all 100 simulations as a whole to better assess the variability due to TESLA wave simulations. There was a clear upward trend in SWI risk frequency with progression through the historical, early century, and late century periods, with some variability within each time period. This variability is likely due to the variability in precipitation and TESLA wave simulations, as shown by the larger inter-quartile ranges in Figure 4.9(b), when precipitation was varied, and Figure 4.9(d), when TESLA simulations were varied, than in Figure 4.9(c) when OWL was varied. Although the observed period falls within the early century period, the early century as a whole demonstrates greater SWI risk occurrence, likely due to increased OWL as the century progressed. Thus we conclude that the wave simulations and modelled precipitation contribute to variability within and across time periods, but that the increasing trend in OWL is the main contributor to the increase in the frequency

of SWI risk over time.

4.4 Discussion

This study offers a novel look at the modeled future co-occurrence of high TWL and low precipitation conditions that are known to be conducive to SWI in the Pajaro Valley region and elsewhere. The use of CMIP5 GCMs allows us to assess realizations from different models run under the same (radiative forcing) scenario; differences in TWL and precipitation values amongst the models capture the uncertainty of SWI risk projections. The use of TESLA wave simulations enabled us to explore variation in the timing of wave events, and thus variability in the co-occurrence of high TWL and low precipitation.

The use of precipitation as a proxy for river discharge was necessary due to the lack of availability of routed flows for our study site from CMIP5 GCMs. However, this proxy likely introduces bias in our % SWI risk calculations. Since the precipitation values for times when discharge is below the 37th percentile range from 0 to 120 mm (Figure 4.2 (b)), our chosen threshold of 9.5 mm (the median value) likely results in an underestimate of the percentage of time at which the low upstream flow conditions for SWI risk were met. Ultimately, CMIP-modelled routed flow would be preferable to precipitation, and could be included in a similar study once the data is available. Nevertheless, this bias is likely far less important than the overall SLR trend in OWL.

Additionally, there is inherent uncertainty in the CMIP5 GCMs and the true nature of future wave time series. CMIP5 precipitation projections are known to be uncertain due mostly to variations in the responses of different models to the same radiative forcing conditions (Wu et al., 2024). Depending on the direction of the uncertainty (lower or higher modelled precipitation), we may expect our calculated % SWI risks to be over- or under-estimations. For our study, we observed a difference in calculated % SWI risk across GCMs, which was especially prominent in the late century (Figures 4.A.1 and

4.A.2). For waves, although little change is expected for mean H_s, mean T_p may increase by 0.25-0.50 s in March through November in the late century (Erikson et al., 2016). This could contribute to a slight overall increase in TWL not captured by the TESLA wave simulations, suggesting that our %SWI risk calculations may be an underestimate.

Despite these uncertainties, the robustness of the upward trend in the percentage of time in which SWI risk occurs into the future (Figure 4.9) suggests that significant increases in SWI risk will be seen in the coming century. Moreover, the main driver of this increased SWI risk is sea level rise in the OWL predictions. Although there may be changes in future precipitation and waves that could affect SWI in the Pajaro Valley, sea level rise is likely the greatest threat to the region's surface freshwater supplies.

The drivers of SWI in the Pajaro Valley are the same drivers as those for lagoon closures (Orescanin et al., 2021). In Chapter 3, we concluded that observed lagoon closures were necessary to induce SWI in the surface slough system. However, for the current study, we lack predictions of lagoon closures at our study site. The behavior of berms at lagoon mouths in response to SLR is an open area of research. A recent study proposed that the berm height of intermittently closed estuaries scales with TWL, suggesting that berm heights should increase under SLR scenarios (Booysen, Theron, 2020). However, identifying the limit in which berm heights will stop increasing and the berm will be permanently over-topped remains an open question. Regardless, the management of lagoon closures under future climate scenarios will be inextricably linked to the management of freshwater in the Pajaro Valley. For the current study, we assume that when conditions are met for SWI, lagoon closures may also occur, but we leave further investigation of this phenomenon to future research. Ultimately coupled hydro-morphological response at the estuary mouth to climate change (particularly SLR), may alter the % SWI risk as estimated here based on TWL and precipitation alone.

Another approach that is complimentary to the one used here for assessing the risk of events like SWI that have compound drivers is a copula approach. Copulas are popular

in hydrologic research (Tootoonchi et al., 2022) and have been used in compound coastal flooding studies (Lucey, Gallien, 2022). In theory, a copula would allow for simulating realizations of TWL and precipitation from the joint distribution established from a single time series (e.g., single model simulation or observed record of TWL and precipitation). In our study, a copula method was not utilized because the theoretical requirements for copula inputs (e.g., variable autocorrelation) (Tootoonchi et al., 2022) were not met when examining TWL and precipitation at the desired (hourly - daily) temporal resolution. Some studies in the coastal flooding literature have relied on monthly maximum/minimum value inputs to copulas (Lucey, Gallien, 2022). In our case, monthly summaries would not allow us to directly connect our analysis to the SWI thresholds previously established from hourly to daily data in the Pajaro Valley (Ch. 3). We would also have to use a monthly minimum instead of a maximum for precipitation to represent the low upstream flow conditions. However, by nature of precipitation this minimum would almost always be zero, making the copula fitting process difficult. Nevertheless, we acknowledge that a carefully designed copula study could be an alternative approach for future research, and might be particularly useful in cases where TESLA wave simulations are not available to generate realizations of variably-timed wave events, which enabled us to effectively 'sample' from the joint distribution of TWL and precipitation. Another example wherein a copula would be useful would be when using a single time series of wave simulations from CMIP5 GCMs (instead of a wave emulator). In that case, a copula would be used to model the joint distribution of TWL and precipitation based on a single GCM-generated time series for the purpose of 'sampling' the occurrence of high TWL and low precipitation from their fitted joint distribution, similar to what we have done in this study.

Although we have focused our study on the Pajaro Valley and the management decisions of its local water management agency, PV Water, this work provides a framework for assessing SWI vulnerability in coastal watersheds worldwide. While here our thresholds are specifically defined for surface water SWI based on historical observations in the Pajaro

Valley, this approach could be applied broadly across many systems. In particular the co-occurrence of high TWL with low precipitation (i.e., low upstream freshwater discharge) is important not only for surface water SWI, but also groundwater SWI and other processes such as estuary mouth morphodynamics. The finding that the main driver of increased SWI risk is SLR in the OWL predictions is likely to be found as a key driver in SWI projections in other regions and systems as well. As SWI is a growing problem in coastal watersheds, methods like ours are required to aid coastal managers in protecting freshwater resources and adapting to climate change.

4.5 Conclusion

Using observed, modelled, and simulated data to assess the joint distributions of TWL and precipitation, we explored the risk of surface water SWI in the coastal Pajaro Valley under climate change. This work used a novel approach to address how SWI and its drivers may change in the future. Based on our results, we anticipate that SWI risk will substantially increase as we move from the CMIP5 GCM-modeled early century (2006-2050) to late century (2051-2100). Although this study was limited by uncertainty in climate model projections and the lack of lagoon closure predictions, our approach provides both local results and a generalizable framework that can help guide water managers as they adapt their freshwater preservation strategies.

4.6 Acknowledgments

Chapter 4, in part, is currently being prepared for submission for publication of the material. L.N. Kim, S.N. Giddings, M.A. Merrifield, L. Cagigal, M.C. Levy. The dissertation author was the primary investigator and author of this material.

4.A Supplementary Figures

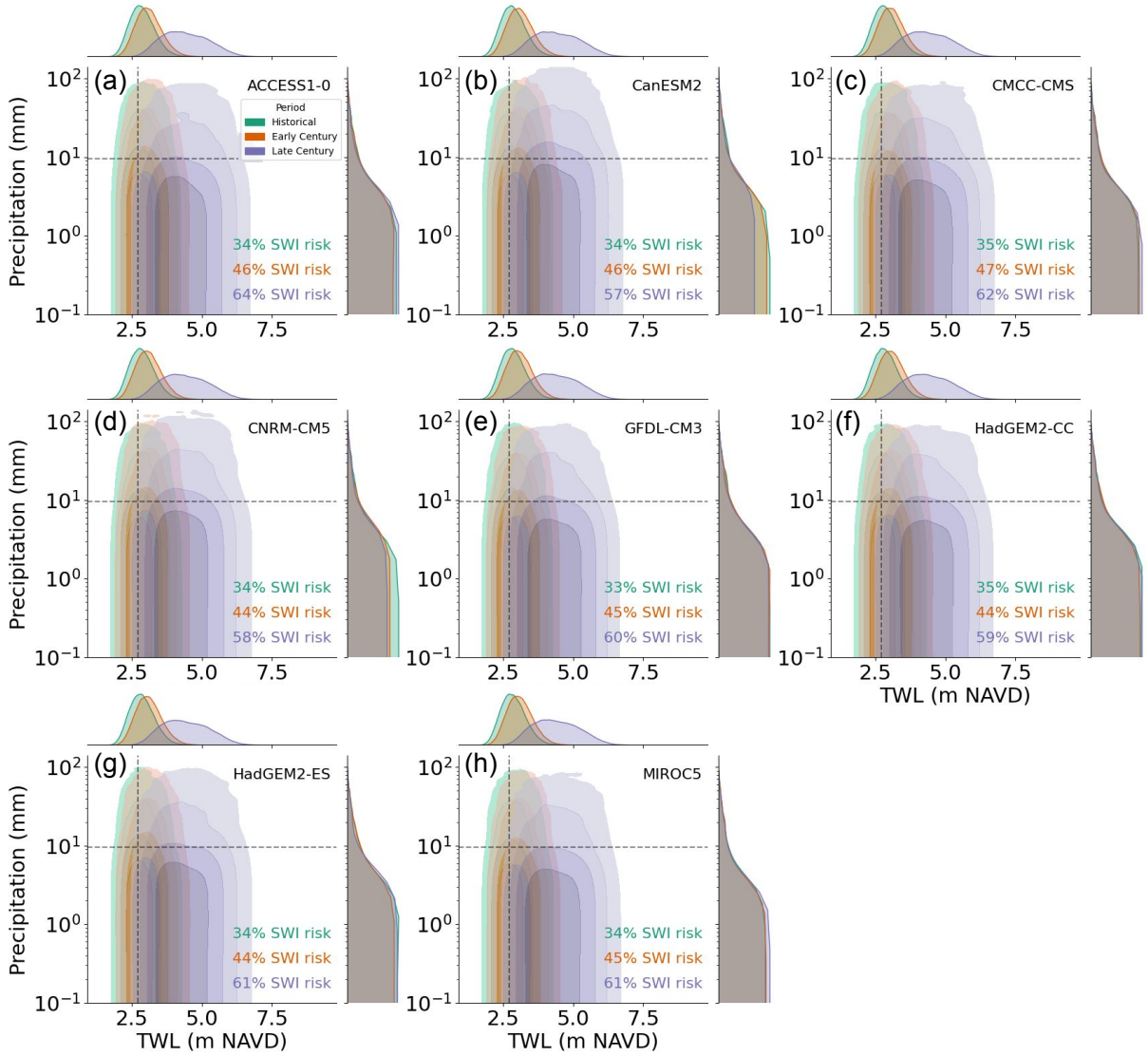

Figure 4.A.1. Joint distributions of TWL comprised of CMIP5 GCM modelled OWL and TESLA wave components and CMIP5 GCM modelled precipitation for (a) the ACCESS1-0, (b) the CanESM2, (c) the CMCC-CMS, (d) the CNRM-CM5, (e) the GFDL-CM3, (f) the HadGEM2-CC, (g) the HadGEM2-ES, and (h) the MIROC5 models for the historical (green), early century (orange), and late century (purple) periods. Dashed gray lines indicate the TWL and precipitation thresholds indicating SWI risk conditions and the percentages listed on the panels indicate the percentage of time in which SWI risk occurs for the dataset.

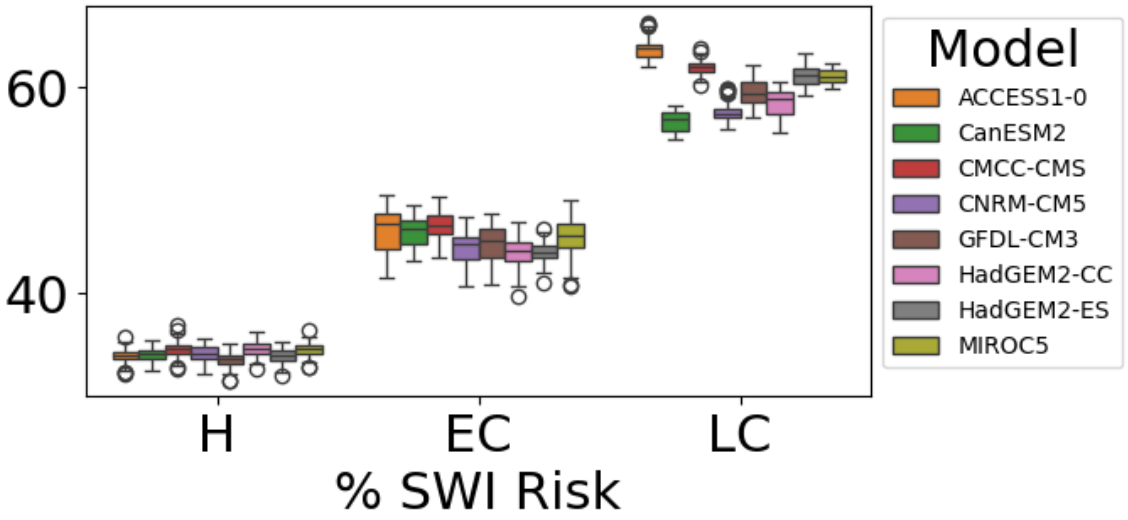

Figure 4.A.2. Boxplots showing the median and 1.5*IQR of the percentage of time in which SWI risk occurs for each model during historical (H), early century (EC), and late century (LC) periods. % SWI risk was calculated for each individual TWL time series (100 total per model).

Bibliography

NOAA/NOS/CO-OPS Observed Water Levels: station 9413450. 2023a.

Watsonville Slough System Managed Aquifer Recharge and Recovery Projects. 5 2023b.

Western Regional Climate Center. 2023c.

Agredano R, Cienfuegos R, Catalán P, Mignot E, Bonneton P, Bonneton N. Morphological changes in a cuspate sandy beach under persistent high- energy swells : Reñaca Beach (Chile) // Marine Geology. 2019. 417. 1–16.

Almar Rafael, Blenkinsopp Chris, Almeida Luis Pedro, Cienfuegos Rodrigo, Catalán Patricio A. Wave runup video motion detection using the Radon Transform // Coastal Engineering. 12 2017. 130. 46–51.

Almar Rafael, Ranasinghe Roshanka, Bergsma Erwin W.J., Diaz Harold, Melet Angelique, Papa Fabrice, Vousdoukas Michalis, Athanasiou Panagiotis, Dada Olusegun, Almeida Luis Pedro, Kestenare Elodie. A global analysis of extreme coastal water levels with implications for potential coastal overtopping // Nature Communications. 12 2021. 12, 1.

Almeida Luis Pedro, Masselink Gerd, Russell Paul, Davidson Mark, Poate Tim, McCall Robert, Blenkinsopp Chris, Turner Ian. Observations of the swash zone on a gravel beach during a storm using a laser-scanner (Lidar) // Journal of Coastal Research. 2013. 65. 636–641.

Almeida Luís Pedro, Almar Rafael, Bergsma Erwin W.J., Berthier Etienne, Baptista Paulo, Garel Erwan, Dada Olusegun A., Alves Bruna. Deriving high spatial-resolution coastal topography from sub-meter satellite stereo imagery // Remote Sensing. 3 2019. 11, 5.

Anderson D., Rueda A., Cagigal L., Antolinez J. A.A., Mendez F. J., Ruggiero P. Time-Varying Emulator for Short and Long-Term Analysis of Coastal Flood Hazard Potential // Journal of Geophysical Research: Oceans. 12 2019. 124, 12. 9209–9234.

Anderson Tiffany R., Fletcher Charles H., Barbee Matthew M., Romine Bradley M., Lemmo Sam, Delevaux Jade M.S. M. S. Modeling multiple sea level rise stresses reveals up to twice the land at risk compared to strictly passive flooding methods // Scientific Reports. 12 2018. 8, 1. 14484.

Anh Duong Tran, Hoang Long Phi, Bui Minh Duc, Rutschmann Peter. Simulating future flows and salinity intrusion using combined one- and two-dimensional hydrodynamic modelling-the case of Hau River, Vietnamese Mekong Delta // Water (Switzerland). 7 2018. 10, 7.

Atkinson Alexander L., Power Hannah E., Moura Theo, Hammond Tim, Callaghan David P., Baldock Tom E. Assessment of runup predictions by empirical models on non-truncated beaches on the south-east Australian coast // Coastal Engineering. 2017. 119, September 2016. 15–31.

Bai Ye, Zhang Zhenxing, Zhao Weiguo. Assessing the Impact of Climate Change on Flood Events Using HEC-HMS and CMIP5 // Water, Air, and Soil Pollution. 6 2019. 230, 6.

Balance Hydrologics . Watsonville Sloughs Hydrology Study. 2014. 1–151.

Barlow Paul M., Reichard Eric G. Saltwater intrusion in coastal regions of North America // Hydrogeology Journal. 2 2010. 18, 1. 247–260.

Basharin Dmitry, Polonsky Alexander, Stankūnavičius Gintautas. Projected precipitation and air temperature over Europe using a performance-based selection method of CMIP5 GCMs // Journal of Water and Climate Change. 2016. 7, 1. 103–113.

Bates Paul D., Quinn Niall, Sampson Christopher, Smith Andrew, Wing Oliver, Sosa Jeison, Savage James, Olcese Gaia, Neal Jeff, Schumann Guy, Giustarini Laura, Coxon Gemma, Porter Jeremy R., Amodeo Mike F., Chu Ziyan, Lewis-Gruss Sharai, Freeman Neil B., Houser Trevor, Delgado Michael, Hamidi Ali, Bolliger Ian, E. McCusker Kelly, Emanuel Kerry, Ferreira Celso M., Khalid Arslaan, Haigh Ivan D., Couasnon Anaïs, E. Kopp Robert, Hsiang Solomon, Krajewski Witold F. Combined Modeling of US Fluvial, Pluvial, and Coastal Flood Hazard Under Current and Future Climates // Water Resources Research. 2 2021. 57, 2.

Beganskas Sarah, Young Kyle S., Fisher Andrew T., Harmon Ryan, Lozano Sacha. Runoff Modeling of a Coastal Basin to Assess Variations in Response to Shifting Climate and Land Use: Implications for Managed Recharge // Water Resources Management. 2019. 33, 5. 1683–1698.

Behrens Dane K., Bombardelli Fabián A., Largier John L. Landward Propagation of Saline Waters Following Closure of a Bar-Built Estuary: Russian River (California, USA) // Estuaries and Coasts. 2016. 39, 3. 621–638.

Behrens Dane K., Bombardelli Fabián A., Largier John L., Twohy Elinor. Episodic closure of the tidal inlet at the mouth of the Russian River - A small bar-built estuary in California // Geomorphology. 2013. 189. 66–80.

Bellafiore Debora, Ferrarin Christian, Maicu Francesco, Manfè Giorgia, Lorenzetti Giuliano, Umgiesser Georg, Zaggia Luca, Levinson Arnoldo Valle. Saltwater Intrusion in a Mediterranean Delta Under a Changing Climate // Journal of Geophysical Research: Oceans. 2 2021. 126, 2.

Ben Alaya M. A., Chebana F., Ouarda T. B. M. J. Probabilistic Gaussian Copula Regression Model for Multisite and Multivariable Downscaling // Journal of Climate. 5 2014. 27, 9. 3331–3347.

Bertin Xavier, Mendes Diogo, Martins Kévin, Fortunato André B., Lavaud Laura. The Closure of a Shallow Tidal Inlet Promoted by Infragravity Waves // Geophysical Research Letters. 2019. 46, 12. 6804–6810.

Beuzen T., Harley M. D., Splinter K. D., Turner I. L. Controls of Variability in Berm and Dune Storm Erosion // Journal of Geophysical Research: Earth Surface. 2019. 124, 11. 2647–2665.

Bevacqua E, Maraun D, Vousdoukas M I, Voukouvalas E, Vrac M, Mentaschi L, Widmann M. Higher probability of compound flooding from precipitation and storm surge in Europe under anthropogenic climate change // Science Advances. 2019. 5.

Birkemeier William A., ASCE M., Long Charles E., Hathaway Kent K. DELILAH, DUCK94 & SandyDuck: Three Nearshore Field Experiments // Coastal Engineering. 1996. 4052–4065.

Birkemeier William A., Holland K. Todd. The U.S. Army Corps of Engineers Field Research Facility: More than two decades of coastal research. Kitty Hawk, 2000.

Blenkinsopp C. E., Mole M. A., Turner I. L., Peirson W. L. Measurements of the time-varying free-surface profile across the swash zone obtained using an industrial LIDAR // Coastal Engineering. 2010. 57, 11-12. 1059–1065.

Blodgett D., Johnson J.M. nhdplusTools: Tools for Accessing and Working with the NHDPlus. 2022.

Booysen Zane, Theron André K. Methods for predicting berm height at Temporarily Open/Closed Estuaries // Estuarine, Coastal and Shelf Science. 2020. 245.

Brink Matthijs van den, Huismans Ymkje, Blaas Meinte, Zwolsman Gertjan. Climate change induced salinization of drinking water inlets along a tidal branch of the Rhine

River: Impact assessment and an adaptive strategy for water resources management // Climate. 4 2019. 7, 4.

Observations of storm morphodynamics using Coastal Lidar and Radar Imaging System (CLARIS): Importance of wave refraction and dissipation over complex surf-zone morphology at a shoreline erosional hotspot. // . 2010. 210.

Brodie Katherine L., Raubenheimer B., Elgar Steve, Slocum R. K., McNinch J. E. Lidar and pressure measurements of inner-surfzone waves and setup // Journal of Atmospheric and Oceanic Technology. 2015. 32, 10. 1945–1959.

Burvingt Olivier, Masselink Gerd, Russell Paul, Scott Tim. Classification of beach response to extreme storms // Geomorphology. 2017. 295. 722–737.

Cagigal Laura, Rueda Ana, Anderson Dylan, Ruggiero Peter, Merrifield Mark A., Montaño Jennifer, Coco Giovanni, Méndez Fernando J. A multivariate, stochastic, climate-based wave emulator for shoreline change modelling // Ocean Modelling. 10 2020. 154.

California Department of Water Resources . CIMIS. 2023.

Carollo . Basin Management Plan Update. 2014.

Charbonneau Bianca R., Dohner Stephanie M. Microscale and mesoscale aeolian processes of sandy coastal foredunes from background to extreme conditions // Remote Sensing. 11 2021. 13, 21.

Chelton Dudley B., Davis Russ E. Monthly Mean Sea-Level Variability Along the West Coast of North America // Journal of Physical Oceanography. 1982. 12. 757–784.

Chen Wei, Chen Kuo, Kuang Cuiping, Zhu David Z., He Lulu, Mao Xiaodan, Liang Huidi, Song Honglin. Influence of sea level rise on saline water intrusion in the Yangtze River Estuary, China // Applied Ocean Research. 1 2015. 54, 2016. 12–25.

Chen Wei, Chen Kuo, Kuang Cuiping, Zhu David Z., He Lulu, Mao Xiaodan, Liang Huidi, Song Honglin. Influence of sea level rise on saline water intrusion in the Yangtze River Estuary, China // Applied Ocean Research. 1 2016. 54. 12–25.

Ciriano Yolanda, Coco Giovanni, Bryan K. R., Elgar Steve. Field observations of swash zone infragravity motions and beach cusp evolution // Journal of Geophysical Research C: Oceans. 2005. 110, 2. 1–10.

Clark Ross, O'Connor Kevin. A systematic survey of bar-built estuaries along the California coast // Estuarine, Coastal and Shelf Science. 2019. 226, June. 106285.

Cohn Nicholas, Brodie Katherine, Conery Ian, Spore Nicholas. Alongshore Variable Accretional and Erosional Coastal Foredune Dynamics at Event to Interannual Timescales // Earth and Space Science. 12 2022. 9, 12.

Cohn Nicholas, Brodie Katherine L., Johnson Bradley, Palmsten Margaret L. Hotspot dune erosion on an intermediate beach // Coastal Engineering. 12 2021. 170.

Cosgrove William J., Loucks Daniel P. Water management: Current and future challenges and research directions // Water Resources Research. 2015. 51. 4823–4839.

Dawson Jason, Orescanin Mara M., Clark Ross, O'Connor Kevin. Spatiotemporal variability of dissolved oxygen in response to morphological state in a central California coast bar-built estuary // Estuarine, Coastal and Shelf Science. 3 2023. 282. 108241.

Dissanayake Pushpa, Brown Jennifer, Wisse Paul, Karunarathna Harshinie. Comparison of storm cluster vs isolated event impacts on beach/dune morphodynamics // Estuarine, Coastal and Shelf Science. 10 2015. 164. 301–312.

Duong Trang Minh, Ranasinghe Roshanka, Walstra Dirkjan, Roelvink Dano. Assessing climate change impacts on the stability of small tidal inlet systems: Why and how? // Earth-Science Reviews. 2016. 154. 369–380.

Elko Nicole, Dietrich Casey, Cialone Mary, Stockdon Hilary, Bilskie Matt W., Boyd Brandon, Charbonneau Bianca, Cox Dan, Dresback Kendra, Elgar Steve, Lewis Amanda, Limber Patrick, Long Joe, Massey Chris, Mayo Talea, McIntosh Kathryn, Nadal-Caraballo Norberto, Raubenheimer Britt, Tomiczek Tori, Wargula Anna. Advancing the understanding of storm processes and impacts // Shore & Beach. 2019. 87, 1. 37–50.

The Future of Nearshore Processes Research. // . 2014.

Environmental Science Associates . Final Memorandum, Harkins and Struve Sloughs Hydrologic Analysis of Diversion Alternatives. Prepared for the Pajaro Valley Water Management Agency. 7 2020.

Erikson L.H., Hegermiller C.E., Barnard P.L., Storlazzi C. Wave Projections for United States Mainland Coasts // U.S. Geological Survey summary of methods to accompany data release. 2016.

Eslami Sepehr, Hoekstra Piet, Minderhoud Philip S.J., Trung Nam Nguyen, Hoch Jannis M., Sutanudjaja Edwin H., Dung Do Duc, Tho Tran Quang, Voepel Hal E., Woillez Marie Noëlle, Vegt Maarten van der. Projections of salt intrusion in a mega-delta under climatic and anthropogenic stressors // Communications Earth and Environment. 12 2021. 2, 1.

Feagin R. A., Furman M., Salgado K., Martinez M. L., Innocenti R. A., Eubanks K., Figlus J., Huff T. P., Sigren J., Silva R. The role of beach and sand dune vegetation in mediating wave run up erosion // Estuarine, Coastal and Shelf Science. 4 2019. 219. 97–106.

Ferguson Grant, Gleeson Tom. Vulnerability of coastal aquifers to groundwater use and climate change. 5 2012. 342–345.

Ganguli Poulomi, Merz Bruno. Extreme Coastal Water Levels Exacerbate Fluvial Flood Hazards in Northwestern Europe // Scientific Reports. 12 2019. 9, 1.

Geyer W. Rockwell, MacCready Parker. The estuarine circulation // Annual Review of Fluid Mechanics. 2014. 46. 175–197.

Goebel Meredith, Knight Rosemary, Halkjær Max. Mapping saltwater intrusion with an airborne electromagnetic method in the offshore coastal environment, Monterey Bay, California // Journal of Hydrology: Regional Studies. 6 2019. 23. 100602.

Goebel Meredith, Pidlisecky Adam, Knight Rosemary. Resistivity imaging reveals complex pattern of saltwater intrusion along Monterey coast // Journal of Hydrology. 8 2017. 551. 746–755.

Gomez , Sullivan Engineers P.C. Final study report: salinity and salt wedge encroachment study RSP 3.20 Conowingo Hydroelectric Project FERC Project number 405. 2012.

Guanche Y., Mínguez R., Méndez F. J. Autoregressive logistic regression applied to atmospheric circulation patterns // Climate Dynamics. 1 2014. 42, 1-2. 537–552.

Hanes Daniel M., Ward Kristen, Erikson Li H. Waves and tides responsible for the intermittent closure of the entrance of a small, sheltered tidal wetland at San Francisco, CA // Continental Shelf Research. 2011. 31, 16. 1682–1687.

Hansen D.V., Rattray M. Gravitational circulation in straits and estuaries // Journal of Marine Research. 1965. 28. 104–122.

Hanson R. T., Lockwood B., Schmid Wolfgang. Analysis of projected water availability with current basin management plan, Pajaro Valley, California // Journal of Hydrology. 11 2014a. 519, PA. 131–147.

Hanson R.T., Schmid Wolfgang, Faunt Claudia C., Lear Jonathan, Lockwood Brian. Integrated Hydrologic Model of Pajaro Valley , Santa Cruz and Monterey Counties , California Scientific Investigations Report 2014 – 5111. 2014b.

Harley Mitchell D., Turner Ian L., Kinsela Michael A., Middleton Jason H., Mumford

Peter J., Splinter Kristen D., Phillips Matthew S., Simmons Joshua A., Hanslow David J., Short Andrew D. Extreme coastal erosion enhanced by anomalous extratropical storm wave direction // Scientific Reports. 2017. 7, 1. 1–9.

Harley Mitchell D., Turner Ian L., Splinter Kristen D., Phillips Matthew S., Simmons Joshua A. Beach response to Australian East Coast Lows : A comparison between the 2007 and 2015 events // Journal of Coastal Research. 2016. Special Issue No. 75. 388–392.

Harvey Madeleine E. Hydrodynamics in Intermittently Closed Estuaries Over Multiple Timescales and Varying Forcing Conditions // Thesis dissertation. 2019. 214.

Harvey Madeleine E., Giddings Sarah N., Pawlak Geno, Crooks Jeffrey A. Hydrodynamic Variability of an Intermittently Closed Estuary over Interannual, Seasonal, Fortnightly, and Tidal Timescales // Estuaries and Coasts. 1 2023. 46, 1. 84–108.

Harvey Madeleine E., Giddings Sarah N., Stein Eric D., Crooks Jeffrey A., Whitcraft Christine, Gallien Timu, Largier John L., Tiefenthaler Liesl, Meltzer Hallee, Pawlak Geno, Thorne Karen, Johnston Karina, Ambrose Richard, Schroeter Stephen C., Page Henry M., Elwany Hany. Effects of Elevated Sea Levels and Waves on Southern California Estuaries During the 2015–2016 El Niño // Estuaries and Coasts. 2020. 43, 2. 256–271.

Hauer Mathew E., Fussell Elizabeth, Mueller Valerie, Burkett Maxine, Call Maia, Abel Kali, McLeman Robert, Wrathall David. Sea-level rise and human migration. 1 2020. 28–39.

Henderson Cassandra S., Fiedler Julia W., Merrifield Mark A., Guza R. T., Young Adam P. Phase resolving runup and overtopping field validation of SWASH // Coastal Engineering. 8 2022. 175.

Hermans Tim H.J., Gregory Jonathan M., Palmer Matthew D., Ringer Mark A., Katsman Caroline A., Slangen Aimée B.A. Projecting Global Mean Sea-Level Change Using CMIP6 Models // Geophysical Research Letters. 3 2021. 48, 5.

Holland K. T., Holman R. A. Field observations of beach cusps and swash motions // Marine Geology. 1996. 134, 1-2. 77–93.

Holland K. Todd. Beach cusp formation and spacings at Duck, United States // Continental Shelf Research. 1998. 18, 10. 1081–1098.

Holman Rob, Haller Merrick C. Remote sensing of the nearshore // Annual Review of Marine Science. 2013. 5. 95–113.

Holman Rob A. Extreme Value Statistics for Wave Run-Up on a Natural Beach // Coastal

Engineering. 3 1986. 9. 527–544.

Holman Robert A, Sallenger Asbury H. Jr. Sand bar generation: A discussion of the Duck experiment series // Journal of Coastal Research. 1993. SI, 15. 76–92.

Hong Bo, Shen Jian. Responses of estuarine salinity and transport processes to potential future sea-level rise in the Chesapeake Bay // Estuarine, Coastal and Shelf Science. 6 2012. 104-105. 33–45.

Houben Georg, Post Vincent E.A. The first field-based descriptions of pumping-induced saltwater intrusion and upconing // Hydrogeology Journal. 2 2017. 25, 1. 243–247.

IPCC . IPCC, 2014: Climate Change 2014: Impacts, Adaptation, and Vulnerability. Part B: Regional Aspects. Contribution of Working Group II to the Fifth Assessment Report of the Intergovernmental Panel on Climate Change. Cambridge, 2014. 1439–1499.

Jacobs Katharine, Lebel Louis, Buizer James, Addams Lee, Matson Pamela, McCullough Ellen, Garden Po, Saliba George, Finan Timothy. Linking knowledge with action in the pursuit of sustainable water-resources management // PNAS. 1 2010. 113, 17. 4591–4596.

Jasechko Scott, Perrone Debra, Seybold Hansjörg, Fan Ying, Kirchner James W. Groundwater level observations in 250,000 coastal US wells reveal scope of potential seawater intrusion // Nature Communications. 12 2020. 11, 1.

Kahle David, Wickham Hadley. ggmap: Spatial Visualization with ggplot2 // The R Journal. 6 2013. 5, 1. 144–161.

Kaushal Sujay S., Likens Gene E., Pace Michael L., Reimer Jenna E., Maas Carly M., Galella Joseph G., Utz Ryan M., Duan Shuiwang, Kryger Julia R., Yaculak Alexis M., Boger Walter L., Bailey Nathan W., Haq Shahan, Wood Kelsey L., Wessel Barret M., Park Cedric Evan, Collison Daniel C., Aisin Belie Y.'aaqob I., Gedeon Taylor M., Chaudhary Sona K., Widmer Jacob, Blackwood Charles R., Bolster Claire M., Devilbiss Matthew L., Garrison Diego L., Halevi Sharon, Kese Gannon Q., Quach Emily K., Rogelio Christina M.P., Tan Maggie L., Wald Henry J.S., Woglo Seyram A. Freshwater salinization syndrome: from emerging global problem to managing risks // Biogeochemistry. 6 2021. 154, 2. 255–292.

Knowles N., Cronkite-Ratcliff C., Pierce D. W., Cayan D. R. Responses of Unimpaired Flows, Storage, and Managed Flows to Scenarios of Climate Change in the San Francisco Bay-Delta Watershed // Water Resources Research. 10 2018. 54, 10. 7631–7650.

Langridge Ruth. Central Coast Summary Report. California's Fourth Climate Change Assessment. 2018.

Largier J. L., Slinger J. H., Taljaard S. The stratified hydrodynamics of the Palmiet - a prototypical bar-built estuary // Coastal and Estuarine Studies. 1992. 135–153.

Largier J. L., Taljaard S. The dynamics of tidal intrusion, retention, and removal of seawater in a bar-built estuary // Estuarine, Coastal and Shelf Science. 1991. 33, 4. 325–338.

Largier John L. Low-inflow estuaries: Hypersaline, inverse, and thermal scenarios // Contemporary Issues in Estuarine Physics. Cambridge: Cambridge University Press, 2010.

Largier John L. Recognizing Low-Inflow Estuaries as a Common Estuary Paradigm // Estuaries and Coasts. 12 2023. 46, 8. 1949–1970.

Leaman Chris, Beuzen Tomas, Goldstein Evan B. py-wave-runup. 2020.

Lee Guan hong, Nicholls Robert J., Birkemeier William A. Storm-driven variability of the beach-nearshore profile at Duck, North Carolina, USA, 1981-1991 // Marine Geology. 1998. 148, 3-4. 163–177.

Levintal Elad, Kniffin Maribeth L., Ganot Yonatan, Marwaha Nisha, Murphy Nicholas P., Dahlke Helen E. Agricultural managed aquifer recharge (Ag-MAR)—a method for sustainable groundwater management: A review // Critical Reviews in Environmental Science and Technology. 2 2023. 53, 3. 291–314.

Levy Morgan C., Garcia Margaret, Blair Peter, Chen Xi, Gomes Sharlene L., Gower Drew B., Grames Johanna, Kuil Linda, Liu Ye, Marston Landon, McCord Paul F., Roobavannan Mahendran, Zeng Ruijie. Wicked but worth it: student perspectives on socio-hydrology // Hydrological Processes. 4 2016. 30, 9. 1467–1472.

Li Linjiang, Zhu Jianrong, Chant Robert J., Wang Chuning, Pareja-Roman L. Fernando. Effect of Dikes on Saltwater Intrusion Under Various Wind Conditions in the Changjiang Estuary // Journal of Geophysical Research: Oceans. 7 2020. 125, 7.

Livneh Ben, Bohn Theodore J, Pierce David W, Muñoz-Arriola Francisco, Nijssen Bart, Vose Russell, Cayan Daniel R, Brekke Levi. A spatially comprehensive, meteorological data set for Mexico, the U.S., and southern Canada (NCEI Accession 0129374). 6 2023.

Loáiciga Hugo A., Pingel Thomas J., Garcia Elizabeth S. Sea water intrusion by sea-level rise: Scenarios for the 21st century // Ground Water. 1 2012. 50, 1. 37–47.

Lucey Joseph T.D., Gallien Timu W. Characterizing multivariate coastal flooding events in a semi-arid region: The implications of copula choice, sampling, and infrastructure // Natural Hazards and Earth System Sciences. 6 2022. 22, 6. 2145–2167.

Ludka B C, Guza R.T., O'Reilly W.C., Merrifield M.A., Flick R.E., Bak A.S., Hesser T., Bucciarelli R., Olfe C., Woodward B., Boyd W., Smith K., Okihiro M., Grenzeback R., Parry L., Boyd G. Sixteen years of bathymetry and waves at San Diego Beaches // Nature Scientific Data. 2019. 6, 161. 1–13.

MacCready Parker. Toward a unified theory of tidally-averaged estuarine salinity structure // Estuaries. 2004. 27, 4. 561–570.

Martins Kévin, Blenkinsopp Chris E., Power Hannah E., Bruder Brittany, Puleo Jack A., Bergsma Erwin W.J. High-resolution monitoring of wave transformation in the surf zone using a LiDAR scanner array // Coastal Engineering. 2017. 128, January. 37–43.

Masselink Gerhard, Hegge Bruce J., Pattiaratchi Charitha B. Beach cusp morphodynamics // Earth Surface Processes and Landforms. 1997. 22, 12. 1139–1155.

Masselink Gerhard, Pattiaratchi Charitha B. Morphological evolution of beach cusps and associated swash circulation patterns // Marine Geology. 1998. 146, 1-4. 93–113.

Matsumoto H., Young A. P., Guza R. T. Cusp and Mega Cusp Observations on a Mixed Sediment Beach // Earth and Space Science. 2020. 7, 10. 1–8.

McKeon Margaret A., Horner-Devine Alexander R., Giddings Sarah N. Seasonal Changes in Structure and Dynamics in an Urbanized Salt Wedge Estuary // Estuaries and Coasts. 2021. 44, 3. 589–607.

McSweeney S. L., Kennedy D. M., Rutherfurd I. D., Stout J. C. Intermittently Closed/Open Lakes and Lagoons: Their global distribution and boundary conditions // Geomorphology. 9 2017. 292. 142–152.

Medellín-Azuara Josué, Howitt Richard E., Hanak Ellen, Lund Jay R., Fleenor William. Agricultural losses from salinity in California's Sacramento-San Joaquin delta // San Francisco Estuary and Watershed Science. 2014. 12, 1.

Michael Holly A., Post Vincent E.A., Wilson Alicia M., Werner Adrian D. Science, society, and the coastal groundwater squeeze // Water Resources Research. 2017. 53. 2610–2617.

Miller Jerry R., Orbock Miller Suzanne M., Torzynski A. Cindy, Kochel R. Craig. Beach cusp destruction, formation, and evolution during and subsequent to an extratropical storm, Duck, North Carolina // Journal of Geology. 1989. 97, 6. 749–760.

Monismith Stephen G, Burau Jon R, Stacey Mark T. Structure and Flow-Induced Variability of the Subtidal Salinity Field in Northern San Francisco Bay. 2002.

NOAA . What percentage of the American population lives near the coast? 2021.

NOAA . NDBC: Station 46042. 2023a.

NOAA . NDBC: Station 46114. 2023b.

Nielsen P. Coastal and Estuarine Processes. Singapore: WORLD SCIENTIFIC, 2009.

O'Dea Annika, Brodie Katherine L., Hartzell Preston. Continuous Coastal Monitoring with an Automated Terrestrial Lidar Scanner // Journal of Marine Science and Engineering. 2 2019. 7, 2. 37.

Okely Patricia, Imberger Jörg. Horizontal transport induced by upwelling in a canyon-shaped reservoir // Hydrobiologia. 2007. 586, 1. 343–355.

Orescanin Mara M., Coughlin Jillian, Young Walter R. Morphological response of variable river discharge and wave forcing at a bar-built estuary // Estuarine, Coastal and Shelf Science. 9 2021. 258.

Orescanin Mara M., Scooler Jeff. Observations of episodic breaching and closure at an ephemeral river // Continental Shelf Research. 2018. 166, July. 77–82.

Spectral Analysis of Beach Cusp Evolution Using 3D Lidar Scans. // . 2019. 657–673.

Pajaro Valley Water Management Agency . Resources & References. 2023.

Pajaro Valley Water Management Agency , Carollo . Recharge Basin Hydrogeologic Study. 2018.

Pajaro Valley Water Management Agency , Montgomery & Associates . Pajaro Valley Basin Management Plan. 2022.

Paul Michael J., Coffey Rory, Stamp Jen, Johnson Thomas. A Review of Water Quality Responses to Air Temperature and Precipitation Changes 1: Flow, Water Temperature, Saltwater Intrusion. 2019. 824–843.

Payo-Payo Marta, Bricheno Lucy M., Dijkstra Yoeri M., Cheng Weicong, Gong Wenping, Amoudry Laurent O. Multiscale Temporal Response of Salt Intrusion to Transient River and Ocean Forcing // Journal of Geophysical Research: Oceans. 3 2022. 127, 3.

Phillips M. S., Blenkinsopp C. E., Splinter K. D., Harley M. D., Turner I. L. Modes of Berm and Beachface Recovery Following Storm Reset: Observations Using a Continuously Scanning Lidar // Journal of Geophysical Research: Earth Surface. 2019. 124, 3. 720–736.

Phillips Matthew S., Harley Mitchell D., Turner Ian L., Splinter Kristen D., Cox Ron J. Shoreline recovery on wave-dominated sandy coastlines: the role of sandbar morphodynamics and nearshore wave parameters // Marine Geology. 2017. 385. 146–159.

Pierce David W, Cayan Daniel R, Thrasher Bridget L. Statistical Downscaling Using Localized Constructed Analogs (LOCA) // Journal of Hydrometeorology. 2014. 15. 2558–2585.

Pugh David. Tides, surges, and mean sea-level. 1987. 472.

Pye Kenneth, Blott Simon J. Assessment of beach and dune erosion and accretion using LiDAR: Impact of the stormy 2013-14 winter and longer term trends on the Sefton Coast, UK // Geomorphology. 2016. 266, March 2014. 146–167.

Racz Andrew J., Fisher Andrew T., Schmidt Calla M., Lockwood Brian S., Huertos Marc Los. Spatial and Temporal Infiltration Dynamics During Managed Aquifer Recharge // Groundwater. 7 2012. 50, 4. 562–570.

Ralston David K., Geyer W. Rockwell, Lerczak James A. Structure, variability, and salt flux in a strongly forced salt wedge estuary // Journal of Geophysical Research: Oceans. 2010. 115, 6. 1–21.

Ranasinghe Roshanka, Pattiaratchi Charitha. The seasonal closure of tidal inlets: Causes and effects // Coastal Engineering Journal. 2003. 45, 4. 601–627.

Rice Karen C., Hong Bo, Shen Jian. Assessment of salinity intrusion in the James and Chickahominy Rivers as a result of simulated sea-level rise in Chesapeake Bay, East Coast, USA // Journal of Environmental Management. 11 2012. 111. 61–69.

Rodrigues Marta, Fortunato André B., Freire Paula. Saltwater intrusion in the upper Tagus estuary during droughts // Geosciences. 9 2019. 9, 9.

Ruggiero P., Komar P. D., McDougal W. G., Marra J. J., Beach R. A. Wave runup, extreme water levels and the erosion of properties backing beaches // Journal of Coastal Research. 2001. 17, 2. 407–419.

Russo Tess A., Fisher Andrew T., Lockwood Brian S. Assessment of managed aquifer recharge site suitability using a GIS and modeling // Groundwater. 2015. 53, 3. 389–400.

Sallenger Jr. Storm impact scale for barrier islands // Journal of Coastal Research. 2000. 16, 3. 890–895.

Sawyer Audrey H, David Cédric H, Famiglietti James S. Continental patterns of submarine groundwater discharge reveal coastal vulnerabilities // Science. 2016. 353, 6300. 705–707.

Schmidt C. M., Fisher A. T., Racz A., Wheat C. G., Los Huertos M., Lockwood B. Rapid nutrient load reduction during infiltration of managed aquifer recharge in an agricultural groundwater basin: Pajaro Valley, California // Hydrological Processes. 7 2012. 26, 15. 2235–2247.

Schmidt Calla M., Fisher Andrew T., Racz Andrew J., Lockwood Brian S., Huertos Marc Los. Linking Denitrification and Infiltration Rates during Managed Groundwater Recharge // Environmental Science & Technology. 11 2011. 45, 22. 9634–9640.

Senechal N, Coco G, Bryan K R, Holman R A. Wave runup during extreme storm conditions // J. Geophys. Res. 2011. 116. 7032.

Senechal Nadia, Coco Giovanni, Plant Nathaniel, Bryan Karin R., Brown Jenna, MacMahan Jamie H. M. Field Observations of Alongshore Runup Variability Under Dissipative Conditions in the Presence of a Shoreline Sandwave // Journal of Geophysical Research: Oceans. 9 2018. 123, 9. 6800–6817.

Smit P.B., Stelling G.S., Roelvink D., Vries J.S.M. van Thiel de, McCall R.T., Dongeren A.R. van, Zwinkels C., Jacobs R. XBeach: Non-hydrostatic model. Delft, The Netherlands, 2010.

Smith Jane McKee, Bak Spicer, Hesser Tyler, Bryant Mary A., Massey Chris. Frf Wave Test Bed and Bathymetry Inversion // Coastal Engineering Proceedings. 2017. 35. 22.

Splinter Kristen D., Carley James T., Golshani Aliasghar, Tomlinson Rodger. A relationship to describe the cumulative impact of storm clusters on beach erosion // Coastal Engineering. 2014. 83. 49–55.

Splinter Kristen D., Kearney Edward T., Turner Ian L. Drivers of alongshore variable dune erosion during a storm event: Observations and modelling // Coastal Engineering. 2018. 131, December 2016. 31–41.

ERDC/CHL SR-19-4 "Coastal Lidar and Radar Imaging System (CLARIS) Lidar Data Report: 2011 - 2017". // . 2019. July.

Stockdon Hilary F., Holman Rob A., Howd Peter A., Sallenger Asbury H. Empirical parameterization of setup, swash, and runup // Coastal Engineering. 2006. 53, 7. 573–588.

Stockdon Hilary F., Sallenger Asbury H., Holman Rob A., Howd Peter A. A simple model for the spatially-variable coastal response to hurricanes // Marine Geology. 3 2007a. 238, 1-4. 1–20.

Stockdon Hilary F., Thompson David M., Sallenger Asbury H. Hindcasting potential

hurricane impacts on rapidly changing barrier islands // 6th International Conference on Coastal Sediments, New Orleans. 2007b. 976–985.

Susquehanna River Basin Commission . Conowingo Pond Management Plan. 2006.

Thornton E. B., MacMahan J., Sallenger A. H. Rip currents, mega-cusps, and eroding dunes // Marine Geology. 2007. 240, 1-4. 151–167.

Thorslund Josefin, Bierkens Marc F.P., Oude Essink Gualbert H.P., Sutanudjaja Edwin H., Vliet Michelle T.H. van. Common irrigation drivers of freshwater salinisation in river basins worldwide // Nature Communications. 12 2021. 12, 1.

Tian Richard. Factors controlling saltwater intrusion across multi-time scales in estuaries, Chester River, Chesapeake Bay // Estuarine, Coastal and Shelf Science. 7 2019. 223. 61–73.

Tootoonchi Faranak, Sadegh Mojtaba, Haerter Jan Olaf, Räty Olle, Grabs Thomas, Teutschbein Claudia. Copulas for hydroclimatic analysis: A practice-oriented overview. 3 2022.

Try Sophal, Tanaka Shigenobu, Tanaka Kenji, Sayama Takahiro, Khujanazarov Temur, Oeurng Chantha. Comparison of CMIP5 and CMIP6 GCM performance for flood projections in the Mekong River Basin // Journal of Hydrology: Regional Studies. 4 2022. 40.

Tully Kate, Gedan Keryn, Epanchin-Niell Rebecca, Strong Aaron, Bernhardt Emily S., Bendor Todd, Mitchell Molly, Kominoski John, Jordan Thomas E., Neubauer Scott C., Weston Nathaniel B. The invisible flood: The chemistry, ecology, and social implications of coastal saltwater intrusion // BioScience. 2019. 69, 5. 368–378.

Turner Ian L., Harley Mitchell D., Short Andrew D., Simmons Joshua A., Bracs Melissa A., Phillips Matthew S., Splinter Kristen D. A multi-decade dataset of monthly beach profile surveys and inshore wave forcing at Narrabeen, Australia // Scientific Data. 2016. 3. 1–13.

USGS . Water Data: Pajaro R a Chittenden CA - 11159000. 2023.

Vitousek Sean, Barnard Patrick L., Fletcher Charles H., Frazer Neil, Erikson Li, Storlazzi Curt D. Doubling of coastal flooding frequency within decades due to sea-level rise // Scientific Reports. 12 2017. 7, 1. 1399.

Vogel Richard M., Lall Upmanu, Cai Ximing, Rajagopalan Balaji, Weiskel Peter K., Hooper Richard P., Matalas Nicholas C. Hydrology: The interdisciplinary science of water // Water Resources Research. 6 2015. 51, 6. 4409–4430.

Vousdoukas M. I., Kirupakaramoorthy T., Oumeraci H., Torre M. de la, Wübbold F., Wagner B., Schimmels S. The role of combined laser scanning and video techniques in monitoring wave-by-wave swash zone processes // Coastal Engineering. 2014.

Vousdoukas Michalis I., Almeida Luis Pedro M., Ferreira Oscar. Beach erosion and recovery during consecutive storms at a steep-sloping, meso-tidal beach // Earth Surface Processes and Landforms. 2012a. 37, 6. 583–593.

Vousdoukas Michalis Ioannis, Wziatek Dagmara, Almeida Luis Pedro. Coastal vulnerability assessment based on video wave run-up observations at a mesotidal, steep-sloped beach // Ocean Dynamics. 2012b. 62, 1. 123–137.

Ward Philip J., Couasnon Anaïs, Eilander Dirk, Haigh Ivan D., Hendry Alistair, Muis Sanne, Veldkamp Ted I.E., Winsemius Hessel C., Wahl Thomas. Dependence between high sea-level and high river discharge increases flood hazard in global deltas and estuaries // Environmental Research Letters. 2018. 13, 8.

White Elliott, Kaplan David. Restore or retreat? saltwater intrusion and water management in coastal wetlands // Ecosystem Health and Sustainability. 1 2017. 3, 1.

Williams M.E., Stacey M.T. Tidally discontinuous ocean forcing in bar-built estuaries: the interaction of tides, infragravity motions, and frictional control // Journal of Geophysical Research: Oceans. 2015. 120, 7. 4654–4669.

Wu Yi, Miao Chiyuan, Slater Louise, Fan Xuewei, Chai Yuanfang, Sorooshian Soroosh. Hydrological Projections under CMIP5 and CMIP6: Sources and Magnitudes of Uncertainty // Bulletin of the American Meteorological Society. 1 2024. 105, 1. E59–E74.

Xu Kui, Wang Chenyue, Bin Lingling. Compound flood models in coastal areas: a review of methods and uncertainty analysis // Natural Hazards. 3 2023. 116, 1. 469–496.

Zijlema Marcel, Stelling Guus, Smit Pieter. SWASH: An operational public domain code for simulating wave fields and rapidly varied flows in coastal waters // Coastal Engineering. 2011. 58, 10. 992–1012.